Backlash Reduction Using Base Proximal Actuation Redundancy for 3-RRR and 3-RPR Planar Parallel Manipulators

by

Xu Mao
B.Eng., Jilin University of P.R. China, 1999
M.A.Sc., Kongju National University of South Korea, 2006

A Dissertation Submitted in Partial Fulfillment
of the Requirements for the Degree of

DOCTOR OF PHILOSOPHY

in the Department of Mechanical Engineering

Supervisory Committee

Backlash Reduction Using Base Proximal Actuation Redundancy for 3-RRR and 3-RPR Planar Parallel Manipulators

by

Xu Mao
B.Eng., Jilin University of P.R. China, 1999
M.A.Sc., Kongju National University of South Korea, 2006

Supervisory Committee

Dr. Yang Shi, Supervisor (Department of Mechanical Engineering)

Dr. Daniela Constantinescu, Departmental Member (Department of Mechanical Engineering)

Dr. Zuomin Dong, Departmental Member (Department of Mechanical Engineering)

Dr. Wu-Sheng Lu, Outside Member (Department of Electronic Engineering Department)

Abstract

Supervisory Committee

Supervisor: Dr. Yang Shi (Department of Mechanical Engineering)

Departmental Member: Dr. Daniela Constantinescu (Department of Mechanical Engineering)

Departmental Member: Dr. Zuomin Dong (Department of Mechanical Engineering)

Outside Member: Dr. Wu-Sheng Lu (Department of Electronic Engineering)

The goal of the research of this Dissertation is using actuation redundancy to reduce backlash in parallel manipulators (*PM*s.) Initially, 3-*RRR* and 3-*RPR PM* layouts where 3 is the number of branches, *R* is a revolute joint and *P* is a prismatic joint, are introduced. Actuated joints will later be underlined in the *PM* desciptions. A method for determining *PM* working area for rotated payload platforms, based on a mechanism inversion, is presented.

Force solutions for non-redundantly actuated 3-*RRR*, 3-*RRR*, 3-*RPR* and 3-*RPR PM*s are formulated in terms of screw coordinates. The reciprocal product of screw coordinates is demonstrated to be invarient under changes in reference location and orientation. As examples, the *PM*s execute basic circle, logarithmic spiral and arc displacement and force trajectories. All non-redundantly-actuated *PM*s, encounter two

backlash-prone zero-actuator-output configurations when executing any of the trajectories. Therefore, non-redundantly actuated *PM*s are found inadequate for precision applications.

Force-uncertainties, where *PM*s cannot sustain or apply forces in uncertain directions, are examined. For typically actuated 3-*RRR* and 3-*RPR PM*s, force uncertainties are identified using screw system arguments based on the existance of 3 actuated forces forming degenerate (rank = 2) planar pencils of forces. These degenerate force pose make arbitrary force and moment application impossible and cause singularities in the force solutions.

The working area of the 3-*RRR PM* is found compatible with all trajectories. This compatibility is due to zero minimum branch length being possible with the limitless angular displacements possible with stacked *R* joints. In comparison, the 3-*RPR PM* with minimum joint lengthes imposed on the *P* joints, has a smaller working area, and is not compatible with any of the trajectories. A *P* joint modification allowing relative length minimums of zero and a compatible working area identical to the 3-*RRR PM*, is considered.

To address inadequacies, symmetric actuation-redundant 3-*RRR* and 3-*RPR PM*s are considered. Pseudo (right Moore-Penrose) inverse of the 3×6 *ARS* (associated reciprocal screw) matrix is considered to solve for the required actuation. This solution, while providing a minimum 2-norm of the vector of required actuator outputs, does not reduce backlash-prone configurations with all actuators still having two backlash-prone zero-output configurations.

An algorithm for reducing backlash, using *MATLAB*'s constrained optimization routine *FMINCON* is applied. Minimizing the 2-norm of the vector of actuator outputs, subject to the backlash-free constraint of having outputs ≥ 0 or ≤ 0 depending on the initial values, is considered. Actuators providing the best conditioned *ARS* matices are utilized for the particular solutions.

Table of Contents

List of Figures

List of Tables

Acknowledgements

I would like to thank my Former supervisor Dr. Ron P. Podhorodeski and supervisor Dr. Yang Shi, for their support and guidance throughout this Dissertation. Furthermore, I would deeply express my gratitude to Ron for introducing me to the fascinating world of kinematics but mostly for tutoring me through diverse aspects of the academic life.

I want to extend my gratitude to my committee members, Dr. Daniela Constantinescu, Dr. Wu-Sheng Lu and Dr. Zuomin Dong, for their comments and suggestions.

I would like to thank my external examiner, Dr. M. John D. Hayes, who has exceptional expertise in kinematics of manipulators. I am truly honored to have him as my external examiner.

I would also like to thank Dr Roger Boudreau for the initial work on the 3-*RRR* parallel manipulator system.

I would like to thank my fellow students, in particular the former and current members of the Robotics and Mechanisms Laboratory, for the numerous discussions that we have had regarding topics related to my Dissertation and especially for embracing me in such a delighting working environment.

I would like to acknowledge the Natural Sciences and Engineering Research Council (NSERC) of Canada whose financial support has made my research possible.

I would like to thank my special friend Felix Li for all of his support, it will always be in my mind.

Finally, I would like to thank my family for their unconditional love and support that allows me to reach goals beyond my expectations and all my friends in my life for their enormous encouragement and their absolute confidence in me throughout my life.

Chapter 1

Introduction

1.1 Goals of the Research

The reduction of backlash in parallel manipulators (*PM*s) through the use of actuation redundancy will be investigated. Inaccuracies due to backlash are partially due to actuators' output sign-switching during manipulation. For examples of sign-switching see the non-redundant *PM* static force formulations (Chapter 2) and the non-redundant static force applications (Chapter 3). Drive-train component clearances in joints, mechanical assembly, and motors and reducers are partially responsible for backlash. This Dissertation concentrates on backlash due to motors and reducers. Zero-actuator output occurs when actuators switch signs, i.e., go from positive to negative or vice-versa. These zero-actuator outputs are prone to backlash as the manipulator end-effector is free to drift within the clearances present in the zero-output actuators, i.e., motors and reducers.

Using actuation redundancy (more actuators than required for a task) to pre-load the actuators' outputs has been found in this research to be effective for reducing actuator output sign-switching (see actuation redundancy examples of Chapters 4 and 5). Research in this Dissertation has demonstrated that preloading is effective for reducing sign switching in 3-*RRR*[1] and 3-*RPR*[1] planar *PM*s. These results have been reported in one conference paper (Mao and Podhorodeski (2010)), one journal paper (Boudreau, Mao, and Podhorodeski (2012)), and one submitted journal paper (Mao and Podhorodeski (2012)).

In this work, accuracy enhancement through backlash reduction is considered. A non-redundantly actuated *PM* subject to a wrench (a force and moment system (Ball (1900), Hunt (1978)) while following a trajectory requires actuator-output forces (torques for *R* joints, forces for *P* joints) where sign-switching may occur. If backlash is present in the actuation hardware for the manipulator, output force sign-switching compromises accuracy.

[1] Within the *PM* descriptions, the preceding number indicates the number of branches, *R* denotes a revolute joint, *P* a prismatic joint and the underline indicates the actuated joint(s).

1.2 Literature Review

*PM*s are being used for manufacturing tasks that require high precision. Clearances in mechanical joints induce backlash (when actuator output sign-switching occurs) and can prevent a manipulator from performing at the desired level of accuracy. In this section, literature related to parallel manipulator analysis and design, backlash reduction, the considered *PM*s, and *PM* redundant encoding and acuation, are reviewed.

1.2.1 *PM* Analysis and Design

Hunt (1983) discussed the analysis and structural kinematics of in-parallel-actuated robot arms pointing out the stiffness and accuracy advantages of in-parallel actuation in comparation to serial actuation. Gosselin and Angeles (1988) discussed the optimal design of *PM*s that are based on 3-*RRR* joint layouts. Merlet (1993) considered the state of the art for *PM*s. Within Merlet (1996a) forward displacement solutions (*FDS*s), for planar *PM*s are formulated. Gosselin *et al*. (1996) presented a new architecture for planar 3 degree-of-freedom (*DOF*) *PM*s. Leguay-Durand and Reboulet (1997) discussed the optimal design of a redundant spherical *PM* finding that actuation redundancy removes singularities and improves dexterity within an enlarged workspace volume. Ryu *et al*. (1998) presented an over-actuatated (redundantly actuated) *PM* used for rapid machining. Carretero *et al*. (2000a) discussed the kinematic analysis and optimization of a three-degee-of-freedom spatial *PM*. The *PM* of Carretero *et al*. (2000a) has reduced 3-*DOF* motion capability in comparison to a full-spatial *PM*. Dimensions reducing inacurate

motions (termed parasistic motions) are found for submerged underwater vehicle (*SUV*) applications.

Chiacchio *et al.* (1991) introduced manipulability ellipsoids for multiple-arm robots. Ellipsoids can be defined for both velocity and force application. Let $v = \{v_x, v_y\}^T$ and ω_z be the velocity of the end-effector with v_x and v_y being *X* and *Y* translational velocity components and ω_z being a *Z* direction angular velocity. Similarly let $f = \{f_x, f_y\}^T$ and m_z be a force applied by the end-effector with f_x and f_y being *X* and *Y* force components and m_z being a moment in the *Z* direction applied by the end-effector. A velocity ellipsoid is defined by $(v^T v)^{1/2} = v_{max}$ for a specified ω_z, and a force ellipsoid is defined by $(f^T f)^{1/2} = f_{max}$ for a specified m_z. Different velocity and force directions are searched to define the magnitudes of the corresponding ellipsoids. Major and minor ellipsoid axis directions correspond to maximum and minimum velocity or force capability directions. Similarily, Bicchi A. *et al*. (1995) defined mobility and manipulability elliposoids for multiple-limb robots.

Zanganeh and Angeles (1997) considered kinematic isotropic design of a planar 3-*RRR* and a spatial 6-*UP*S *PM*. Isotropy of a *PM* Jacobian, *J*, matrix means that $J^T J = I$, where *I* is a 3×3 identity matrix for a planar manipulator and a 6×6 identity matrix for a spatial manipulator. In terms of ellipsoids, equality to an identity matrix, indicates that the corresponding ellipsoid would be a 3-*D* sphere for 3-dimensions (planar applications) or a 6-*D* hyper-sphere (spatial applications). Due to dimensional inconsistency Zanganeh and Angeles (1997) considered the Jacobian to consist of one part related to orientation

and a second part related to translation. Two scaling factors are introduced to dimensionally homogenize dimensional inconsistancies.

Zhang *et al.* (2004) considered the optimal design of over-actuated parallel kinematic toolheads with genetic algorithms. Objectives of maximum global stiffness and workspace volume are introduced. A "Tripod" 3-*PRS PM*, where the *P* and *R* joints are perpendicular, providing 3-*DOF* of motion is suggested to be combined with a 2-*DOF X-Y* platform to supply a total of 5 motion *DOF*. (Note 5 motion *DOF* are sufficient for machining). A genetic algorithm is used to optimize the manipulation system for the before mentioned stiffness and workspace objectives. Pinto *et al*. (2010) demonstrated a general methodology for stiffness modeling and suggests that *PM* stiffness could be used as a design index. Zhang *et al*. (2011) focused on the importance of effective performance indices and proposes methods to set up control systems for *PM*s.

1.2.2 Effect of Clearances on Accuracy

Clearances in mechanical components can lead to end-effector inaccuracies and *PM* backlash. *PM*s are multiple-input, multiple-loop mechanisms. Therefore, research on the effect of joint clearances on mechanism accuracy is of interest. Innocenti (2002) considered the accuracy sensitivity of spatial assemblies including *R* joints with clearances. Parenti-Castelli and Venanzi (2005) considered the influence of both *R* and *P* joint clearances on the accuracy of mechanisms.

Briot and Bonev (2008) performed an analysis of the accuracy of 3-*DOF* planar *PM*s studying the effect of inaccuracies of the inputs on the accuracy of the output payload platform. Briot and Bonev found that to have a local maximum of inaccuracy of the output, at least two of the three inputs would have to have maximum inaccuracy. The *PM*s considered included the planar 3-*RPR* and the 3-*PRR*. Chebbi *et al*. (2009) performed analysis to predict the end-effector pose-errors caused by joint clearances for 3-*UPU* (where *U* is a passive universal joint, equivalent to 2 intersecting *R* joints), parallel robots.

Actuator preloading is an effective way to reduce the effects of clearances. In this Dissertation actuator preloading is investigated for the reduction of backlash in 3-branch planar *PM*s. In Section 6.5, it is recommended that the effect of joint preloading on clearance induced mechanism inaccuracies should be investigated.

1.2.3 Actuator Preloading and Backlash Management

Inaccuracies due to backlash are reduced if there is no sign switching in the control forces. Redundancy has been proposed to ensure no sign switching. Müller (2005) and Müller and Maisser (2007) considered additional branch redundant-actuation (a planar 4-*RRR* *PM* and a spatial hexapod). They avoided backlash by considering Lagrangian motion equations and inverse dynamics, allowing internal pre-load control and backlash reduction for certain trajectories and joints.

Lotfi *et al*. (2010) sacrificed the accuracy of platform orientation to ensure single direction (backlash-free) motion in the *x* and *y* working area of a planar *3-RPR PM*. The working area of Lotfi et al. has a reduced dimension, i.e., only 2 translational *DOF* and therefore has actuation redundancy with the *3-RPR PM*. The working area considered by Lotfi *et al*. (2010) is restricted to a singular-free circular area, and the working area is further limited since stop-reverse-direction actuator inputs are not allowed.

Wei and Simaan (2010) proposed using pre-loaded springs at the wrist joints of a planar 3-*PRR PM* (where an enlarged underlined font for the wrist joint has been used to indicate a joint pre-loaded by a spring.) This spring pre-loaded device was found to reduce backlash for a range of external forces. The pre-load magnitude was determined to ensure no actuator sign switching (backlash-free motion) within the range of external forces. The necessary torsional pre-loads for the method of Wei and Simaan (2010) are determined by formulating a Lagrange problem that minimizes the elastic energy of the robot.

Müller (2010) utilized actuation redundancy to achieve backlash avoidance. Geometric imperfections (model uncertainties) were found to cause parasitic perturbations that cannot be compensated by *PD* (proportional and derivative) and computed-torque control. Müller (2011) proposed an amended version of *PD* and computed-torque control that are not affected by geometric imperfections.

Müller (2011) noted that redundant actuation can reduce singularities, improve dexterity, and allow optimal force distribution and stiffness control, and backlash avoiding control. However, as mentioned above, Müller found that kinematic model

uncertainties lead to parasitic perturbation forces that cannot be compensated by ordinary *PD* control. Amended versions of *PD* and computed torque control are proposed. Müller (2011) amended *PM* control involves including tracking error $q_e(t) = q(t) - q_d(t)$, where $q(t)$ is the actual joint displacement value, $q_d(t)$ is the desired value, $q_e(t)$ is the tracking error and t is time. Including the tracking error and its first and second derivatives within a *PD* controller resulted in a controller Müller (2011) demonstrated to be stable for geometric imperfections when considering stiffness (force capability) control and implementing actuation redundancy for limiting backlash.

Müller and Hufnagel (2012) proposed a computed torque and augmented *PD* control scheme in redundant coordinates which does not require coordinate switching. The scheme is robust using pseudo-inverses of rank-deficient matrices. Experimental results were presented for a planar 2-*DOF* redundantly-actuated *PM*.

1.2.4 Monolithic Flexure Joints

Monolithic flexure joints have been proposed to replace mechanically assembled joints that have inaccuracies due to manufacturing tolerances (see for example: Yi *et al*. (2003), Pham and Chen (2004) and Kang *et al*. (2005)). Monolithic flexure joints will reduce backlash but have very limited range of displacements limiting the available *PM* workspace.

1.2.5 *PM*s Considered in this Research

The non-redundant versions of the considered *PM*s can be considered to be planar versions of the *PM*s introduced by Gough (1965) and Stewart (1965a). Gough introduced a 6-*UPU PM* intended for transportation tire testing, where *U* stands for a passive universal joint (equivalent to two orthogonal intersecting passive *R* joints). The tire testing apparatus of Gough is documented in reports by Gough dating back to 1965. As pointed out by Stewart (1965b) the tire testing apparatus of Gough (1965) should not function as a spatial (6 motion *DOF*) device since each leg only has 5 = 2 (due to first *U* joint) + 1 (due to *P* joint) + 2 (due to last *U* joint) motion *DOF*. Stewart correctly surmised that Gough's 6-*UPU* tire testing *PM* functioned only due to the additional passive rotary motion allowed along the direction of the hydraulic cylinder (the *P* joint in each branch) by the pistons of each cylinder. In effect the additional rotation allowed by the hydraulic cylinder piston in each branch caused Gough's tire testing device to be a 6-*UPS* device where *S* stands for a passive spherical joint (equivalent to three orthogonal intersecting passive *R* joints).

Stewart (1965a) proposed a flight simulator based on 3 branches. Each branch had an actuated vertical *R* joint followed by a perpendicular intersecting passive *R* joint followed by a perpendicular actuated *P* joint, and finally followed by a passive *S* joint connecting a payload platform to each of the branches. Using the above *PM* notation is a 3-*RRPS PM* where the first three joints are sequentially perpendicular. Stewart (1965a) also proposed a fully-parallel (one actuator per branch) 6-*UPS PM* again intended for flight simulation. Note that *PM*s based on 6-*UPS* layouts are often referred to as Stewart-Gough platforms.

Also note that many flight simulators today are based on the 6-*UPS PM* layout of Stewart (1965a).

Within this work, in-branch actuation redundancy is utilized to reduce backlash induced inaccuracies at the actuated joints of a planar *PM*. In particular, the 3-branch (*3-RRR*) *PM* considered by Gosselin and Angeles (1988) is in-branch redundantly actuated resulting in a 3-*RRR PM*. Figure 1.1 is a typical 3-*RRR PM*. The research is then extended to 3-*RPR PM*s, i.e., *PM*s having an actuated prismatic 2^{nd} joint. Figure 1.2 shows a typical 3-*RPR PM*. While requiring the actuation of the 2^{nd} joints of the device, the actuation of these 2^{nd} joints reduces the actuator output forces (toques for both the 3-*RRR* and the 3-*RPR PM*s) required of the branch 1^{st} joints (base joints) requiring smaller actuators.

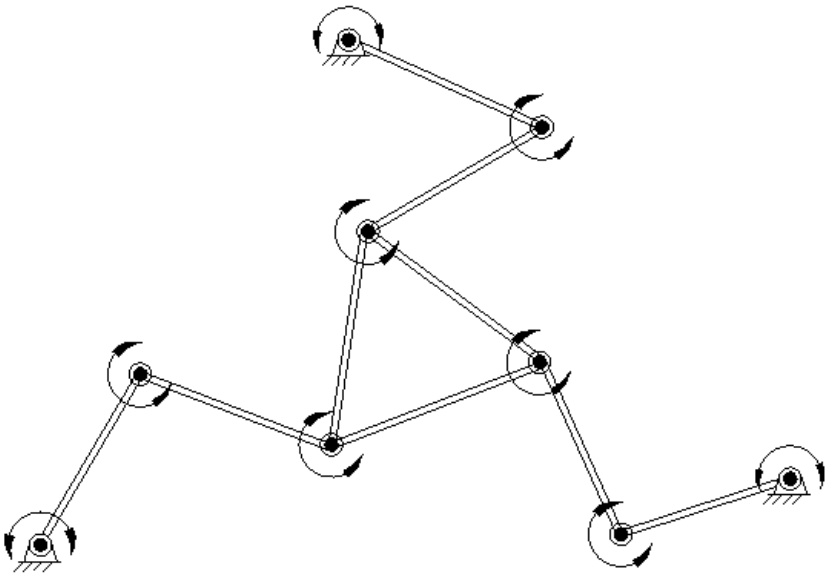

Figure 1.1: The Typical 3-*RRR* Planar *PM*.

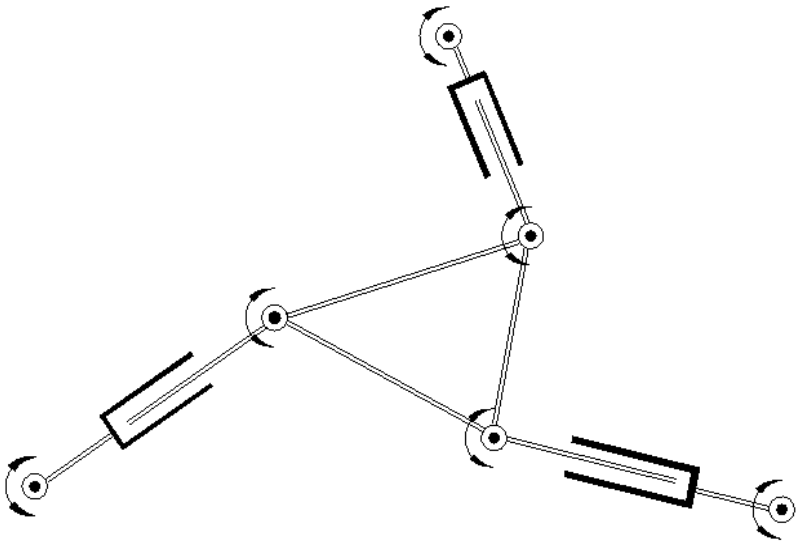

Figure 1.2: The Typical 3-*RPR* Planar *PM*.

1.2.6 Redundancy in *PM* Components

Redundancy in *PM* components has been considered by numerous researchers. Merlet (1996b) considered the advantages of *PM*s with redundant actuation. There are several forms of this redundancy. Redundant in-branch actuation (e.g., Firmani and Podhorodeski (2004) and redundant additional branch actuation (e.g., Firmani *et al*. (2007)) have been investigated for the reduction of *PM* force unconstrained configurations.

Zibil *et al*. (2007) considered an analytical optimization method for determining force moment capabilities of redundantly-actuated planar *PM*s. The weighted sum of the squares of the output (x and y) force and the output (z) moment components was used as

the objective function for the optimization. The analytical method involved expressing the static solution in terms of scaling factors, taking the derivative with respect to the scaling factor multiplier, setting the derivative equal to zero, and solving for the optimal multiplier.

Kotlarski *et al*. (2010) considered the use of discrete and continuous optimization strategies with an objective function of minimization of the maximal homogenized pose error for kinematical redundant *PM*s. "Homogenized pose error" means that a unit-corrected weighting based on the perceived value of translational pose error versus orientation pose error is used. The *PM* considered by Kotlarski *et al*. (2010) is the planar 3(*P*)*RRR PM* introduced by Ebrahimi *et al*. (2007) where the notation "(*P*)" means that there is one branch with an additional actuated *P* joint proximal to the base. Although this planar *PM* has four actuators, it does not have actuation redundancy since one branch is kinematically redundant, i.e., four joints would have to be actuated in the *PM* to have the end-effector location known. In conclusion, the work of Kotlarski *et al*. (2010) found that discrete optimization can work as well as continuous optimization, for certain examples. Backlash reduction is not considered in Kotlarski *et al*. (2010).

Weihmann *et al*. (2012) developed an optimization method based on a modified evolutionary approach to maximize output force capabilities of a 3-*RRR PM*. All potential assembly modes, i.e., elbow-up or elbow-down for each branch ($2^3 = 8$ different modes) were considered. The search involved 30,000 function evaluations in 30 runs to allow consideration of different assembly modes and different start points. Differential refers to the mutations used in the evolution process, and modified is the adaptive method

used in tuning update parameters. The analytical method of Zibil *et al*. (2007), in comparison, is more efficient and exact, but only considered the "elbows-up" assembly mode. Backlash reduction was not considered in the work by Weihmann *et al*. (2012) or in the work by Zibil *et al*. (2007).

Kinematically redundant branches (e.g., Ebrahimi *et al*. (2007)) have been considered to enhance workspaces and reduce singularities of *PM*s. Wu *et al*. (2009) considered controlling a non-redundantly actuated *PM* with position control and controlling the redundant actuation of the *PM* with force control. Within Wu *et al*. (2009) it was proposed to place non-redundantly actuated *PM*s in an uncertainty configuration to allow redundant actuation to have an effect on the redundantly-actuated *PM*'s pose. *PM*s with redundant actuation are noted to have: increased mobility; force unconstrained poses reduced, and to have the capability of modulating end-effector stiffness with internal-force control. Within Wu *et al*. (2009) Gruebler mobility analysis (Erdman and Sandor (1996)), inverse displacement analysis, Jacobians for velocity analysis and derivatives for acceleration formulation are utilized. Backlash reduction is not considered in the work by Wu *et al*. (2009).

Wu *et al*. (2009) considered the dynamics and control of a 3-*DOF PM* with actuation redundancy. The manipulator consisted of two 5-link loops where the end effecter was a common link. In summary, each loop consisted of the 1 common end effecter link + 2 prismatic links + 1 base link + 1 fixed length link = 5 links per loop. Each loop also has 1 prismatic joint + 4 revolute joints. So far the device is similar to two four-bars with variable length inputs (the prismatic joints). This planar device, for both loops, would

have two inputs and would be capable of controlling the position of the common end-effector link, i.e., this is not an actuation redundant 3-*DOF* device.

The actuation redundancy for the two loop *PM* of Wu *et al*. (2009) is due to the before described base joints being pistons with controllable vertical movements. The net effect is that there are a total of four actuated *P* joints within the two loop 3-*DOF* device, i.e., it has an actuation degree of redundancy (*DOR*) of one. Wu *et al*. (2009) apply this *DOR* of one to minimizing $\boldsymbol{\tau}^{T}\boldsymbol{\tau}$ were $\boldsymbol{\tau}$ is the 4×1 vector of prismatic joint forces. Wu *et al*. (2009) did not utilize actuation redundancy to reduce backlash.

Pashkevich *et al*. (2011) presented a methodology for modeling the stiffness of *PM*s including passive joints. A non-linear stiffness model was introduced for manipulators with passive joints. To model the stiffness, manipulator elements are presented as pseudo-rigid bodies separated by multi-dimensional virtual springs and perfect passive joints. Pashkevich *et al*. (2011) did not utilize actuation redundancy to reduce backlash.

Xu *et al*. (2012) considered elastic deformation while formulating the inverse force problem of redundantly-actuated *PM*s. Compatibility equations of elastic deformation are derived considering conservation of energy. Xu *et al*. (2012) then discussed whether internal forces exist within the pseudo-inverse solution to the inverse dynamics of redundantly actuated *PM*s. Finally, appropriate actuated forces are obtained to coordinate the elastic deformations and avoid destruction of a 2-*S*<u>*P*</u>*S* + *R* forging manipulator. Note "*S*" is a passive spherical (3-*DOF* rotary joint) and "+ *R*" is a revolute joint connected to the coupling link joining the two *SPS* branches. Xu *et al*. (2012) did not utilize actuation redundancy to reduce backlash.

1.3 3-*RRR* and 3-*RPR PM*s: Layouts and Dimensions, Actuated Joint Limits and *PM* Working areas

1.3.1 3-*RRR* and 3-*RPR PM*s: Section Overview

As mentioned in Section 1.2.4, the *3-RRR* and the *3-RPR PM*s will be the *PM*s used as examples in this Dissertation. Section 1.3.2 discusses the layouts and dimensions of the *3-RRR* and the *3-RPR PM*s. Section 1.3.3 considers actuated joint limits, develops a method for finding the working areas for planar *PM*s having a rotated payload platform, and presents working areas of the *3-RRR* and the *3-RPR PM*s.

1.3.2 Layouts and Dimensions

The 3-*RRR PM* layout is illustrated in Figure 1.3. Each branch consists of a base joint B_i, an elbow joint E_i, and a wrist joint W_i, i = 1, 2 and 3. The points B_1, B_2 and B_3 define a base platform of known location. The wrist joints, W_1, W_2 and W_3, are attached to and define a mobile payload platform. The elbow joints E_1, E_2 and E_3, effectively define the linear distance between B_1 and W_1, B_2 and W_2, and B_3 and W_3, respectively. The dimensions of the 3-*RRR PM* are as follows: $B_1B_2 = B_2B_3 = B_3B_1 = 0.6m$; $W_1W_2 = W_2W_3 = W_3W_1 = 0.3m$; and $B_1E_1 = B_2E_2 = B_3E_3 = 0.3m$, and $E_1W_1 = E_2W_2 = E_3W_3 = 0.3m$.

The 3-*RPR PM* is illustrated in Figure 1.4. Each branch consists of a base joint B_i, a prismatic joint P_i, and a wrist joint W_i, i = 1, 2, and 3. The points B_1, B_2 and B_3 define a base platform of known location. The wrist joints, W_1, W_2 and W_3, are attached to and

define a mobile payload platform. The prismatic joints P_1, P_2 and P_3 define the linear distance between B_1 and W_1, B_2 and W_2, and B_3 and W_3, respectively. The dimensions of the 3-*RPR PM* are as follows: $B_1B_2 = B_2B_3 = B_3B_1 = 0.6m$; and $W_1W_2 = W_2W_3 = W_3W_1 = 0.3m$. The prismatic joints, P_1, P_2, and P_3 have lengths that are indivdually controlled to be within 0.3 to 0.6*m*.

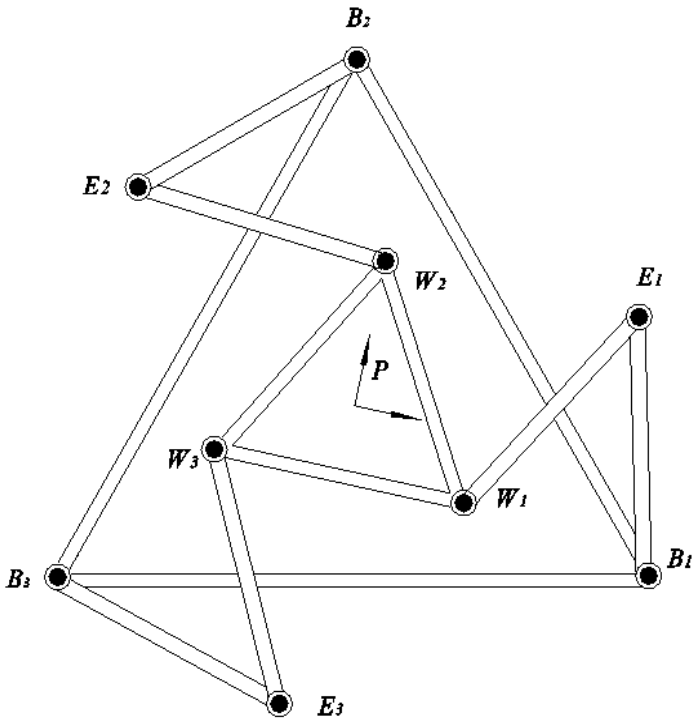

Figure 1.3: The 3-*RRR PM* Layout.

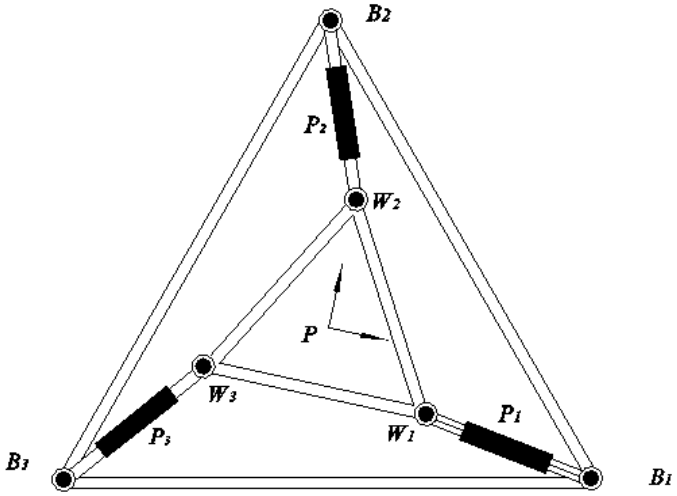

Figure 1.4: The 3-*RPR PM* Layout.

1.3.3 Joint Limits and *PM* Working areas

The revolute joints, both actuated and passive (non-actuated) are considered to be capable of full rotation. This full rotation can be easily achieved by stacking the links seperated by revolute joints. Note that this stacking will cause the links to operate in separate planes, but these planes will be parallel. All links operating in parallel planes are a characteristic of a planar mechanism (Erdman and Sandor (1996)). The 3-*RRR* and 3-*RPR PM*s are planar manipulators formed from planar mechanisms. Prismatic joints are the 2nd joints of the branches of the 3-*RPR PM*s. These prismatic joints are able to initially vary individually between 0.3 to 0.6*m*.

Gosselin (1988) determined planar 3-*RRR PM* working areas using a graphical concentric circular construction. Gosselin (1988) is recognized as being the original work on working area determination. Williams II and Joshi (1999) presented a planar

PM working area construction for no rotation of the payload platform based on the working area (volume) determination method of Gosselin (1988, 1990). The working area construction for planar *PM*s of Williams II and Joshi (1999) can be summarized as:

1) For each branch draw circles about the branch base point of radius of the minimum and the maximum reach of the branch (this would be 0.0 and 0.6*m* for the 3-*RRR PM* and 0.3 and 0.6*m* for the 3-*RPR PM*). This will create one set of three circles (the minimum length is 0.0*m* creating no circles) for the 3-*RRR PM* and two sets of three circles for the 3-*RPR PM*.
2) The working area is defined by the circles intersected or by the circles alone if they do not intersect.

The workspace construction of Gosselin (1990) is for spatial *PM*s and for any payload platform orientation. Gosselin (1990) considered a 6-*UPS PM* for a known payload-platform orientation and for minimum and maximum *P* joint lengths. Considering different elevations (Z values) with X = Y = 0.0, and either the minimum or maximum *P* lengths, volume edges were found for each individual *UPS* kinematic chain. Intersecting the work-volume edges for each elevation provides the working area for that elevation and for minimum or maximum *P* lengths. Subtracting the elevation-specific working area found with minimum *P* lengths (points within this volume are unreachable) from the working area found at the same elevation considering maximum *P* lengths provides the reachable working area at the elevation. Considering all reachable elevations, a work-volume is determined for a specific payload-platform angle and X = Y = 0.0. The process can be repeated for other payload-platform orientations and for other X and Y

displacements. Note that within the construction of Gosselin (1990), no limits are placed on the displacements of the rotary joints.

Gosselin and Jean (1996) developed an algorithm accounting for joint limits on active P joints and passive *R* joints in the working area determination of a planar 3-*RPR PM*. Limiting arcs and line segments are considered in Cartesian space to define the reach limits for each kinematic chain (each *RPR* is a kinematic chain) and edges for the working area of the individual kinematic chain. Intersection of the individual work-volume edges provides the working area for the 3-*RPR PM*. .Similarly, Carretero *et al*. (2000b) present a method for determining the work volume for a 3-*DOF PM* allowing X and Y translational and roll angular motion.

The construction of Williams II and Joshi (1999) feature a planar 3-*RPR PM* with zero payload platform rotation. The points below outline a *PM* working area determination method (similar to Gosselin (1988) and Williams II and Joshi (1999) working area construction methods), including a rotation of the payload platform utilizing a mechanism inversion:

1) Consider the payload platform to be fixed at an angle of no rotation;
2) Rotate the base attachment points, about the centre of the base attachment points, in the opposite direction to the rotation assigned to the payload platform. This base attachment point rotation is 30 degrees cw for the 30 degrees ccw rotation of the payload platforms for the considered *PM*s. This step is an inversion and preserves the relative rotation between the payload platform and the base attachment points;

3) Draw circles about the inverted base points of radius the maximum and the minimum reaching length (this would be 0.6*m* and 0.0*m* for the 3-*RRR PM* and 0.6*m* and 0.3*m* for the 3-*RPR PM*). This will create one set of three circles (the minimum length is 0.0*m* creating no circles) for the 3-*RRR PM* and two sets of three circles for the 3-*RPR PM*.

4) The working area is the circles intersected or the circles alone if they do not intersect.

Figure 1.5 shows the circle construction to determine the working areas of the 3-*RRR* and the 3-*RPR PM*s. The working areas are highlighted by shading. The 3-*RRR* PM working area is due to 3 branches of two 0.3*m* revolute joint connected lengths, i.e., the branches vary between 0 and 0.6*m*. The working area for the 3-*RRR PM* is larger than the working area of the 3-*RPR PM* where the 3 branches vary between 0.3*m* and 0.6*m*. The darker area is the area that can only be reached by the 3-*RPR PM*. The points B'_1, B'_2, and B'_3 on Figure 1.5 are the inverted base pin locations.

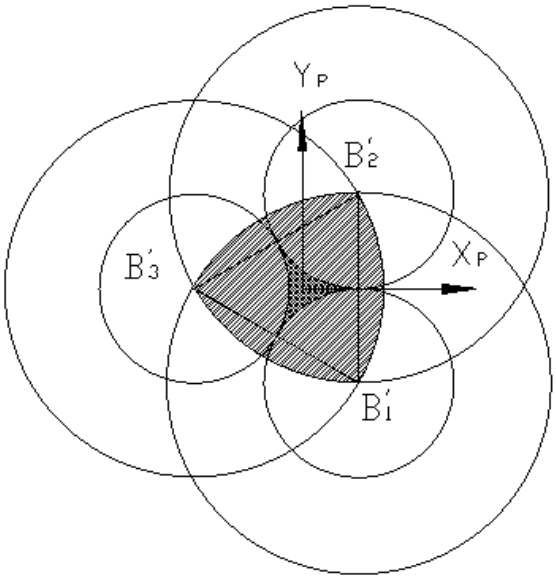

Figure 1.5: 3-*RRR* and 3-*RPR PMs* Working Area Constructions for Payload Platform Orientation of 30 ccw.

1.4 Organization of the Remaining Dissertation

Chapter 2 formulates the inverse static force problem for non-redundant *PM*s, solving for required actuated forces (torques for actuated revolute joints or forces for actuated prismatic joints), for a known end-effector force. In Chapter 3, circle, spiral and arc force trajectories are derived for cutting. Inverse static force solutions are found for the non-redundantly actuated *PM*s executing the circle, spiral and arc cutting trajectories. These non-redundantly actuated *PM*s are observed to have backlash-prone zero-actuator-output configurations.

In Chapter 4, redundant actuation is considered to reduce backlash-prone configurations. Pseudo-inverses solutions are found to still require as many backlash-prone configurations as the non-redundantly actuated *PM*s. To reduce backlash, non-reversing actuator-outputs using null-space-based projection of sacrificial elbow torques, non-reversing joint-output force constraints, and *MATLAB*'s *FMINCON* (a sequential programming optimization routine) is applied.

Chapter 5 considers finding backlash-free wrench intensity results for redundantly-actuated *PMs* performing the circle, spiral and arc force trajectories. Both the 3-*RRR* and 3-*RPR PMs* are considered. Discussions, high-lighting the contributions made within Chapters 2 through 5, are included as final sections in each chapter. Chapter 6 summarizes contributions made in the Dissertation, makes conclusions and recommendations for further research.

Chapter 2

Static Force Problems for Non-Redundantly Actuated *PM*s

2.1 Overview of Chapter 2

*PM*s and reference frames considered in the examples of this Dissertation are presented in Section 2.2. Expressing static force problems for non-redundantly actuated *PM*s with associated reciprocal screws (*ARS*s), wrench intensities and reciprocal products are considered in Section 2.3. The presentation is in terms of screw quantities and screw coordinates. Hunt (1983) and Roth (1984) discussed relevant screw quantity terminology. Planar *PM*s and their reciprocal screw quantities are described in Section 2.4. The static force problems for the non-redundantly actuated 3-*RRR*, 3-*RRR*, 3-*RPR* and 3-*RPR*

planar *PM*s are considered in Section 2.5. A discussion on the formulations presented in this chapter is given in Section 2.6.

2.2 Example *PM*s and Frames of Reference

Figure 1.3 depicts a symmetrical 3-*RRR PM* with the labeling B_i, E_i, and W_i, being the base, elbow and wrist joints of the i^{th} branch, i = 1, 2, and 3. Figure 1.4 depicts a symmetrical 3-*RPR PM* with the labeling B_i, P_i, and W_i, being the base, prismatic and wrist joints of the i^{th} branch, i = 1, 2, and 3. Appendix A presents forward displacement solutions (*FDS*s) and Appendix B presents inverse displacement solutions (*IDS*s) for the 3-*RRR* and 3-*RPR PM*s.

For both *PM*s, the platform reference frame $\{P\}$ is fixed to the mobile payload platform. The origin of $\{P\}$ is located at the center of the three passive wrists: W_1, W_2 and W_3. Frame $\{P\}$'s X-direction X_P is the direction from W_3 to W_1 and its Y-direction Y_P is defined by the location of W_2. Finally: $Z_P = X_P \times Y_P$. The platform reference frame $\{P\}$ is illustrated in Figures 2.1 and 2.2.

For both *PM*s, the base reference frame $\{B\}$ is fixed to the base platform. The origin of $\{B\}$ is located at the center of the three base joints: B_1, B_2 and B_3. Frame $\{B\}$'s X-direction X_B is the direction from B_3 to B_1 and its Y-direction Y_B is defined by B_2. Finally: $Z_B = X_B \times Y_B$.

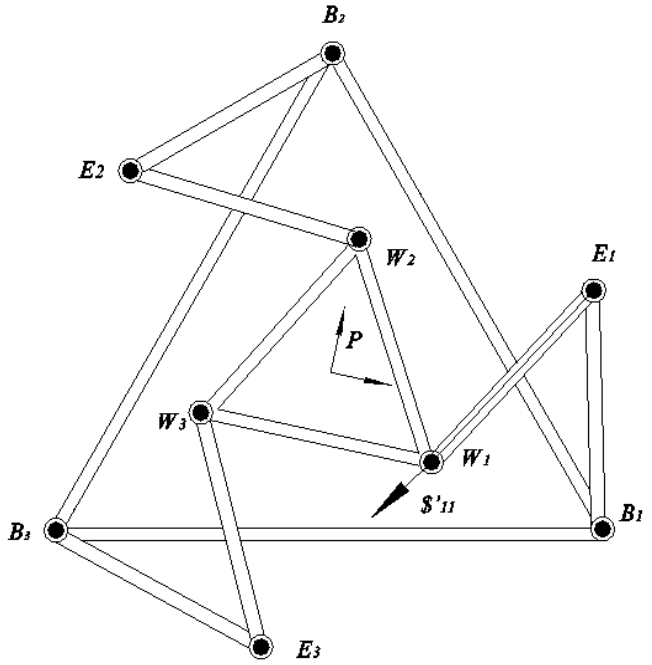

Figure 2.1a: 3-*RRR PM* with Reference Frames and *ARS* $\$'_{11}$.

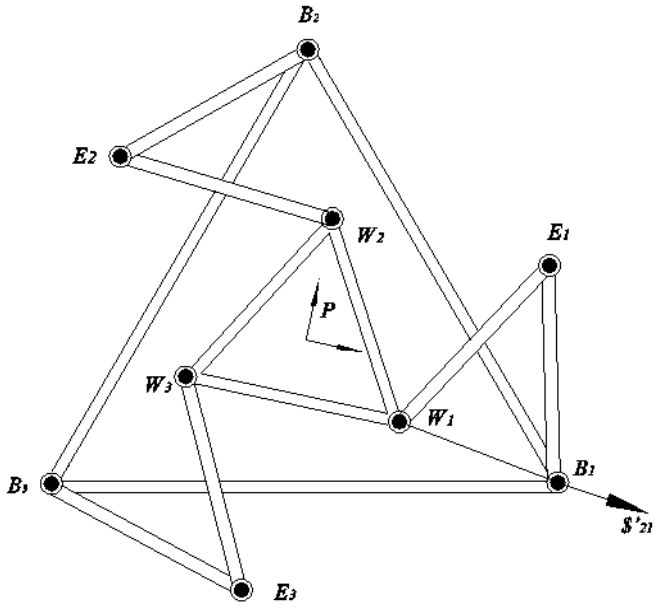

Fig 2.1b: 3-*RRR PM* with Reference Frames and *ARS* $\$'_{21}$.

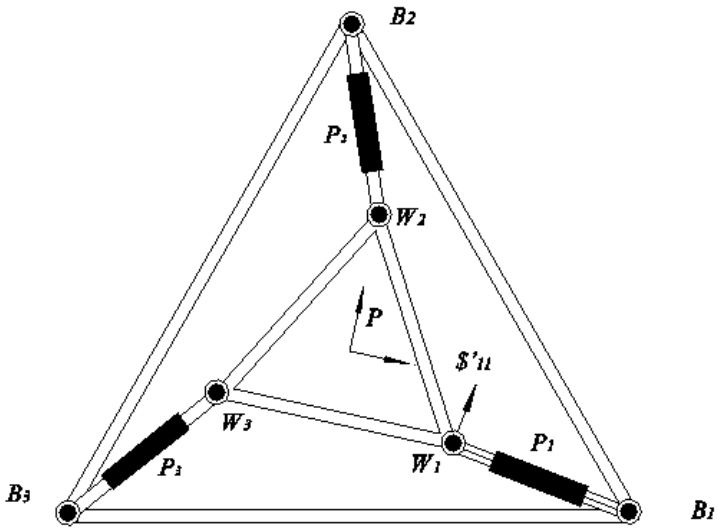

Figure 2.2a: 3-*RPR PM* with Reference Frames and *ARS* $'$_{11}$.

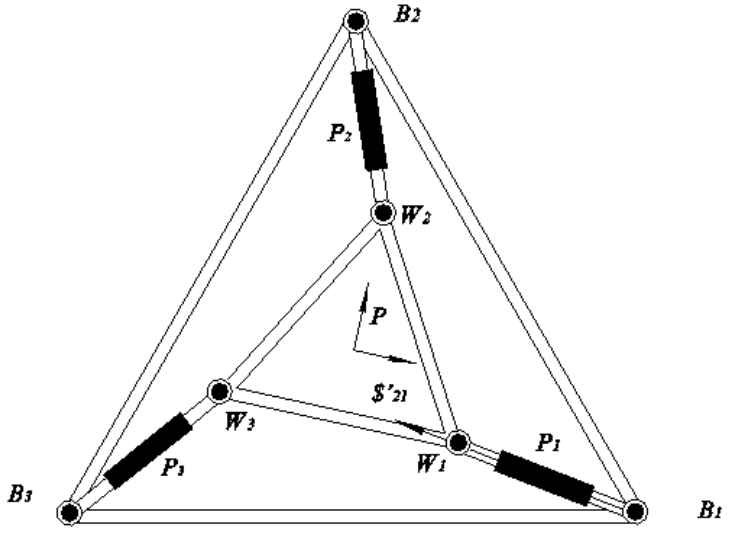

Figure 2.2b: 3-*RPR PM* with Reference Frames and *ARS* $'$_{21}$.

2.3 Expressing Force Problems with Associated Reciprocal Screws, Wrench Intensities and Reciprocal Products

Assume ${}^{p}\mathbf{F} = {}^{p}\{f_x, f_y; m_{zp}\}^T = {}^{p}\{\boldsymbol{f}; m_{zp}\}^T$ is a wrench composed of a force and a moment to be applied by the manipulator. ${}^{p}\mathbf{F}$ is known with respect to (wrt) frame $\{P\}$. ${}^{p}\mathbf{F}$ has force components: ${}^{p}\boldsymbol{f} = {}^{p}\{f_x, f_y\}^T$ in the x and y directions and a moment m_{zp} about the point p that is only in the Z-direction. From ${}^{p}\mathbf{F}$ a wrench ${}^{B}\mathbf{F}$ wrt frame $\{B\}$ can be found (Hunt 1978), i.e.:

$$ {}^{B}\mathbf{F} = \left\{ {}^{B}_{p}\boldsymbol{R}\,{}^{p}\boldsymbol{f}; \mathrm{z}\left(\{0,0,\mathrm{m}_{zp}\}^T + {}^{B}\check{\mathbf{r}}_{B-p}\,{}^{B}_{p}\boldsymbol{R}\,{}^{p}\boldsymbol{f} \right) \right\}^T . \qquad (2\text{-}1) $$

In Equation (2-1) ${}^{B}_{p}\boldsymbol{R}$ is a rotation matrix describing the orientation of $\{P\}$ wrt $\{B\}$, position vector ${}^{B}\mathbf{r}_{B\text{-}p}$ describes the location of the origin of $\{P\}$ wrt the origin of $\{B\}$ in terms of $\{B\}$'s orientation, ${}^{B}\check{\boldsymbol{r}}_{B\text{-}p}$ denotes the skew-symmetric 3×3 cross-product matrix of vector ${}^{B}\boldsymbol{r}_{B\text{-}P}$, and z( ) refers to the z-component of a vector quantity. Note that since a planar manipulator is being considered, ${}^{B}\check{\mathbf{r}}_{B\text{-}p}\,{}^{B}_{p}\boldsymbol{R}\,{}^{p}\boldsymbol{f}$ will only be in the Z-direction.

The 3×3 skew-symmetric cross-product matrix of $\boldsymbol{r} = \{r_x, r_y, r_z\}^T$ is

$$ \check{r} = \begin{pmatrix} 0 & -r_z & r_y \\ r_z & 0 & -r_x \\ -r_y & r_x & 0 \end{pmatrix} . $$

If force $\boldsymbol{f} = \{f_x, f_y, f_z\}^T$ then $\check{\boldsymbol{r}}\boldsymbol{f} = \{ -r_z f_y + r_y f_z,\ r_z f_x - r_x f_z,\ -r_y f_x + r_x f_y \}^T = \boldsymbol{r} \times \boldsymbol{f}$, i.e., the 3 × 3 skew-symmetric $\check{\boldsymbol{r}}$ when pre-multiplying a 3×1 vector is a cross-product operator.

Note that for a planar *PM*: $r_z = f_z = 0$, and therefore $\check{\boldsymbol{r}}\boldsymbol{f} = \{0, 0, -r_y f_x + r_x f_y\}^T$ only has a non-zero z value.

The position vector ${}^B\boldsymbol{r}_{B\text{-}P}$ and the rotation matrix ${}^B_p\boldsymbol{R}$ are variables and would be typically known from the required task.

The wrench ${}^B\mathbf{F}$ can also be expressed in terms of the wrench intensities, w_{ji}, and the associated reciprocal screws (*ARS*s), $\boldsymbol{\$}'_{ji}$, of the actuated joints. That is,

$$ {}^B\mathbf{F} = \sum_i \sum_j \mathbf{w}_{ji}\, {}^B\$'_{ji} \qquad j = 1 \text{ to } b_i,\ i = 1 \text{ to } b, \tag{2-2}$$

where b_i is the number of actuated joints in branch *i*, and *b* is the number of branches. The *ARS* ${}^B\boldsymbol{\$}'_{ji}$ is reciprocal to the all joints of branch *i* other than the actuated joint *j*. Appendix C summaries the screw coordinates of the *ARS*s of the 3-*RRR*, 3-*RRR*, 3-*RPR* and 3-*RPR PM*s wrt {*B*}.

The wrench intensity required at the j^{th} joint of branch *i* is w_{ji}. For a non-redundantly actuated *PM* the w_{ji} will form a 3 x 1 wrench intensity vector $\boldsymbol{w}_3$. The *ARS*s can be grouped in a 3x3 matrix: ${}^B\boldsymbol{\$}'_3$. Equation (2-2) can be expressed in matrix-vector form:

$$ {}^B\mathbf{F} = {}^B\$'_3\,\mathbf{w}_3. \tag{2-3}$$

Vector $\boldsymbol{w}_3$ can be solved by inverting ${}^B\boldsymbol{\$}'_3$ in Equation (2-3). The required joint torque τ_{ji} in terms of w_{ji}, ${}^B\boldsymbol{\$}'_{ji}$, and ${}^B\boldsymbol{\$}_{ji}$ is found by:

$$ \tau_{ji} = w_{ji}({}^B\$'_{ji} \circledast {}^B\$_{ji}), \tag{2-4}$$

where ${}^{B}\boldsymbol{\$}_{ji}$ are the screw coordinates of the j^{th} actuated joint of branch i and $\circledast$ indicates a reciprocal product, i.e.,

if $\mathbf{F} = \{f; \mathrm{m}\}^{\mathrm{T}} = \{f_x, f_y; m_z\}^{\mathrm{T}}$ and $V = \{\omega; v\}^{\mathrm{T}} = \{\omega_z; v_x, v_y\}^{\mathrm{T}}$ then:

$$\mathbf{F} \circledast \mathbf{V} = f \cdot v + m \cdot \omega = f_x v_x + f_y v_y + m_z \omega_z, \tag{2-5}$$

Within Equation (2-4), ${}^{B}\boldsymbol{\$}'_{ji} \circledast {}^{B}\boldsymbol{\$}_{ji}$ *i*s related to the mechanical advantage of the j^{th} actuated joint of branch i. It represents the perpendicular distance between $\boldsymbol{\$}'_{ji}$ and $\boldsymbol{\$}_{ji}$. The reciprocal product of a force and a velocity, as in Equation (2-5) has the units of rate of work, i.e., the units of power.

For an actuated prismatic joint j of branch i:

$${}^{B}\$_{ji} = {}^{B}\{0; \boldsymbol{a}_{ji}\}^{\mathrm{T}}, \tag{2-6}$$

where $\boldsymbol{a}_{ji}$ is the approach vector (z vector) of actuated joint j, i.e., it is the third column of ${}^{B}_{ji}\boldsymbol{R}$. The *ARS* for an actuated prismatic joint j of branch i is equal to:

$${}^{B}\$'_{ji} = {}^{B}\{\boldsymbol{a}_{ji}; 0\}^{\mathrm{T}}, \tag{2-7}$$

Therefore, for an actuated prismatic joint:

$$\$'_{ji} \circledast \$_{ji} = \boldsymbol{a}_{ji}^{\mathrm{T}} \boldsymbol{a}_{ji} = 1, \tag{2-8}$$

since $\boldsymbol{a}_{ji}$ is a unit vector. Note that the frame of reference (in this case $\{B\}$) does not matter to the unitary result of Equation (2-8) since the transforms of the screw quantities of Equations (2-6) and (2-7) to a different frame (say for example $\{P\}$) only involve a rotation matrix $\boldsymbol{R}$. The wrench intensity, w_{ji}, for a prismatic joint is equal to the actuator force, f_{ji}, i.e. :

$$f_{ji} = w_{ji}\left(\$'_{ji} \circledast \$_{ji}\right) = w_{ji}(1) = w_{ji}. \quad (2\text{-}9)$$

2.4 Reciprocal Screw Quantities

To explain the reciprocity of two screw quantities, consider a rigid body subjected to a twist and a wrench. If the wrench acting on the body does not contribute to the rate of work being done on the body twisting about a second screw, the wrench and the twist are said to be reciprocal (Hunt (1983) and Roth (1984)). If we consider a revolute, *R*, joint of a manipulator, a force with a line of action passing through the joint axis will not have an effect on the rotation about the *R* joint, and is therefore reciprocal to the *R* joint screw. In addition, a force couple perpendicular to an *R* joint screw (axis) is reciprocal to an *R* joint screw. In the case of a prismatic, *P*, joint the force's line of action has to be perpendicular to the *P* joint axis in order to be reciprocal to *P*. A pure force couple, however, is always reciprocal to a *P* joint because it can never have an effect on translation. When two screw quantities are reciprocal to each other, their reciprocal product, Equation (2-5), is zero.

In Figures 2-1a and 2.1b, $\$'_{11}$ and $\$'_{21}$ denote the associated reciprocal screws (*ARS*s) for the 1st and 2nd (base *R* and elbow *R*) actuated joints of Branch 1 of the 3-*RRR PM*. Similar *ARS*s exist for the actuated joints of Branches 2 and 3. *ARS*s are reciprocal to all joints in a branch except the actuated joint to which it is associated. Since only *R* joints are present in this manipulator, to be reciprocal the *ARS* of an actuated joint must be *0*-pitch and must intersect the other two *R* joints of the branch, i.e., $\$'_{11}$ intersects joints two

and three of branch one and $\$'_{21}$ intersects joints one and three of branch one. Appendix C presents the screw coordinates of the *ARSs* of the 3-*RRR* and 3-*RPR PM* wrt $\{B\}$.

In Figures 2.2a and 2.2b, $\$'_{11}$ and $\$'_{21}$ denote the *ARS*s for the 1st and 2nd (base *R* and second *P*) actuated joints of branch 1 of the planar 3-*RPR PM*. Similar *ARS*s exist for the actuated joints of branches 2 and 3. As illustrated on Figures 2.2, the second joint is prismatic and the first and third joints are revolute for each branch. Therefore, the *ARS* of the first joint of the first branch $\$'_{11}$, must be *0*-pitch and be perpendicular to the *P* joint and must intersect the wrist *R* joint. The *ARS* associated with the actuated prismatic joint, $\$'_{21}$, must be *0*-pitch and intersect the *R* joints one and three. Appendix C presents the screw coordinates of the 3-*RPR PM ARS*s wrt $\{B\}$.

2.5 Static Force Problems for the 3-*RRR*, the 3-*RRR*, 3- *RPR*, and 3-*RPR PM*s

2.5.1 3 -*RRR PM*

In terms of *ARS*s and wrench intensities, the static force problem (and the applied wrench ${}^{B}\mathbf{F}$) for a 3-*RRR PM* can be expressed as:

$$ {}^{B}\mathbf{F} = {}^{B}[\$'_{11}\ \$'_{12}\ \$'_{13}]\{w_{11}w_{12}w_{13}\}^{T} = {}^{B}\$'_{3a}\,\boldsymbol{w}_{3a}. \qquad (2\text{-}10) $$

The *ARS*, $\$'_{11,}$ is shown in Figure 2.1a. The screw coordinates for the *ARS*s ${}^{B}\$'_{11}$, ${}^{B}\$'_{12}$ and ${}^{B}\$'_{13}$ for the actuated base, B_i, *R* joints are given in Appendix C and have been

grouped as a 3x3 matrix ${}^{B}\boldsymbol{\$}'_{3a}$ in Equation (2-10). Inverting ${}^{B}\boldsymbol{\$}'_{3a}$ (Strang (1988)) allows $\boldsymbol{w}_{3a}$ to be found:

$$\boldsymbol{w}_{3a} = {}^{B}\$'_{3a}{}^{-1}\,{}^{B}\mathbf{F}. \tag{2-11}$$

The joint torques τ_{1i} are equal to the wrench intensities w_{1i} multiplied by their mechanical weighting factor as in Equation (2-4).

2.5.2 3 - *RRR PM*

An expression similar to Equation (2-10), using the *ARS*s and wrench intensities for the actuated elbow joints can be written for the 3-*RRR PM*, i.e.:

$${}^{B}\mathbf{F} = {}^{B}[\$'_{21}\ \$'_{22}\ \$'_{23}]\{w_{21}\,w_{22}\,w_{23}\}^{T} = {}^{B}\$'_{3b}\,\boldsymbol{w}_{3b}. \tag{2-12}$$

The *ARS*, $\boldsymbol{\$}'_{21,}$ is shown in Figure 2.1b. The screw coordinates of the ARSs ${}^{B}\boldsymbol{\$}'_{21}$, ${}^{B}\boldsymbol{\$}'_{22}$ and ${}^{B}\boldsymbol{\$}'_{23}$ for the actuated elbow, E_i, *R* joints are given in Appendix C and have been grouped as a 3x3 matrix ${}^{B}\boldsymbol{\$}'_{3b}$ in Equation (2-12). Inverting ${}^{B}\boldsymbol{\$}'_{3b}$ allows $\boldsymbol{w}_{3b}$ to be found:

$$\boldsymbol{w}_{3b} = {}^{B}\$'_{3b}{}^{-1}\,{}^{B}\mathbf{F}. \tag{2-13}$$

The joint torques τ_{2i} are equal to the wrench intensities w_{2i} multiplied by the mechanical weighting factor as in Equation (2-4).

2.5.3 3 - *RPR PM*

Again, an expression similar to Equation (2-10), using the *ARS*s and wrench intensities for the actuated base *R* joints can be written for the 3-*RPR PM*, i.e.,

$$ {}^{B}\mathbf{F} = {}^{B}[\$'_{11}\ \$'_{12}\ \$'_{13}]\{w_{11}w_{12}w_{13}\}^{T} = {}^{B}\$'_{3c}\boldsymbol{w}_{3c}. \quad (2\text{-}14) $$

The *ARS*, $\boldsymbol{\$}'_{11}$, is shown in Figure 2.2a. The screw coordinates of the *ARS*s ${}^{B}\boldsymbol{\$}'_{11}$, ${}^{B}\boldsymbol{\$}'_{12}$ and ${}^{B}\boldsymbol{\$}'_{13}$ for the actuated base *R* joints B_i of the 3-*RPR* planar *PM*, these *ARSs* are also given in Appendix C and have been grouped as a 3x3 matrix ${}^{B}\boldsymbol{\$}'_{3c}$ in Equation (2-14). Inverting ${}^{B}\boldsymbol{\$}'_{3c}$ allows $\boldsymbol{w}_{3c}$ to be found:

$$ \boldsymbol{w}_{3c} = {}^{B}\$'^{-1}_{3c}\,{}^{B}\mathbf{F}. \quad (2\text{-}15) $$

The joint torques τ_{1i} are equal to the wrench intensities w_{1i} multiplied by the mechanical weighting factor, as in Equation (2-4).

2.5.4 3 - *RPR PM*

Again, an expression similar to Equation (2-10), using the *ARS*s and wrench intensities for the actuated *P* joints can be written for the 3–*RPR PM*,

$$ {}^{B}\mathbf{F} = {}^{B}[\$'_{21}\ \$'_{22}\ \$'_{23}]\{w_{21}w_{22}w_{23}\}^{T} = {}^{B}\$'_{3d}\boldsymbol{w}_{3d}. \quad (2\text{-}16) $$

The *ARS*, $\boldsymbol{\$}'_{21}$, is shown in Figure 2.2b. The screw coordinates of the *ARS*s ${}^{B}\boldsymbol{\$}'_{21}$, ${}^{B}\boldsymbol{\$}'_{22}$ and ${}^{B}\boldsymbol{\$}'_{23}$ for the actuated joints P_i of the 3-*RPR PM* are also given in Appendix C and have been grouped as a 3x3 matrix ${}^{B}\boldsymbol{\$}'_{3d}$ in Equation (2-16). Inverting ${}^{B}\boldsymbol{\$}'_{3d}$ allows $\boldsymbol{w}_{3d}$ to be found:

$$ \boldsymbol{w}_{3d} = {}^{B}\$'^{-1}_{3d}\,{}^{B}\mathbf{F}. \quad (2\text{-}17) $$

The joint forces f_{2i} required of the prismatic joints are equal to the wrench intensities forces w_{2i} since ${}^{B}\boldsymbol{\$}'_{ji} \circledast {}^{B}\boldsymbol{\$}_{ji} = 1$ for a prismatic joint.

2.6 Discussion on the Static Force Formulations

2.6.1 On Static Force Problems Expressed in terms of Screw Coordinates

The static force problems are expressed in terms of screw coordinates, *ARS*s and wrench intensities. Reciprocal products and conservation of power are used to formulate the solution to the static force problem (Section 2.3). For the case of a planar manipulator, a force system acting on a rigid body requires two orthogonal coordinates to describe the force and one normal coordinate to describe the moment, i.e., $\mathbf{F} = \{f_x, f_y; m_z\}^T$. For a spatial manipulator, a force system would require three orthogonal coordinates to describe the force and three orthogonal coordinates to describe the moment acting on a rigid body, i.e., $\mathbf{F} = \{f_x , f_y, f_z; m_x, m_y, m_z\}^T$. A force system is referred to as wrench acting on a screw (Ball (1900), Hunt (1978)).

Similarly, for the case of a planar manipulator, an infinitesimal displacement of a rigid body or the general velocity of a rigid body requires one coordinate to describe an infinitesimal rotation (or angular velocity) and two orthogonal coordinates to describe an infinitesimal translation (or linear velocity), i.e., $\mathbf{V} = \{\omega_z; v_x, v_y\}^T$. For a spatial manipulator this would require three orthogonal coordinates to describe an infinitesimal rotation (or angular velocity) and three orthogonal coordinates to describe an infinitesimal translation (or linear velocity), i.e., $\mathbf{V} = \{\omega_x, \omega_y, \omega_z; v_x, v_y, v_z\}^T$. An infinitesimal motion (or velocity system) is referred to as a twist acting on a screw.

A semi-colon "; " is used to separate the coordinates used to describe the force and the moment of a *wrench* acting on a screw to emphasize the fact that they have different dimensions (*force* for a force and *length***force* for a moment). Using the standard metric system these dimensions have units of *N* for a force and *Nm* for a moment. The same comment can be made for a twist acting on a screw, where an angular velocity has dimensions of angle/time and a translational velocity has dimensions of length/time. Using the standard metric system these dimensions have units of *rads/s* for angular velocity and *m/s* for translational velocity.

2.6.2 On the Solution of Wrench Intensities and Corresponding Joint Torques (for *R* Joints) and Joint Forces (for *P* Joints)

The static force problem for symmetric non-redundantly actuated 3-branch planar *PM*s was formulated in this Chapter. Since the manipulators are non-redundantly actuated they must have three actuators. Since the actuation is symmetric the manipulators will have the same one joint actuated in each branch, this is referred to as 1-1-1 actuation. Alternatives to this would include having 2-1-0 actuation where one branch has two actuators, one branch has one actuator and the third has none. This actuation (and assumed joint displacement encoding) has advantages for the *FDS* simplifying calculations, but requiring actuation symmetry prevents 2-1-0 actuation. Having different joints actuated on each branch could have advantages for the design of particular planar *PM*s, but the requirements of such a planar *PM* have not been specified and again this would violate the requirement of having symmetric actuation.

Required wrench intensities are solved by inversion of the 3×3 matrix of *ARS*s. Note that other more efficient methods could be used (for example Gaussian Reduction or Householder Reflections (Strang (1988)) but as this is not a topic of this work, more efficient methods have not been further investigated. The numerically stable routines of *MATLAB* are used for this inversion. Also note that singularity of the *ARS* matrix means that the *PM* is unconstrained for certain forces, but this is the topic of previous research work, outlined in the review of literature of Chapter 1, and is not a topic of this Dissertation.

In the static force solution for *R* joints, the required wrench intensities are converted to joint torques using the mechanical advantage of the joints. Mechanical advantages are found using the reciprocal product of the screw coordinates of the actuated joint *j* in branch *i* and it's *ARS*, as in Equation (2-4). For *P* joints the actuated joint forces are found to be equal to the wrench intensity since the reciprocal product of the screw coordinates of the actuated *P* joint *j* in branch *i* and it's *ARS* is unity, i.e., equal to one.

2.6.3 On Reciprocal Product Invariance to Reference Frame Location and Orientation

Everything formulated in this chapter could have been done with vectors. However, the use of screw systems and screw coordinates is preferred since a reciprocal product of two screw quantities is invariant to changes in orientation and changes in the location of the

frame of reference. To demonstrate this invariance, note that the spatial transformation (Hunt 1978) of a screw ${}^{s}\$ = {}^{s}\{\$; \$_o\}^{T}$ known wrt $\{s\}$ to $\{f\}$ is given by:

$$ {}^{f}\$ = \left\{ {}^{f}_{s}\boldsymbol{R}\,{}^{s}\$;\;\; {}^{f}\check{\boldsymbol{r}}_{f-s}\,{}^{f}_{s}\boldsymbol{R}\,{}^{s}\$ + {}^{f}_{s}\boldsymbol{R}\,{}^{s}\$_0 \right\}^{T} = {}^{f}_{s}\boldsymbol{T}_{f-s}\,{}^{s}\$ \qquad (2\text{-}18) $$

where ${}^{f}_{s}\boldsymbol{R}$ is a 3x3 rotation matrix describing the orientation of $\{s\}$ wrt $\{ f \}$, the 3×3 matrix ${}^{f}\check{\boldsymbol{r}}_{f\text{-}s}$ is the cross-product skew-symmetric matrix of the 3x1 vector ${}^{f}\boldsymbol{r}_{f\text{-}s}$. The vector ${}^{f}\boldsymbol{r}_{f\text{-}s}$ defines the location of the origin of $\{s\}$ wrt the location of the origin of $\{ f \}$ known wrt the orientation of $\{ f \}$, and ${}^{f}_{s}\boldsymbol{T}_{f\text{-}s}$ denotes the 6x6 screw transformation matrix, i.e.,

$$ {}^{f}_{s}\boldsymbol{T}_{f-s} = \begin{bmatrix} {}^{f}_{s}\boldsymbol{R} & 0_{3\times3} \\ {}^{f}\check{\boldsymbol{r}}_{f-s}\,{}^{f}_{s}\boldsymbol{R} & {}^{f}_{s}\boldsymbol{R} \end{bmatrix}. \qquad (2\text{-}19) $$

The reciprocal product of two screw quantities $\$_1$ and $\$_2$ is the inner product:

$$ \$_1 \circledast \$_2 = \$_1 \cdot \$_{o2} + \$_{o1} \cdot \$_2 \qquad (2\text{-}20) $$

The reciprocal product of a "twist" and a "wrench" quantifies a rate of work. Two screws are reciprocal when their reciprocal product is zero. For example, a body having a motion described by a twist when subjected to a force system described by a wrench that is reciprocal to the twist performs no work.

The reciprocal product of two screw quantities is invariant under a transformation of frame of reference location and orientation. This invariance will now be demonstrated. The screw coordinates of two screws, ${}^{s}\$_i = {}^{s}\{\$_i; \$_{oi}\}^{T}$ and ${}^{s}\$_j = {}^{s}\{\$_j; \$_{oj}\}^{T}$ are known wrt a frame $\{s\}$ having an origin located at a point s. The reciprocal product of two screw quantities, ${}^{f}\$_i$ and ${}^{f}\$_j$, expressed in a frame $\{ f \}$ having an origin located at f using the transform given in Equation (2-18) is given by:

$$ {}^{f}\$ \circledast {}^{f}\$_{j} = {}^{f}_{s}\boldsymbol{R}\ {}^{s}\$_{i} \cdot ({}^{f}\check{\boldsymbol{r}}_{f\text{-}s}\ {}^{f}_{s}\boldsymbol{R}\ {}^{s}\$_{j} + {}^{f}_{s}\boldsymbol{R}\,{}^{s}\$_{oj}) + ({}^{f}\check{\boldsymbol{r}}_{f\text{-}s}\ {}^{f}_{s}\boldsymbol{R}\ {}^{s}\$_{i} + {}^{f}_{s}\boldsymbol{R}\,{}^{s}\$_{oi}) \cdot {}^{f}_{s}\boldsymbol{R}\ {}^{s}\$_{j}. \qquad (2\text{-}21) $$

Expressing the dot products in Equation (2-21) in terms of vector and matrix transposes gives:

$$ {}^{f}\$_{i} \circledast {}^{f}\$_{j} = {}^{s}\$^{T}_{oj}\ {}^{f}_{s}\boldsymbol{R}^{T}\ {}^{f}_{s}\boldsymbol{R}\mathbf{s}_{i} + {}^{s}\$^{T}_{j}\ {}^{f}_{s}\boldsymbol{R}^{T}\ {}^{f}\check{\boldsymbol{r}}^{T}_{f\text{-}s}\ {}^{f}_{s}\boldsymbol{R}\ {}^{s}\$_{j} + {}^{s}\$^{T}_{j}\ {}^{f}_{s}\boldsymbol{R}^{T}\ {}^{f}\check{\boldsymbol{r}}_{f\text{-}s}\ {}^{f}_{s}\boldsymbol{R}\ {}^{s}\$_{j} + {}^{s}\$^{T}_{oj}\ {}^{t}_{s}\boldsymbol{R}^{T}\ {}^{t}_{s}\boldsymbol{R}\ {}^{s}\$_{i}. \qquad (2\text{-}22) $$

Noting that ${}^{f}_{s}\boldsymbol{R}$ is an orthogonal rotation matrix and therefore ${}^{f}_{s}\boldsymbol{R}^{T} = {}^{f}_{s}\boldsymbol{R}^{-1}$, and that ${}^{f}\check{\boldsymbol{r}}^{T}_{f\text{-}s} = -\,{}^{f}\check{\boldsymbol{r}}_{f\text{-}s}$ Equation (2-22) simplifies to:

$$ {}^{f}\$_{i} \circledast {}^{f}\$_{j} = {}^{s}\$^{T}_{oj}\ {}^{s}\$_{i} + {}^{s}\$^{T}_{j}\ {}^{s}\$_{oi} = {}^{s}\$_{i} \cdot {}^{s}\$_{oj} + {}^{s}\$_{oi} \cdot {}^{s}\$_{j}, = {}^{s}\$_{i} \circledast {}^{s}\$_{j}. \qquad (2\text{-}23) $$

proving the invariance of the reciprocal product to a change in reference frame location and orientation.

2.6.4 On Reciprocal Screw Quantities

Section 2.3 outlines how to find *ARS*s, i.e., outlines the characteristics of reciprocal screw quantities. In summary, to be reciprocal to a zero-pitch screw (used to represent revolute joints), a reciprocal screw must be 0-pitch and intersect the zero-pitch screws or be parallel to the 0-pitch screw (intersect it at infinity). To be reciprocal to an infinite-pitch screw (used to represent prismatic joints) a screw must be perpendicular to the infinite-pitch screw. Using these rules, the *ARS*s which are reciprocal to all joints in the branch of a planar *PM* except for the associated actuated joint are identified.

2.6.5 On Static Force Problems for the 3-*RRR*, the 3-*RRR*, the 3- *RPR*, and the 3-*RPR PM*s

Section 2.5 formulates the static force problems for the 3-*RRR*, 3-*RRR*, 3-*RPR* and 3-*RPR* planar *PM*s, using the knowledge gained in Sections 2.2 and 2.3. These formulations will be used in Chapter 3 for circle, spiral, and arc trajectories. The non-redundantly actuated *PM*s will be seen to be prone to backlash. This being prone to backlash is due to the revolute actuated torques and the prismatic actuated forces being found to need actuator sign-switching which requires zero actuator-output values, values that are prone to backlash as outlined in Chapter 1.

Chapter 3

Static Force Solution Examples of Non-Redundantly Actuated *PM*s

3.1 Overview of Chapter 3

Cutting trajectories are considered in Section 3.2 for circle (Section 3.2.2), logarithmic spiral (Section 3.2.3) and arc (Section 3.2.4) trajectories. Trajectory feasibility for *PM* working areas and prismatic joint redesign for working area compatibility is presented in Section 3.3. Unconstrained configurations of the 3-*R*<u>*P*</u>*R PM* are considered in Section 3.4. The cutting force trajectories are considered in static force solutions for the 3-*RRR* and 3-*RPR PM*s (Section 3.5). That is, four non-redundantly actuated *PM*s: 3-<u>*R*</u>*RR* (Section 3.5.2), 3-*RR*<u>*R*</u> (Section 3.5.3), 3-<u>*R*</u>*PR* (Section 3.5.4), and 3-*R*<u>*P*</u>*R* (Section 3.5.5) are considered. A discussion in Section 3.6 summarizes the results and emphasizes that the points of zero actuated-joint-forces (torques for actuated <u>*R*</u> joints and forces for actuated <u>*P*</u> joints) are prone to the existence of backlash in *PM*s.

3.2 Considered Cutting Trajectories

3.2.1 Summary of Cutting Trajectories

Three examples are presented. In all examples, the manipulator is considered to be used in a cutting operation following a given trajectory. It is assumed that the motion is very slow along the trajectory so that dynamic effects are negligible and a kinetostatic analysis is justified. The trajectories were chosen such as to generate joint forces (torques or forces depending on the actuated-joint type) that switch directions when a non-redundant manipulator is used. A 100N force is considered to be acting on the manipulator in the direction opposite to its motion, i.e., tangent to its trajectory. No moment is considered to be applied to the platform, i.e., wrt the platform frame $\{p\}$, ${}^{p}m_z = 0$. However, from Equation (2-1) it can be seen that a moment will be applied wrt $\{B\}$ and the applied moment will not be zero. The calculations of the required actuated joint forces will be similar for any non-zero ${}^{p}m_z$. The orientation of the payload platform is constant at $\pi/6$ radians (30 degrees) ccw.

The three cutting trajectory examples include: the circle, logarithmic spiral and arc trajectories (Boudreau *et al*. (2012)). These before-mentioned trajectories are representative of actual cutting paths in applications. Further trajectories can be formed from combinations of the three trajectories presented below, or are simple to derive if they can't be formed by combinations of the three presented trajectories..

3.2.2 Circle Trajectory

The first trajectory considered is a circle centered at (0.1. 0.1)*m* with a radius of 0.05*m*. The wrench applied by the manipulator in frame {*B*} will be:

$$^{B}\mathbf{F} = \{f_x, f_y; m_z\}^T = \{-100\sin(\theta), 100\cos(\theta); -yf_x + xf_y\}^T N; Nm, \quad (3\text{-}1)$$

where θ is the angle between the horizontal line passing through the center of the path circle and the radius line to the point on the circle, and *x* and *y* are the coordinates of the point on the circle.

3.2.3 Logarithmic Spiral Trajectory

The second trajectory is a logarithmic spiral path described by the following polar equation:

$$\rho = \alpha e^{k\beta}, \quad \text{where } k = \cot(\varphi), \quad (3\text{-}2)$$

where ρ is the spiral radius for a given angle β, a is a constant (set here to be equal to *0.02m*) and φ is the angle between the tangent and the radial line at the polar point (ρ, β). Angle φ is chosen as 75 degrees, and the center is at (-0.1, 0.1)*m*. The wrench applied by the manipulator in this case is then:

$$^{B}\mathbf{F} = \{f_x, f_y; m_z\}^T = \{100\cos(\beta+\varphi), 100\sin(\beta+\varphi); -yf_x + xf_y\}^T N; Nm, \quad (3\text{-}3)$$

where β varies in this example from 0 to 2π radians, and *x* and *y* are the coordinates of a point on the spiral.

3.2.4 Arc Trajectory

The third trajectory is an arc of radius $r = 0.2m$, centered at the origin of $\{B\}$ and limited by the horizontal axis and an angle of 2 radians (114.6 degrees). This trajectory was chosen because it contains a position very close to a force uncertainty (singularity) when considering the *ARS*s of the 3-*RRR PM*. The *ARS*s of a 3-*RRR PM* are in the directions of the distal links of the branches, i.e., intersect the final two *R* joints of each branch. The "close to a force uncertainty" is due to all three of the *ARS*s lying in a plane and almost intersecting a common point (almost defining a planar pencil screw system of order two (Hunt 1978)). Figure 3.1 illustrates the corresponding "close to a force uncertainty" configuration.

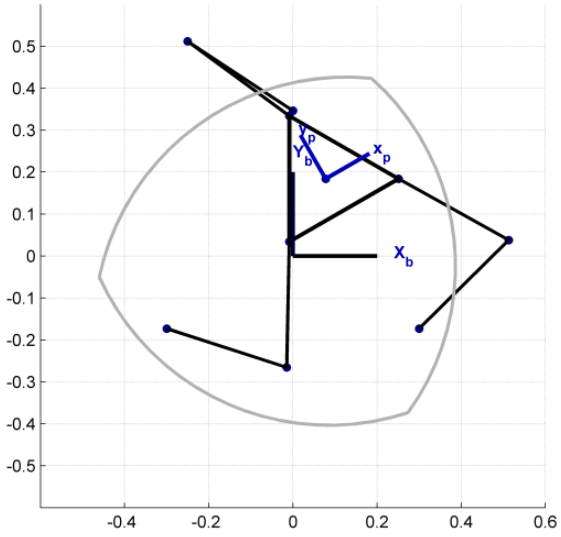

Figure 3.1: Uncertainty (singular) 3- *RRR PM* Position when Following arc Trajectory.

.

It can be observed from Figure 3.1 that the *ARS*s of the first actuated joint of the first branch (far-right branch) and the second branch (upper branch), which pass through the distal links, are almost aligned in a straight line. The third branch (far-left lower branch) *ARS* intersects the almost straight line almost defining a planar pencil of screw quantities, and thus the three base-actuated *ARS*s are close to meeting at a point. In this case, matrix $\$'_3$ is ill-conditioned and problems occur when trying to invert $\$'_3$. This causes difficulties when the algorithm tries to compute Equation (2-11) and similar equations involving inversions of $\$'_3$. Note that the same problem of ill-conditioned 3×3 *ARS* matrices can also occur if only the elbow joints are actuated. With non-redundant actuation it is not possible to avoid all uncertain (singular) configurations.

This problem of ill-conditioned $\$'_3$ is solved later when redundant actuation (both the base (shoulder) joints and elbow joints actuated) is considered. With redundant actuation the *ARS* matrix with the best, or at least an acceptable conditioning, is chosen for a wrench intensity particular solution. This choosing better conditioned $\$'_3$ will be left until later chapters on redundant actuation.

The wrench applied by the manipulator in frame $\{B\}$ for the arc trajectory has coordinates:

$$^{B}\mathbf{F} = \{f_x, f_y; m_z\}^T = \{-100\sin(\theta), 100\cos(\theta); -yf_x + xf_y\}^T N; Nm. \quad (3\text{-}4)$$

In Equation (3-4), θ is the angle between the horizontal line passing through the center of the arc path and the radius line to a point on the arc.

3.3 Trajectory Feasibility for *PM* Working areas and Prismatic Joint Redesign for Working area Compatibility

3.3.1 Feasibility of the Trajectories for the *PM* Working areas

All of the cutting trajectories, circle, spiral and arc, are illustrated on the constant orientation (having a payload platform angle φ = 30 degrees ccw) working area, found with the method of Section 1.4 and shown for the 3-*RRR PM* in Figure 3.2. Note that in Figure 3.2 the horizontal could be considered the *x*-direction and the vertical could be considered the *y*-direction, but the *PM*s can be mounted in any orientation about the normal to the plane of manipulation. For the 3-*RRR PM* all of the trajectories are feasible, i.e., lie within the 3-*RRR PM* working area (φ = 30 degrees ccw).

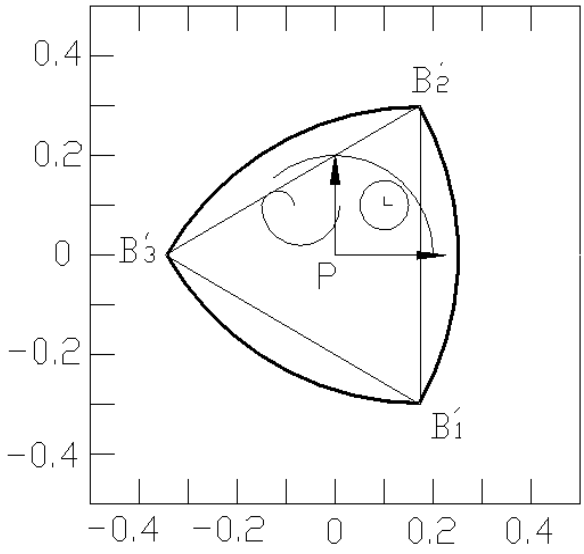

Figure 3.2: Working area (φ = 30 degrees ccw) and Trajectories for the 3-*RRR PM*.

Figure 3.3 illustrates the working area (φ = 30 degrees ccw) for the 3-*RPR PM*. All of the cutting trajectories: circle, spiral and arc are also illustrated on Figure 3.3. A mis-match exists for the working area of the 3-*RPR PM* and the trajectories, i.e., the trajectories are outside of the 3-*RPR PM*'s working area. The 3-*RPR PM* could be re-located to execute the circle trajectory but cannot be relocated to execute either of the spiral or arc trajectories. The constraint of minimum prismatic P_1, P_2 and P_3 lengths of 0.3*m* limits the working area as shown on Figure 3.3.

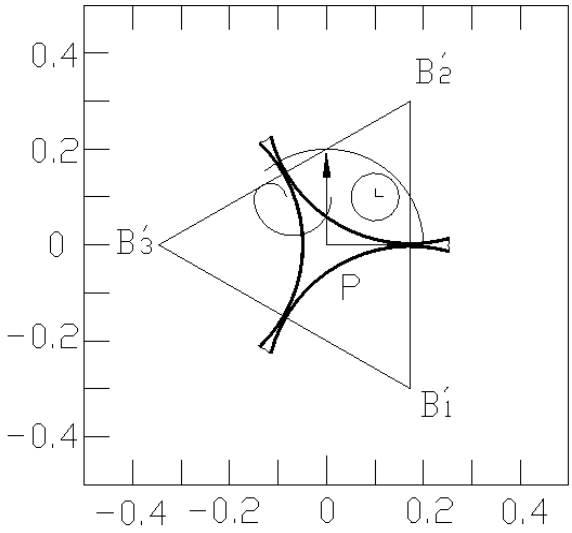

Figure 3.3: 3-*RPR PM* φ = 30 degrees ccw Working area and Trajectories.

3.3.2 3-*RPR PM* Prismatic Joint Modification to Accommodate Trajectories

To accommodate the trajectories the prismatic joints are modified to have length capabilities ranging from 0 to 0.6*m*. This modification involves prismatic joints varying

in length from 0.6*m* to 1.2*m*, as illustrated in Figure 3.4. A revolute joint which is perpendicular to the *PM* working area is located 0.6*m* from the end of the prismatic joint. The prismatic joint can expand to 1.2*m*. This maximum length relative to the revolute joint is 0.6*m*. If the prismatic joint is contracted to its minimum length, the length relative to the revolute joint is 0. With the relative ranges of the P_i, i = 1, 2, 3, being 0 to 0.6*m* the working area becomes equivalent to the working area shown in Figure 3.2, i.e., it is a working area containing all of the trajectories considered in this Chapter.

R_{1i} is connected to the base point B_{1i} and R_{3i} is connected to the payload platform point W_i, i = 1, 2 and 3. Note that a hydraulic cylinder is assumed to be used for the prismatic joint and 0.6*m* hangs in the back of the *PM* assembly for all three prismatic joints. Note that a similar overhang exists for prismatic joints based on lead screws, (see for example the 3-*RPR PM* of Williams II and Joshi (1999)). The overhangs have not been observed to cause any collision problems.

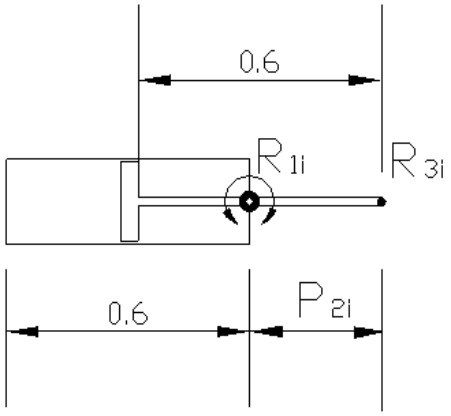

Figure 3.4: Prismatic Joint with 0 to 0.6*m* Capability, R_{1i} and R_{3i} Locations, and P_{2i} Displacement.

3.4 Unconstrained Configurations of the 3-*RPR PM*

3.4.1 3-*RPR PM* Usual Non-Redundant Actuation and Prismatic Joint *ARS*s

The non-redundantly actuated 3-*RPR PM* generally has the *P* joints of each branch actuated (e.g.,: Gosselin and Angeles (1990), Williams II and Joshi (1999) and Yang and O`Brien (2007)). Within Section 3.2.4, a close to unconstrained (also known as a force uncertainty) configuration is described for the 3-*RRR PM* executing an arc trajectory. In an unconstrained configuration the constraint forces provided by the actuators do not constrain the potential motions and forces to be applied by the *PM*. Since the *PM*s considered in this Dissertation are planar manipulators, the forces of constraint must constrain forces within the plane of manipulation (e.g., X and Y forces). Moments perpendicular to the plane of motion (moments in the Z direction) must also be constrained. Constraining the above 3-system of planar motions and forces requires a 3-system of planar forces (Hunt (1978)).

3-RPR PM unconstrained (force uncertainty) configurations: the lines B_iP_i, i = 1, 2 and 3, define the directions of B_iP_i and the application points P_i, i = 1, 2 and 3 of the forces applied by the prismatic joints to the payload platform. These forces are the *ARS*s of the branches of the 3-*RPR PM*. Usually these three forces constrain the payload platform for forces in the X and Y directions (the plane of the planar 3-*RPR PM*) and for moments perpendicular (in the normal (Z) to the plane), i.e., the forces generally form a 3-system (Hunt (1978)) of constraints and can be represented with three zero-pitch screw

quantities (wrenches) $\mathbf{F}_i$, i = 1, 2 and 3. The wrenches $\mathbf{F}_i$ are collinear with the lines defined by B_iP_i , i = 1, 2 and 3 for the 3-*RPR PM*, i.e., $\mathbf{F}_i$ intersects the first and the third joints of branch i. While normally forming a 3-system constraining all possible motions and applied forces, unconstrained (singular) configurations exist for the 3-*RPR PM*.

Merlet (1989) considered the uncertainty configurations related to the spatial *6-UPS PM*. Merlet noted that the constraint forces provided by each *P* joint lies on a line passing through the centers of the passive *U* and *S* joints of its branch. Using Grassman line geometry, Merlet (1989) determined uncertainty configurations for the *6-UPS PM*.

O'Brien *et al*. (2006) and O'Brien and Wen (2006) determined unstable singular configurations where the 3-*RPR PM*s lose the ability to counteract forces in uncertain directions and can experience finite unconstrained motion. Li *et al*. (2006) determined the maximal singularity-free zones within the working areas of planar *PM*s.

3.4.2 Analytical Input and Output Velocity Equations

Gosselin and Angeles (1990) identified three types of singularities for closed-loop kinematic chains by differentiating the non-linear loop–closure equations wrt time. The non-linear loop-closure equations of Gosselin and Angeles (1990) are in terms of the input (joint displacements **q**) and output (end-effector pose ***x***) variables, i.e.,:

$$f(\mathbf{q}, \boldsymbol{x}) = 0 \quad . \tag{3-5}$$

Differentiating Equation (3-5) wrt time yields:

$$\mathbf{A}\left(\frac{\partial \boldsymbol{x}}{\partial \mathrm{t}}\right) = \mathbf{B}(\partial \mathbf{q}/\,\partial \mathrm{t}), \tag{3-6}$$

where $\mathbf{A} = \partial f(\mathbf{q}, \boldsymbol{x})/\,\partial \mathbf{x}$ and $\mathbf{B} = \partial f(\mathbf{q}, \boldsymbol{x})/\,\partial \mathbf{q}$ are $m \times m$ Jacobian matrices where m is the *DOF* of the linkage (3 in this case) and $\partial \mathbf{x}/\partial \mathrm{t}$ and $\partial \mathbf{q}/\partial \mathrm{t}$ are the end-effector and joint velocities, respectively.

Considering Equation (3-6), the inverse velocity solution is equal to:

$$\frac{\partial \mathbf{q}}{\partial \mathrm{t}} = \mathbf{B}^{-1}\mathbf{A}\left(\frac{\partial \mathbf{x}}{\partial \mathrm{t}}\right) = \mathbf{J}^{-1}\left(\frac{\partial \mathbf{x}}{\partial \mathrm{t}}\right), \tag{3-7}$$

where $\mathbf{J}^{-1} = \mathbf{B}^{-1}\mathbf{A}$. Following the singularity derivation of Firmani and Podhorodeski (2009), for static conditions the relationship between the joint forces $\boldsymbol{\tau}$ and the applied force $\mathbf{F}$ is:

$$\mathbf{F} = \mathbf{J}^{-\mathrm{T}}\boldsymbol{\tau}. \tag{3-8}$$

Therefore, the joint forces are given by:

$$\boldsymbol{\tau} = \mathbf{J}^{\mathrm{T}}\mathbf{F} = (\mathbf{A}^{-1}\mathbf{B})^{\mathrm{T}}\mathbf{F}. \tag{3-9}$$

The three types of uncertainties identified by Gosselin and Angeles (1990) correspond to: Type I (velocity singularity) when **B** is singular as shown in Equation (3-7); Type II (force singularity) when **A** is singular as shown in Equation (3-9), platform can have motion even when the joints are locked; and Type III (complex singularity) occurs when both **A** and **B** are simultaneously singular. Type II uncertainties are the topic of this sub-section.

Equation (3-9) allows the finding of force uncertain configurations by root finding of polynomial expressions that result from tangent half-angle (Strang (1988)) substitution. This technique is utilized by Gosselin and Angeles (1990), Gosselin *et al*. (1992), Mohammadi-Daniali *et al*. (1995), Bonev *et al*. (2003), and Firmani and Podhorodeski (2009). Major differences in the previously-mentioned five papers include frames of reference and *PM* actuation inversions used to minimize the order of the resulting polynomials. Collins and McCarthy (1998) derive quartic singularity surfaces for planar parallel manipulators. The derivation of Collins and McCarthy (1998) is done for general payload platform orientations rather than a specific angle as in Gosselin *et al*. (1992). Hayes and Husty (2003) develop kinematic constraint surfaces for three-legged planar *PM*s. The parameterizations used by Hayes and Husty that describe the constraint surfaces have the advantage of being singularity free.

For 3-*RPR PM* uncertainties, the resulting singularity polynomial is quadratic (Firmani and Podhorodeski (2009)). In the remainder of this sub-section, a geometric (screw coordinate) derivation of uncertainty configurations of the 3-*RPR PM*, due to payload and base platform edge alignment, is presented.

3.4.3 Uncertainty Configurations due to Platform and Base Edge Alignments

For the description of the force uncertainty configurations, first a simple example will be used. Consider the P_3P_1 edge of the payload platform to be located and oriented such that

it lies on the line defined by B_3 and B_1 as shown in Figure 3.5. If P_3P_1 is collinear with B_3B_1, the actuation force $\mathbf{F}_1$ provided by the prismatic joint connecting B_1P_1 becomes collinear with the actuation force $\mathbf{F}_3$ provided by the prismatic joint connecting B_3P_3. The actuation force $\mathbf{F}_2$ provided by the prismatic joint B_2P_2 is perpendicular to the force provided by B_3P_3 and B_1P_1. All three of the actuation forces intersect at a concurrency point, C. The *PM* is instantaneously unconstrained for rotations about the point C and cannot apply or sustain a moment, perpendicular to the plane of motion, about point C. In this case, the forces provided by the actuators, B_1P_1, B_2P_2 and B_3P_3 form a 2-system of screw quantities (a planar pencil with a concurrency point C, (Hunt (1978)) and do not instantaneously constrain the manipulation system.

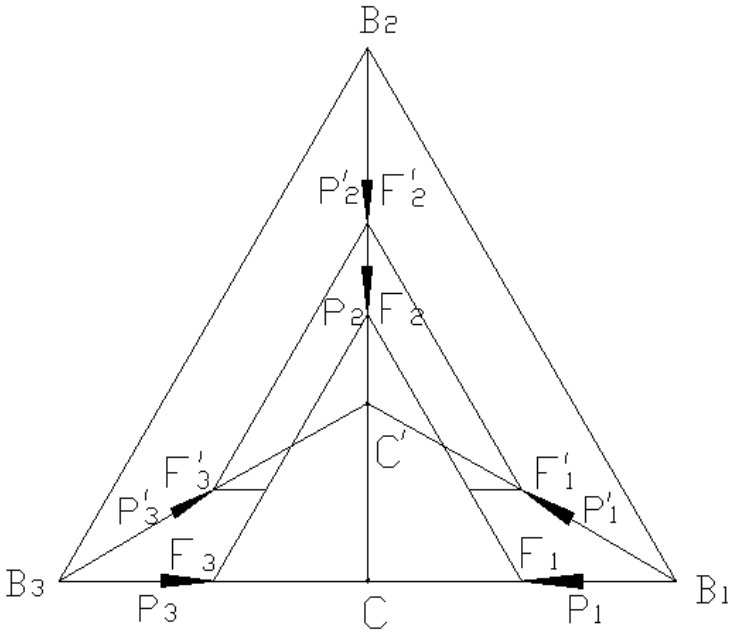

Figure 3.5: Concurrency Points leading to Uncertainty Configurations of the 3-*RPR PM*.

Still referring to Figure 3.5 if an arbitrary displacement (with no rotation) of P_3P_1 is considered perpendicular to the edge B_3B_1 the location $P_3'P_1'$ is achieved (note that the entire payload platform was displaced). Lines (*0*-pitch wrenches $\mathbf{F}_3'$ and $\mathbf{F}_1'$) through B_3P_3' and B_1P_1' intersect at a point proposed to be a concurrency point, C', for the three wrenches $\mathbf{F}_1'$, $\mathbf{F}_2'$ and $\mathbf{F}_3'$. Since the line (*0*-pitch wrench $\mathbf{F}_2'$) through B_2P_2' passes through the point C', the point C' is confirmed to be a degenerate concurrency point of the three wrenches. Again, it should be noted that the *PM* is instantaneously unconstrained for rotations about the point C' and cannot apply or sustain a moment, perpendicular to the plane of motion, about the point C'. Since the displacement of P_3P_1 is arbitrary the above construction demonstrates concurrency of $\mathbf{F}_1$, $\mathbf{F}_2$ and $\mathbf{F}_3$ can be shown an order of a single infinity ($O(\infty^1)$ (Erdman and Sandor (1996)) number of times. Note that an $O(\infty^1)$ is the number of points on a line. The concurrency points will lie on the line passing through C and C'.

The above proof of the existence of an $O(\infty^1)$ of concurrency points of constraint wrenches for the 3-*RPR PM* leading to instantaneously unconstrained configurations can be repeated an $O(\infty^1)$ times for platform edges P_1P_2 and P_2P_3 located centrally and aligned respectively with B_1B_2 and B_2B_3. In total, there are $3*O(\infty^1) = O(\infty^1)$ instantaneously unconstrained configurations. Note that these uncertainties are due to alignment of platform and base edges. Firmani and Podhorodeski (2009) demonstrated that 2-dimensional manifolds (an $O(\infty^2)$) of uncertainty poses exist within all x-y-φ coordinates for 3-*RPR PM*s. Note that an $O(\infty^2)$ is the number of points on a plane.

3.4.4 Stability of Payload Platform considering Rotation

To illustrate that the 3-*RPR PM* has a stable payload platform, assume that the platform edge P_3P_1 is centrally located to, B_3B_1, snd has the alignment of B_3B_1. Also assume that P_3P_1 is displaced perpendicularly to B_3B_1 such that the centre of P_3P_1 is coincident with the *PM*'s reference frame origin. This configuration was shown in Section 3.4.3 to be an instantaneous uncertainty.

Now consider a rotation of the payload platform by 30 degrees ccw. This results in rotated platform edge locations of P_3' and P_1' as shown on Figure 3.6. Intersecting lines (*0*-pitch wrenches $\mathbf{F}_3$' and $\mathbf{F}_1$') through B_3P_3' and B_1P_1' yields the concurrency point C_{31} for $\mathbf{F}_3$' and $\mathbf{F}_1$'. Intersecting $\mathbf{F}_1$' and $\mathbf{F}_2$', through B_1P_1' and B_2P_2', yields a concurrency point C_{12} for $\mathbf{F}_1$' and $\mathbf{F}_2$'. Intersecting $\mathbf{F}_2$' and $\mathbf{F}_3$', through B_2P_2' and B_3P_3', yields a concurrency point C_{23} for $\mathbf{F}_2$' and $\mathbf{F}_3$'. Noting that C_{31}, C_{12}, and C_{23} are not the same point demonstrates that the constraint forces $\mathbf{F}_1$', $\mathbf{F}_2$' and $\mathbf{F}_3$' do not define an uncertainty configuration, i.e., they form a *3*-system capable of constraining arbitrary planar forces and motions. O'Brien *et al*. (2006) determined examples of finite unstable singularities in parallel robots with N-arms. The uncertainty due to platform and base edge alignments for the planar 3-*RPR PM* is not a case of *a* finite unstable singularity, i.e., it is stable.

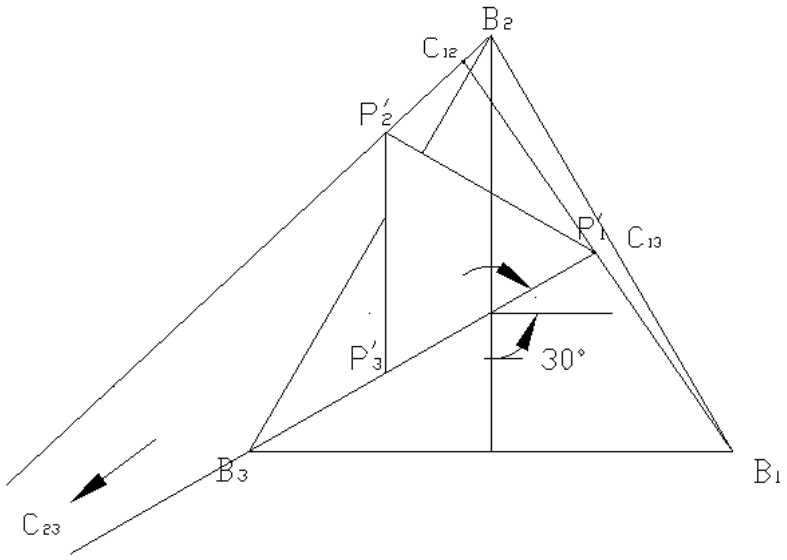

Figure 3.6: Demonstrating Stability of the 3-*RPR PM* using a Rotation of P_3P_1.

.

It could be stated that the above argument of $\mathbf{F}_1$', $\mathbf{F}_2$' and $\mathbf{F}_3$' not forming an unstable uncertainty configuration is only good for a rotation of 30 degree ccw of the payload platform. However, it can be demonstrated that this observation is true for arbitrary (ccw or cw) rotations of the payload platform, i.e., the payload platform is stable. The uncertainty is dependent on the edges being parallel. It could also be argued that the rotation also only demonstrates stability for a reference specific frame origin location. However, the same demonstration of stability through rotation can be applied to the other frame origin locations. Note that the existence of uncertain configurations causes the inversion of the 3×3 matrix of *ARS*s, $\$'_3$, to be ill-conditioned in the uncertain configurations. In later Chapters, it is demonstrated that the addition of redundant actuation allows the selection of utilized *ARS*s to ensure a well-conditioned $\$'_3$.

3.5 Example Static Force Solutions

3.5.1 Summary of Considered *PM*s and Force Trajectories

Manipulators based on the 3-*RRR* and 3-*RPR PM* layouts and the cutting force trajectories of Section 3.2 are considered for the example static force solutions. That is, four non-redundantly actuated *PM*s: 3-*RRR*, 3-*RRR*, 3-*RPR* and 3-*RPR*; and three trajectories: circle, logarithmic spiral and arc trajectories; are considered. The *PM*s all have length dimensions of 0.3*m* for each side of the payload platform and 0.6*m* for the sides of the base platform. The arms of the 3-*RRR PM*s are 0.3*m* in length and the 3-*RPR PM*s have *P* joints that with the redesign of Section 3.3.2 can vary in length between 0 and 0.6*m*.

Figure 3.2 shows a constant orientation working area (φ = 30 degrees) obtained using the geometric method of sub-Section 1.4 for a 3-*RRR PM* of the above dimensions. Note that with the prismatic joint redesign of Section 3.3.2 the working area of the 3-*RPR PM* is also the area shown in Figure 3.2. Also shown on Figure 3.2 are the circle, spiral and arc trajectories.

3.5.2 3-*RRR PM*

Using Equation (3-1), the required joint torques for the 3-*RRR PM* executing the circle trajectory are shown in Figure 3.7.

Using Equation (3-3), the required joint torques for the 3-*RRR PM* executing the spiral trajectory are shown in Figure 3.8.

Using Equation (3-4), the required joint torques for the 3-*RRR PM* executing the arc trajectory are shown in Figure 3.9.

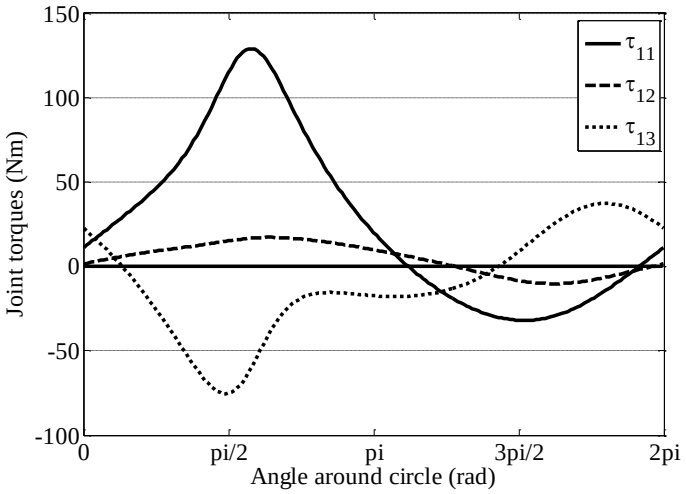

Figure 3.7: 3-*RRR PM* Joint Torques to Follow Circle Trajectory.

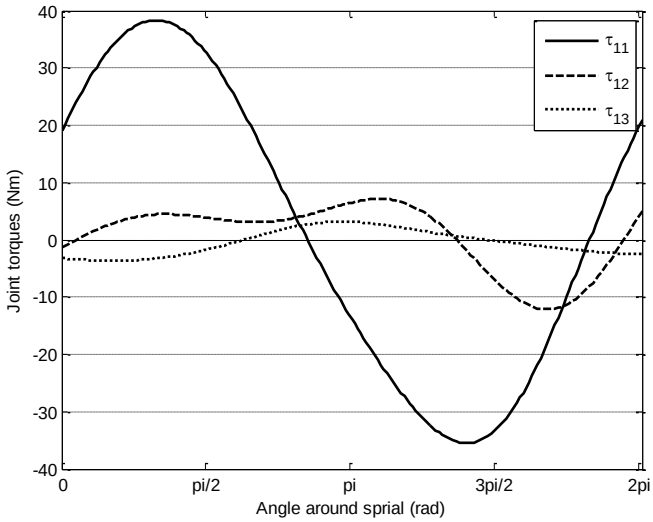

Figure 3.8: 3- *RRR PM* Joint Torques to Follow Spiral Trajectory.

.

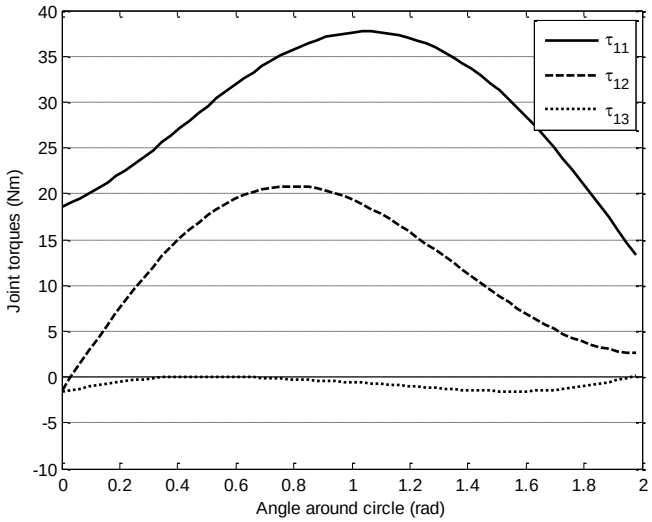

Figure 3.9: 3-*RRR PM* Joint Torques to Follow Arc Trajectory.

3.5.3 3-*RRR PM*

Using Equation (3-1), the required joint torques for the 3-*RRR PM* executing the circle trajectory are shown in Figure 3.10.

Using Equation (3-3), the required joint torques for the 3-RRR *PM* executing the spiral trajectory are shown in Figure 3.11.

Using Equation (3-4), the required joint torques for the 3-*RRR PM* executing the arc trajectory are shown in Figure 3.12.

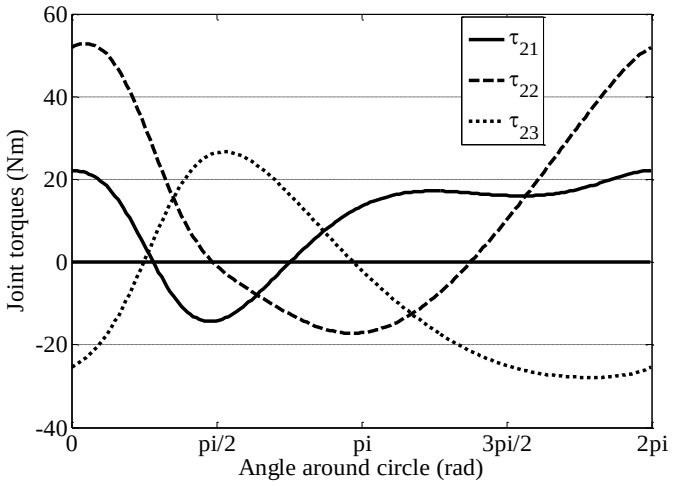

Figure 3.10: 3-*RRR PM* Joint Torques to Follow Circle Trajectory.

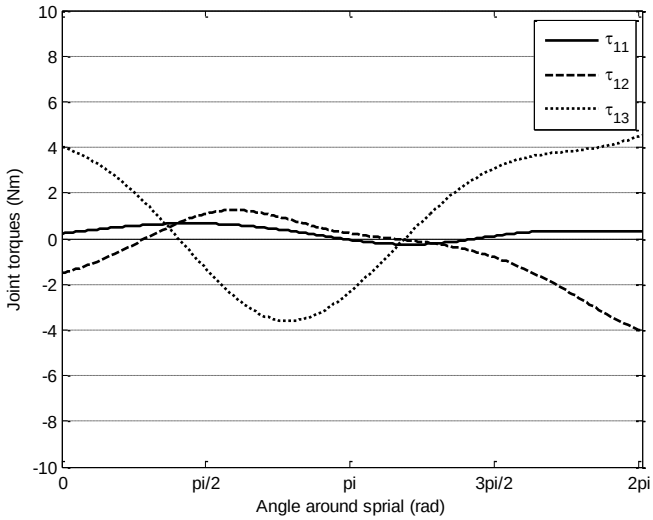

Figure 3.11: 3-*RRR PM* Joint Torques to Follow Spiral Trajectory.

.

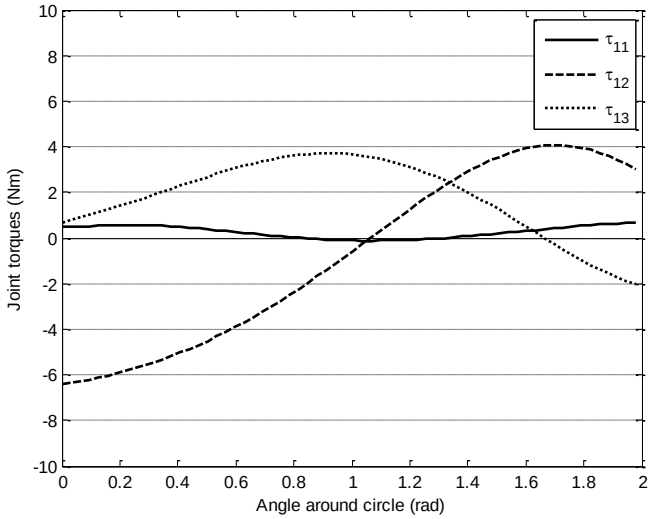

Figure 3.12: 3-*RRR PM* joint torques to Follow Arc Trajectory.

3.5.4 3-*RPR PM*

Using Equation (3-1), the required joint torques for the 3-*RPR PM* executing the circle trajectory are shown in Figure 3.13.

Using Equation (3-3), the required joint torques for the 3-*RPR PM* executing the spiral trajectory are shown in Figure 3.14.

Using Equation (3-4), the required joint torques for the 3-*RPR PM* executing the arc trajectory are shown in Figure 3.15.

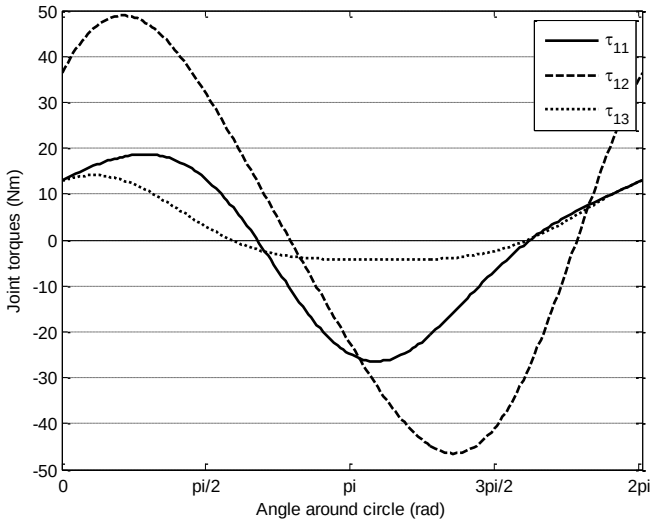

Figure 3.13: 3-*RPR PM* Joint Torques to Follow Circle Trajectory.

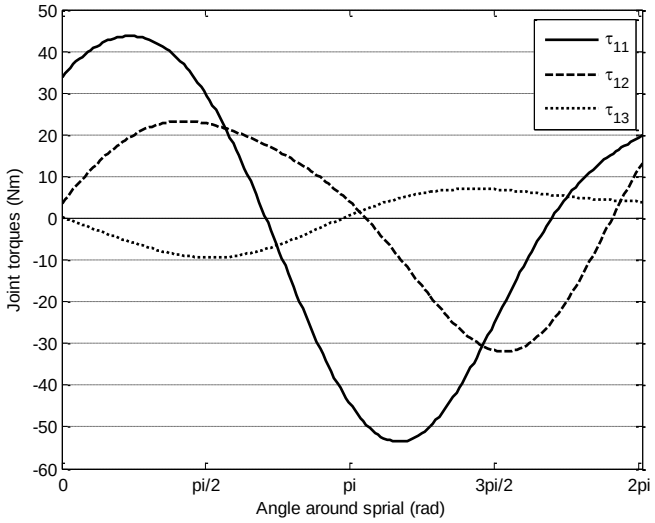

Figure 3.14: 3-*RPR PM* Joint Torques to Follow Spiral Trajectory.

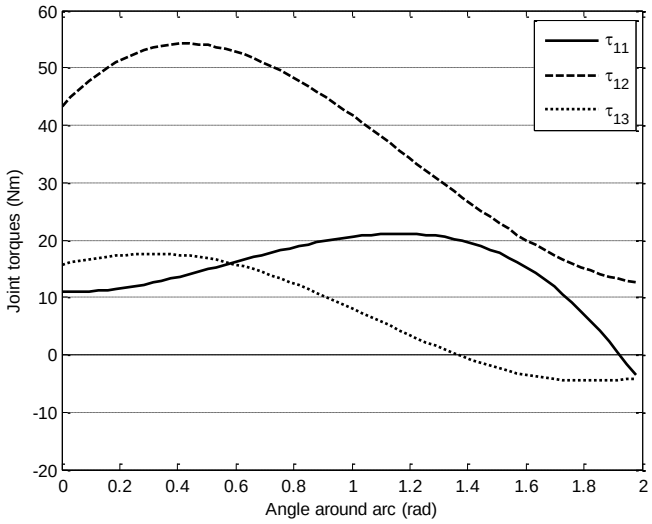

Figure 3.15: 3-*RPR PM* Joint Torques to Follow Arc Trajectory.

3.5.5 3-*RPR PM*

Using Equation (3-1), the required joint forces for the 3-*RPR PM* executing the circle trajectory are shown in Figure 3.16.

Using Equation (3-3), the required joint forces for the 3-*RPR PM* executing the spiral trajectory are shown in Figure 3.17.

Using Equation (3-4), the required joint forces for the 3-*RPR PM* executing the arc trajectory are shown in Figure 3.18.

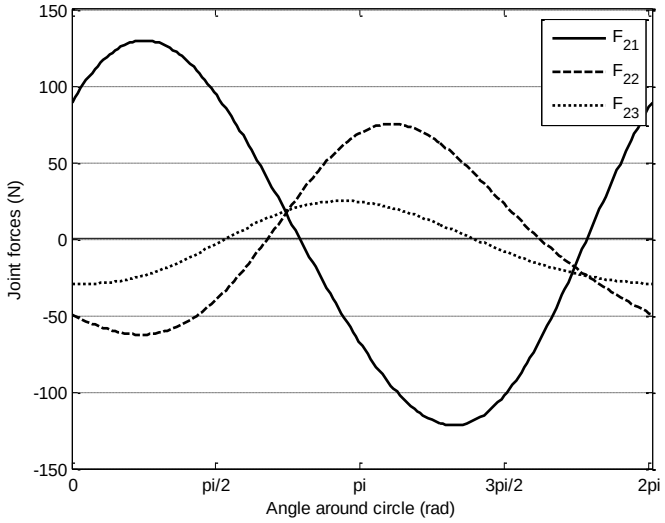

Figure 3.16: 3-*RPR PM* Joint Forces to Follow Circle Trajectory.

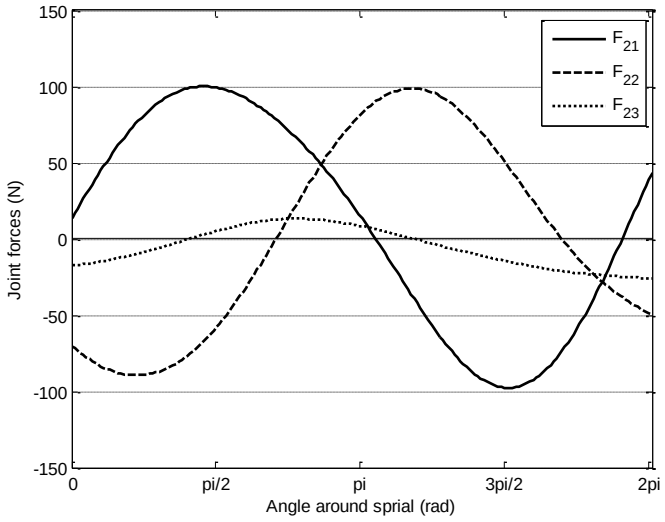

Figure 3.17: 3-*RPR PM* Joint Forces to Follow Spiral Trajectory.

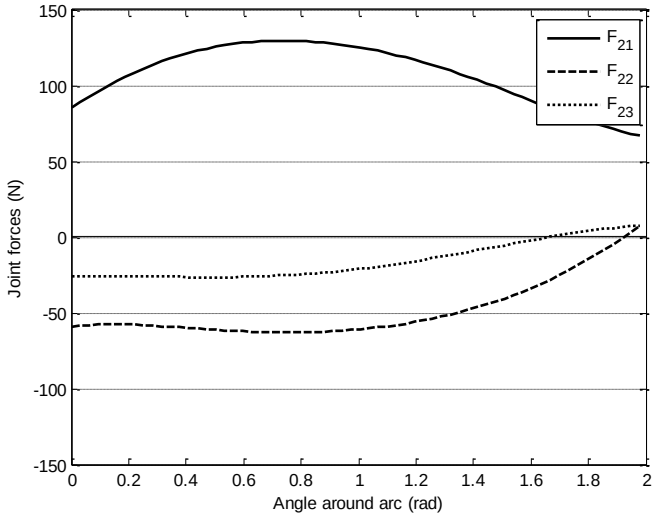

Figure 3.18: 3-*RPR PM* Joint Forces to Follow Arc Trajectory.

3.6 Discussion

3.6.1 On the Considered Cutting Trajectories

The force trajectories of Section 3.2.2 (circle), 3.2.3 (spiral) and 3.2.4 (arc) have characteristics found in realistic cutting trajectories for robotic devices. For later discussion it is important to note that the circle and the spiral trajectories consider a full rotation (θ = 0 to 2π). The arc trajectory has a larger radius than the circle trajectory, but is only presented for θ = 0 to 2 radians. In simulations presented later in this discussion the arc trajectory is tested for full-circle rotation, i.e., θ = 0 to 2π.

3.6.2 On Trajectories not Matched to Their Working areas

The 3-*RRR* and 3-*RPR PM*s are applied to tasks of circle, spiral and arc cutting trajectories. The cutting trajectories are well matched to the 3-*RRR PM* with all trajectories lying within the working area of the *PM*. However, for the 3-*RPR PM* working area, with its constraint on the minimum *P* joint length, none of the cutting trajectories match its working area, with the exception of the circle trajectory. However, due to the working area and trajectory mismatches, redesign of the *P* joint was necessary.

3.6.3 On Modification of the Prismatic Joint for the 3-RPR *PM*

The *P* joint of the 3-*RPR PM* was modified to allow length changes from 0 to 0.6*m*. The redesign involved a *P* joint with a fully extended length of 1.2*m* and a collapsed length of 0.6*m*. Relative to a 0 measurement point located at a *R* joint positioned 0.6*m* from the *P* joints end, this allows relative *P* joint lengths of 0 to 0.6*m*. The modification, however, results in an overhang of 0.6*m* for each of the three *P* joints of the 3-*RPR PM*. A similar overhang occurs for *P* joints based on lead screws. With a collapsible pneumatic joint controlled to have lengths between 0 and 0.6*m*, the 0.6*m* overhang can be avoided.

3.6.4 On Unconstrained Configurations of the 3-*RRR* and 3-*RPR PM*

In Section 3.2.4, a close to uncertainty (singular) configuration is demonstrated for the 3-*RRR PM* executing an arc trajectory. This uncertainty configuration was due to the alignment of the joints and can occur for any trajectory. In Section 3.4, uncertainty

configurations are examined for the 3-*RPR PM*. Non-rotated platform edges centrally located wrt their corresponding base edges were shown to be in uncertainty configurations wrt a concurrency point of the applied constraint wrenches. The payload platform was not constrained for rotations and cannot apply moments about the constraint wrench concurrency point. Since uncertainties exist for platforms displaced an arbitrary distance perpendicularly to the corresponding base edge, it is concluded that an $O(\infty^1)$ of uncertainty configurations exist for the 3-*RPR PM* due to platform and base edge alignments.

If the base and platform edges do not align an intersection, for example, of branch one's force $\mathbf{F}_1$ and branch two's force $\mathbf{F}_2$ still intersect at a concurrency point C_{12}. A platform angle that corresponds to the branch three's force $\mathbf{F}_3$ intersecting C_{12} is a platform angle φ corresponding to an uncertainty configuration and demonstrates that an $O(\infty^2)$ uncertainty configurations exist. The same argument can be made for $\mathbf{F}_2$ and $\mathbf{F}_3$ having a concurrency point C_{23} and a platform angle φ existing such that $\mathbf{F}_1$ intersects C_{23} demonstrating another $O(\infty^2)$ of uncertainty configurations can exist. An identical argument exists for $\mathbf{F}_3$ and $\mathbf{F}_1$ having a concurrency point C_{31} and a platform angle φ existing such that $\mathbf{F}_2$ intersects C_{31} leading to another $O(\infty^2)$ of uncertainty configurations. Noting $3 * O(\infty^2) = O(\infty^2)$ it can be stated that an $O(\infty^2)$ of uncertainty configurations exist for the 3-*RPR PM* demonstrated by arguments of kinematic geometry (Hunt 1978). Firmani and Podhorodeski (2009) derived the uncertainty configurations of the 3-*RPR PM* by solving platform angles φ yielding x values, and after back substitution y values, causing the matrix **A** of Equation (3-9) to be singular. Since a quadratic function of x

values is found, it is possible to demonstrate that an $O(\infty^2)$ of uncertainty configurations exist.

The home position of the 3-*R*<u>*P*</u>*R PM* corresponds to an uncertainty configuration. It is disturbing to consider that the 3-*R*<u>*P*</u>*R PM* is not constrained for moments and instantaneous rotations about a concurrency point in its home position. However, this disturbing fact is minimized since it is shown in Section 3.4.4 that after rotation of the payload platform, the 3 concurrency points associated with the 3 pairs of constraint wrenches are not concurrent, i.e., the constraint wrenches form a planar 3-system of forces. The addition of a passive spring system applying a moment to the 3-*R*<u>*P*</u>*R PM* could also be used to reduce the uncertainty.

Within Future Work (Section 6.4), it is proposed that the uncertainties found in Firmani and Podhorodeski (2009) should be verified for the uncertainties found in this Dissertation for 3-*R*<u>*P*</u>*R PMs* using kinematic geometry.

3.6.5 On the Example Static Force Solutions

The inverse force problem results for the non-redundant cases of the shoulder joints (branch first joints) actuated and for the branch second joints (either elbow or prismatic) actuated for the 3-*RRR* and 3-*RPR PM*s is very realistic for *PM*s. That is, the results in Section 3.5.2 (3-<u>*R*</u>*RR*), Section 3.5.3 (3-*R*<u>*R*</u>*R),* Section 3.5.4 (3-<u>*R*</u>*PR*) and Section 3.5.5 (3-*R*<u>*P*</u>*R*) are realistic to the field of *PM*s. It is very important to notice that all of the non-redundant joint force diagrams in Section 3.5 encountered zero joint forces (torques for

actuated *R* joints or forces for actuated *P* joints). Zero joint forces are prone to backlash problems as introduced in Chapter 1.

With the circle trajectory, the applied force from the cutting trajectory eventually revolves in all directions. This causes the required actuated torques or forces to encounter zero values in two distinct locations. These two distinct locations can be seen in the torque or force plots for the circle trajectory for each joint in: Figures 3.7 for the 3-*RRR PM*; Figure 3.10 for the 3-*RRR PM*; Figure 3.13 for the 3-*RPR PM* and Figure 3.16 for the 3-*RPR PM*.

With the logarithmic spiral trajectory, again the applied force associated with the cutting trajectory eventually points in all directions. Again this causes the required actuated torques or forces to encounter zero values in two distinct locations. These two distinct locations can be seen in the torque or force plots for each joint in: Figures 3.8 for the 3-*RRR PM*; Figure 3.11 for the 3-*RRR PM*; Figure 3.14 for the 3-*RPR PM* and Figure 3.17 for the 3-*RPR PM*.

With the arc trajectory since the applied force directions only varied from $\theta = 0$ to 2 radians, the applied force associated with the cutting trajectory only point in directions which vary between 0 to 2 radians. In this case, the required actuated torques or forces only encounter a zero value in one distinct location. The existence of one distinct zero value is evident in the torque or force plots for each joint in: Figures 3.9 for the 3-*RRR PM*; Figure 3.12 for the 3-*RRR PM*; Figure 3.15 for the 3-*RPR PM* and Figure 3.18 for the 3-*RPR PM*. The arc trajectory can be considered to be a circle trajectory of a large radius.

When the force calculations are run for the arc trajectory considering applied force directions varying between θ = 0 to 2π, the applied force associated with the cutting trajectory eventually points in all directions. Again this causes the required actuated torques or forces to encounter zero values in two distinct locations, i.e., backlash-prone locations. Figure 3.19 and 3.20 illustrate the required torque and force plots for the 3-*RPR PM* executing a full-circle arc trajectory ($\theta = 0$ to 2π) with the base-revolute joint actuated, and with the elbow-prismatic joint actuated, respectively.

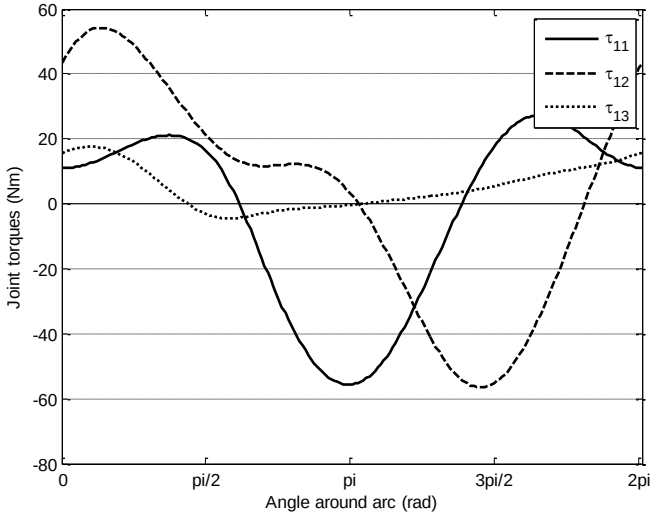

Figure 3.19: 3-*RPR PM* Joint Torques for the Full-circle Arc Trajectory ($\theta = 0$ to 2π).

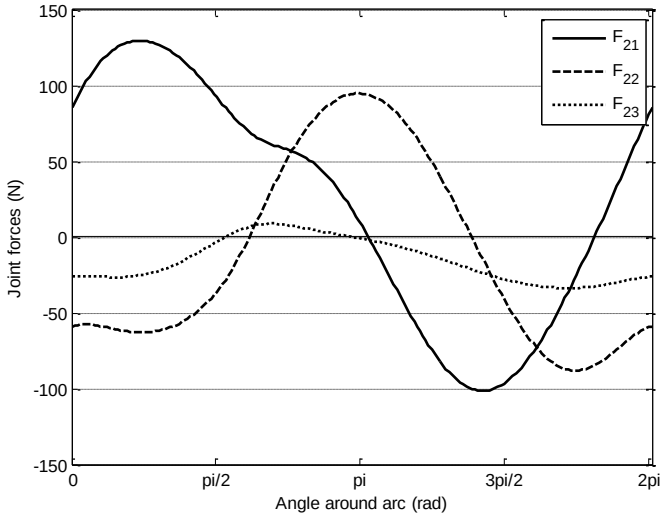

Figure 3.20: 3-*RPR PM* Joint Forces for the Full-circle Arc Trajectory ($\theta = 0$ to 2π).

Chapter 4 of this Dissertation considers the use of actuation redundancy to reduce backlash-prone configurations in *PM*s.

Chapter 4

Backlash Reduction using Actuation Redundancy

4.1 Overview of Chapter 4

The reduction of backlash through the use of actuation redundancy is considered in Chapter 4. It was found in Chapter 3 that non-redundant actuation of a *PM* does not ensure backlash-free motion. With non-redundant actuation it was found that sign switching was required in the actuators. This sign switching requires backlash-prone zero-actuated joint-forces (torques for *R* joints, applied forces for actuated *P* joints). As noted earlier (Chapter 1), this actuator sign-switching results in the creation of backlash due to clearances in drive-chain components. In the non-redundant actuation of Chapter 3, either the 1st (shoulder *R*) joint or the 2nd (elbow *R* for 3-*RRR* or *P* for 3-*RPR PM*s) joint of each branch was considered to be actuated. In this Chapter, both the first and the

second joints of each branch are considered to be actuated simultaneously, i.e., 3-*RRR* or 3-*RPR* actuation.

Symmetry of the redundantly actuated *PM* is achieved with 3-*RRR* or 3-*RPR PM* actuation. Force capabilities with the 3-*RRR* or 3-*RPR PM* will be symmetric and the actuation *DOR* being equal to three, i.e., *DOR* = 3 provides back up in case of actuation failure. As an example, consider a case of a 3-*RPR PM* with one branch *RPR* redundantly actuated and two branches *RPR*, non-redundantly actuated, for in total four actuated joints in the *PM*. Normally this *PM* is constrained and capable of sustaining and applying a 3-system of forces. Say that one of the *RPR* has an actuator failure and becomes incapable of sustaining or providing a force. The *ARS* of the second *RPR* branch is a line in the plane of manipulation of the *PM*. If this second *RPR* branch's *ARS* intersects the intersection point of the two *ARSs* of the *RPR* actuated branch (the passive wrist *R* joint of the *RPR* branch) the *PM* is instantaneously incapable of sustaining or applying a moment about the passive *R* joint of the *RPR* branch.

The static force problems to be solved for *PM*s with actuation redundancy are outlined in Section 4.2. Resolving actuation output-forces is first attempted using pseudo-inverse (right Moore-Penrose (Strang 1978)) solutions (Section 4.3). The forces to be applied are modeled as quasi-static problems associated with the circle, spiral and arc cutting (force and displacement) trajectories introduced in Sections 3.2, 3.3 and 3.4. The pseudo-inverse solutions are found to still require actuator output forces that switch signs. Therefore, the pseudo-inverse solution is not found to be acceptable.

Null-space basis vectors (Section 4.4) are derived for the matrices of the *ARS*s related to the 3-*RRR* and the 3-*RPR PMs*. A general wrench intensity solution is expressed as a particular solution plus a homogeneous solution. The homogeneous solution is formed from the derived null-space basis vectors with the 2nd joint wrench intensities acting as the multipliers (Section 4.5).

Ensuring base joint wrench intensities by sacrificing elbow joint values is presented in Section 4.6. An algorithm using an optimization-based method for ensuring non-reversing actuator outputs is presented (Section 4.7). The algorithm uses the *MATLAB* routine *FMINCON*. Section 4.8 presents routines and constraints required to allow the optimization-based (*FMINCON*) method, ensuring non-reversing actuator outputs, to be implemented. The implementation routines and constraints consist of: sinusoidal functions that ensure non-reversing base joint wrench intensities (Section 4.8.1); and constraints to ensure non-reversing actuator-output values (Section 4.8.2).

A discussion in Section 4.9 summarizes the contributions of this chapter. Results from the optimization-based (*FMINCON*) non-reversing actuator-output solutions are presented in Chapter 5.

4.2 Static Force Problem for Redundantly Actuated *PM*s

Reduction of backlash in *PM*s through the use of actuation redundancy is investigated in the research presented in this Chapter. Using actuation redundancy to pre-load the actuators' outputs has been found in this research to be effective for reducing output sign-switching in 3-*RRR* (Figure 4.1) and 3-*RPR* (Figure 4.2) planar *PM*s.

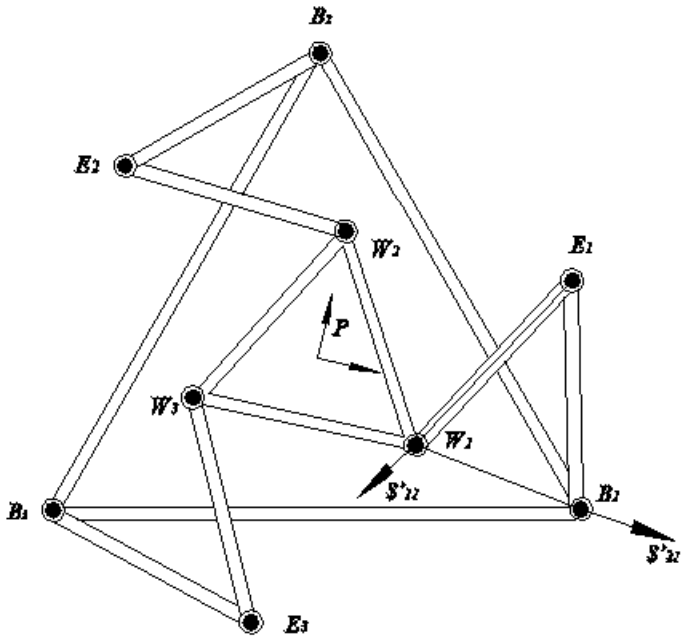

Figure 4.1: Redundantly Actuated 3-*RRR* PM and *ARSs* $\$'_{11}$ and $\$'_{21}$ for Branch 1.

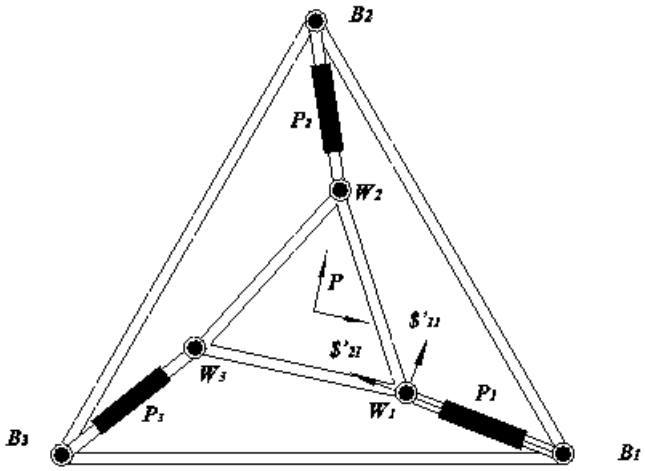

Figure 4.2: Redundantly Actuated 3-*RPR PM* and *ARSs* $\boldsymbol{\$}'_{11}$ and $\boldsymbol{\$}'_{21}$ for Branch 1.

For the case of the redundantly-actuated 3-*RRR* or 3-*RPR PM*s, the number of branches is three and two joints (base revolute and elbow revolute or base revolute and prismatic sliding) are actuated per branch. In terms of *ARS*s ${}^{B}\boldsymbol{\$}'s$, wrench intensities $\boldsymbol{w}_{ji}$ and the force to be applied, ${}^{B}\mathbf{F}$, the static force problem can be expressed by:

$$ {}^{B}\mathbf{F}_{3\times1} = {}^{B}[\$'_{11},\$'_{12},\$'_{13},\$'_{21},\$'_{22},\$'_{23}]\{w_{11},w_{12},w_{13}w_{21},w_{22},w_{23}\}^{T} = {}^{B}\$'_{6}\boldsymbol{w}_{6}, \qquad (4\text{-}1) $$

Equation (4-1) is under-determined (Strang (1988)) in terms of the required wrench intensities, $\boldsymbol{w}_{ji}$, j = 1 and 2, i = 1, 2 and 3; for a known force value, ${}^{B}\mathbf{F}_{3x1}$. For convenience, the six *ARS*s, $\boldsymbol{\$}'_{ji}$, j = 1 and 2, i = 1, 2 and 3, have been grouped in the matrix ${}^{B}\boldsymbol{\$}'_{6}$ and the six wrench intensities have grouped in the vector $\boldsymbol{w}_6$. In terms of mechanism synthesis (Erdman and Sandor (1996)), Equation (4-1) would be referred to as having 3 orders of infinity ($O(\infty^3)$) of solutions for $\boldsymbol{w}_6$ for a desired ${}^{B}\mathbf{F}$. Note, the solution of Equation (4-1) is also subject to the constraints of having non-reversing wrench intensities.

4.3 Static Force Solutions for Redundantly-Actuated *PM*s based on Pseudo-Inversion of the *ARS*s Matrix

Matrix ${}^{B}[\$'_6]_{3x6}$ is due to six actuated joints and is of dimension 3×6. There are three dimensions of solutions for the six elements of $\boldsymbol{w}_6$. Within robotics Whitney (1969) and (1972) suggested using the right-Moore-Penrose pseudo-inverse, $\boldsymbol{J}^{I}$ (Strang (1988)) of the Jacobian matrix, $\boldsymbol{J}$, for joint redundant serial manipulators. A right-Moore-Penrose pseudo-inverse of ${}^{B}\$'_6$ would yield:

$$\boldsymbol{w}_6 = {}^{B}\$'^{I}_6 {}^{B}\mathbf{F}, \tag{4-2}$$

where ${}^{B}\$'^{I}_6 = {}^{B}\$'^{T}_6(\$'_6 {}^{B}\$'^{T}_6)^{-1}$. Note that a Moore-Penrose pseudo-inverse solution will return a solution with the minimum 2-norm (Strang (1988)) of the elements of $\boldsymbol{w}_6$.

Researchers used weighted right-Moore-Penrose pseudo-inverses to minimize local objectives for serial manipulators, eg,, Kircanski and Vukobratovic (1984) used a weighted pseudo-inverse formulation to minimize the total energy consumed by the actuators during task execution. Klein (1985) and Yoshikawa (1985) suggested dexterity measures and used weighted pseudo-inverses to optimize these measures. Note solutions based on weighted Jacobian pseudo-inverses are local optimizations, i.e., only consider data based on the instant considered and are not a global optimization. Podhorodeski (1989) and Podhorodeski *et al*. (1991 and 1993) formulated the redundant serial manipulator objectives previously considered in terms of weighted Jacobian matrix pseudo-inverses in terms of Jacobian null-space basis vector pseudo-inverses. The solution of the inverse instantaneous kinematic problem and the derivation of the null-

space basis vectors were done through a decomposition of screw coordinates representing the manipulator joint axes. The use of Jacobian null-space basis vectors allowed analytical solutions to be found for the kinematically simple (Pieper and Roth (1969)) manipulators commonly used in industrial robot and outer-space applications. The solutions based on weighted Jacobian null-space basis vectors are also local in nature.

Nakumura and Hanafusa (1987), Suh and Hollerbach (1987), and Kazerounian and Wang (1988) present globally-optimal inverse instantaneous kinematic solutions for serial manipulators. These globally-optimal solutions require the optimization of higher-order kinematics, e.g., acceleration problems. Note that the pseudo-inverse of ${}^{B}\boldsymbol{\$}'_{6}$ would return a solution with the minimum 2-norm (Strang (1988)) of the elements of $\boldsymbol{w}_6$ but should not be expected to return a same-sign (zero-backlash) solution for the elements of $\boldsymbol{w}_6$.

Figures 4.3 and 4.4 illustrate the required joint torques for the 3-*RRR* and the 3-*RPR* *PM*s, executing the circle force trajectory described in Equation (3-1), using the right-Moore-Penrose pseudo-inverse solution. The wrench intensity to joint torque conversion of Equation (2-4) for actuated revolute joint torques ($\tau_{ji} = w_{ji}(\boldsymbol{\$}'_{ji} \circledast \boldsymbol{\$}_{ji})$ and Equation (2-9) for actuated prismatic joint forces ($f_{ji} = \boldsymbol{w}_{ji}$ (1)) are used in this solution.

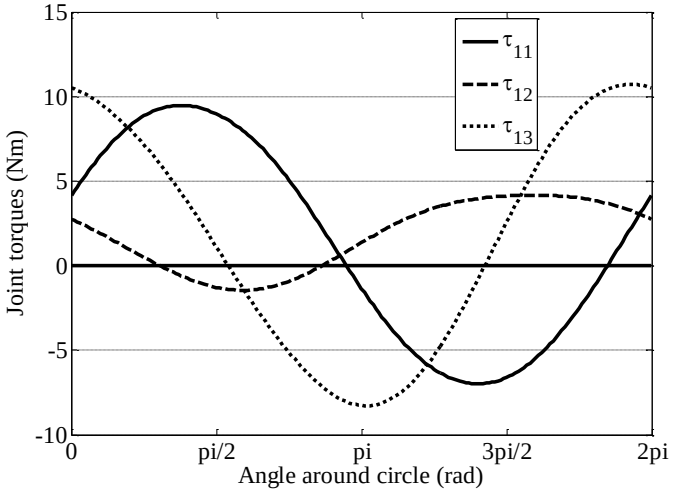

a) Base (1st) joint torques.

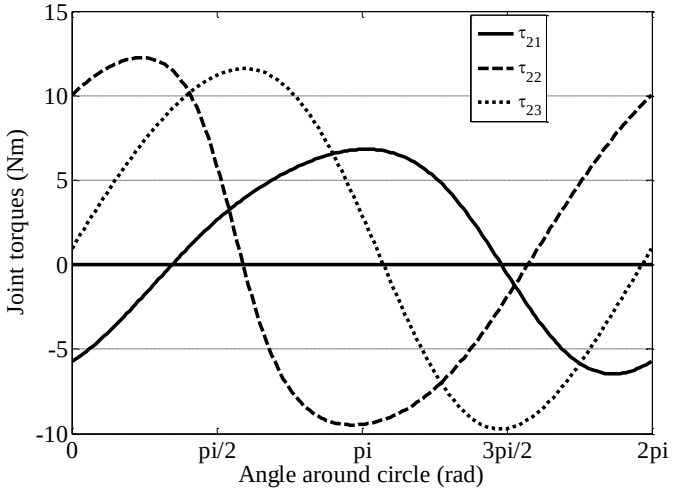

b) Elbow (2nd) joint torques.

Figure 4.3: 3-*RRR PM* Joint Torques to Follow Circle Trajectory using Pseudo-inverse Solution.

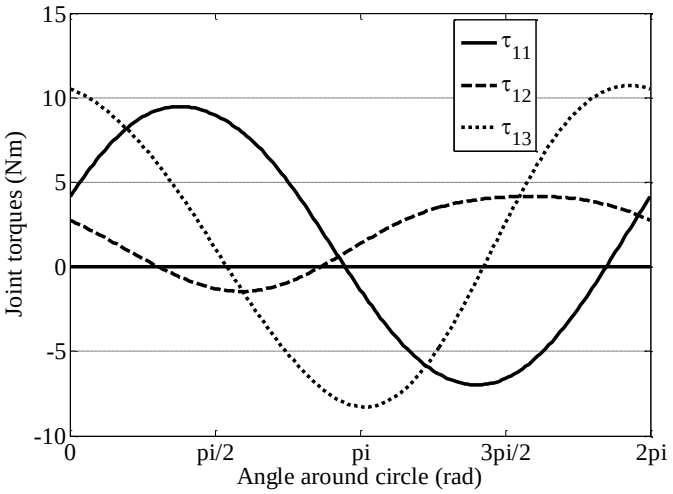

a) Base (1st) joint torques.

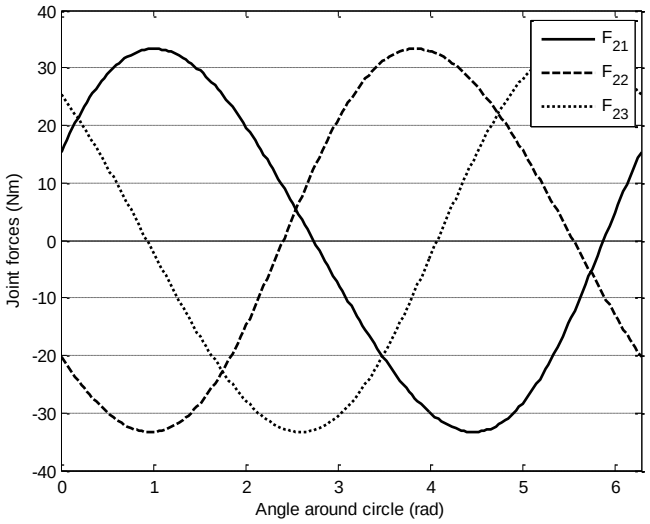

b) Prismatic (2nd) joint forces.

Figure 4.4: 3-*RPR PM* Joint Torques and Forces to Follow Circle Trajectory using Pseudo-inverse Solution.

.

For the spiral trajectory described by Equation (3-2) and for the applied wrench of Equation (3-3), the pseudo-inverse solution for the actuated torques and forces is shown in Figures 4.5 and 4.6 for the 3-*RRR* and 3-*RPR PM*s.

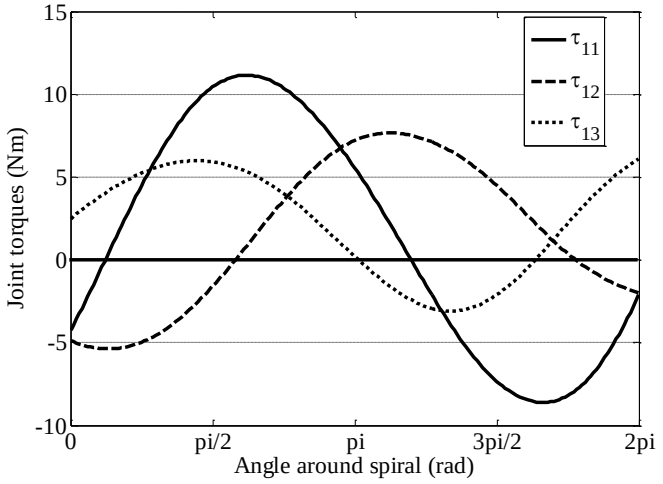

a) Base (1st) joint torques.

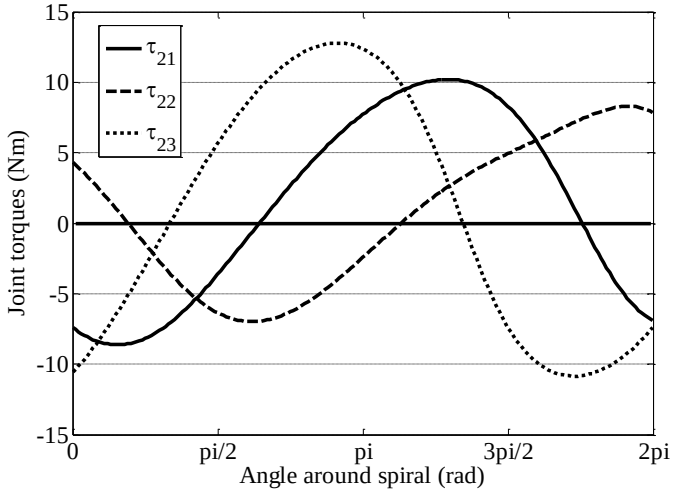

b) Elbow (2nd) joint torques.

Figure 4.5: 3-*RRR PM* Joint Torques to Follow Spiral Trajectory using Pseudo-inverse Solution.

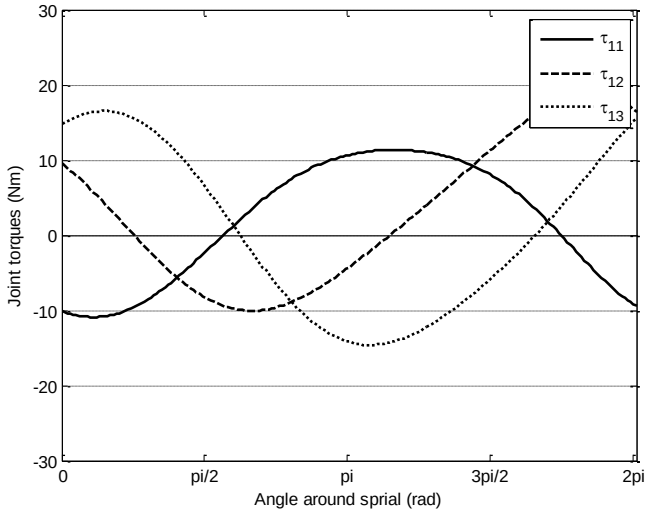

a) Base (1st) joint torques.

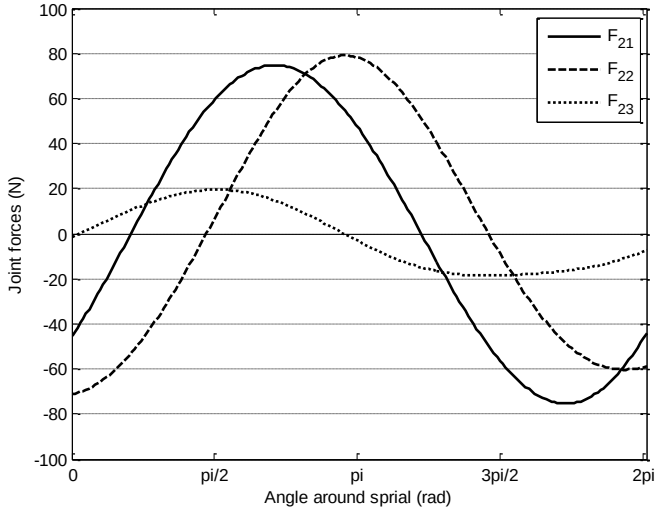

b) Prismatic (2nd) joint forces.

Figure 4.6: 3-*RPR PM* Joint Torques and Forces to Follow Spiral Trajectory using Pseudo-inverse Solution.

For the arc trajectory and for the applied wrench of Equation (3-4), the pseudo-inverse solution for the actuated torques and forces is shown in Figures 4.7 and 4.8 for the 3-*RRR* and the 3-*RPR PMs*. (Note, the arc trajectory is defined for 0 to 2 radians in Chapter 3).

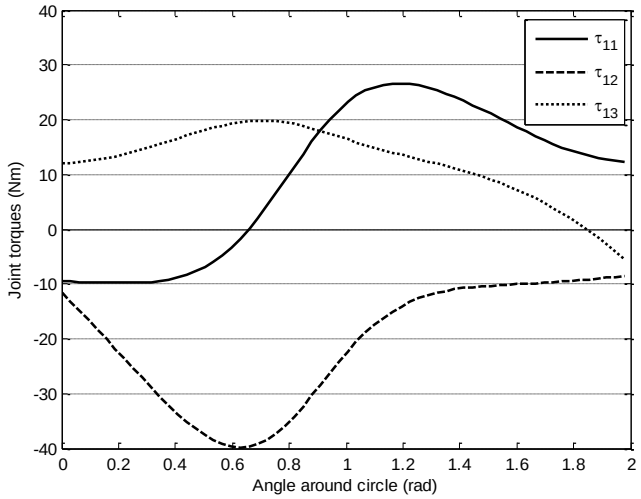

a) Base (1st) joint torques.

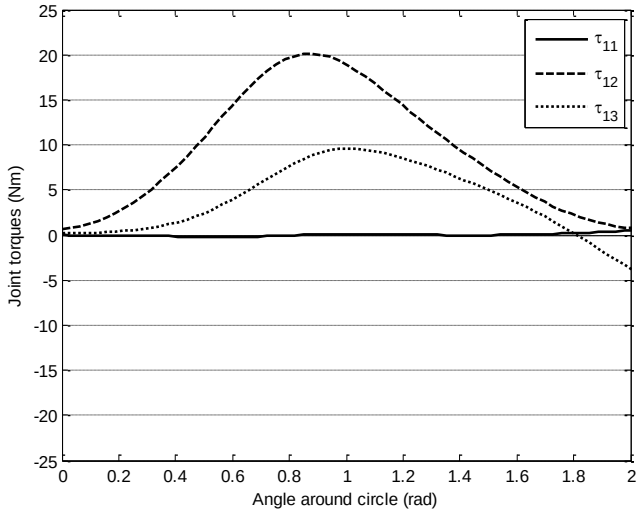

b) Elbow (2^{nd}) joint torques.

Figure 4.7: 3-*RRR PM* Joint Torques to Follow Arc Trajectory using Pseudo-inverse Solution.

.

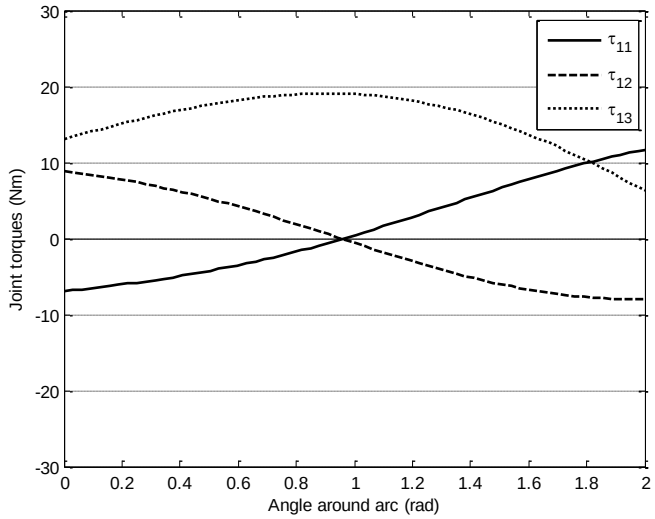

a) Base (1^{st}) joint torques.

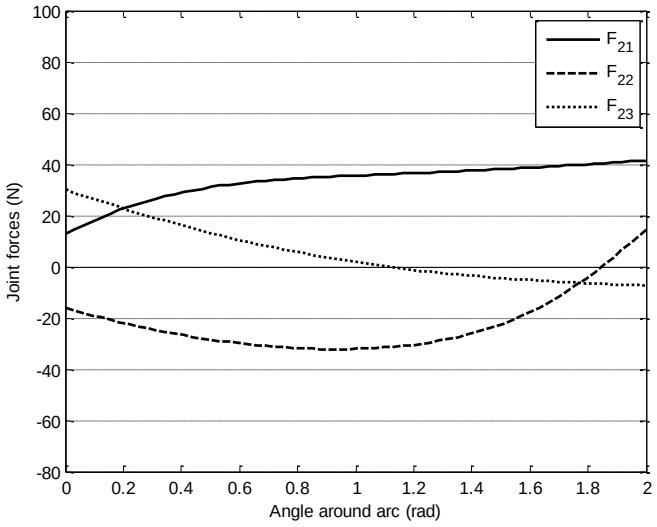

b) Prismatic (2^{nd}) joint forces.

Figure 4.8: 3-*RPR PM* Joint Torques and Forces to Follow Arc Trajectory using Pseudo-inverse Solution.

.

From the pseudo-inverse solutions of Figures 4.3 - 4.8, it can be seen that pseudo-inverse solutions do not ensure that the joint output forces are non-reversing, i.e., all of the joint torques and forced switch from positive to negative or vice-versa two times. Therefore, this solution will not be considered further, except as a potential particular solution.

4.4 Null-space Basis Vectors for ${}^{B}\$'_{6}$

A single sense solution for the elements of $\boldsymbol{w}_6$ can be achieved by exploiting null-space basis vectors of $\$'_6$. One approach for finding null-space basis vectors of $\$'_6$ is by first

resolving magnitudes required to produce $\$'_{21}$, $\$'_{22}$, and $\$'_{23}$ using the screw coordinate quantities of $\$'_3$. Consider the vectors v_i that satisfy the following relation:

$$\$'_3\mathbf{v}_i + \$'_{2i} = 0 \text{ or } \mathbf{v}_i = \$'^{-1}_3(-\$'_{2i}), \quad i = 1,2,3, \tag{4-3}$$

where $\$'_3 = {}^B[\$'_{11}\ \$'_{12}\ \$'_{13}]$. Three 6×1 null-space basis vectors for $\$'_6$ can be assembled as:

$$\boldsymbol{V}_1 = \{\mathbf{v}_1^T, 1,0,0\}^T; \tag{4-4a}$$

$$\boldsymbol{V}_2 = \{\mathbf{v}_2^T, 0,1,0\}^T; \tag{4-4b}$$

and

$$\boldsymbol{V}_3 = \{\mathbf{v}_3^T, 0,0,1\}^T. \tag{4-4c}$$

Note that:

$$\$'_6[\boldsymbol{V}_1\boldsymbol{V}_2\boldsymbol{V}_3] = \mathbf{0}_{3\times3}, \tag{4-5}$$

i.e., the vectors $\boldsymbol{V}_i$, i = 1, 2, 3, form a null-space basis of $\$'_6$. Wrench intensities based on multiples of the null-space basis vectors cause forces internal to the *PM*.

The method of Equations (4-3) and (4-4) of finding a null-space basis is related to the force solutions used in this Dissertation. That is, $\$'_3 = [\$'_{11}\ \$'_{12}\ \$'_{13}]$ is being used to find a particular solution for the force problem and $\$'_{21}$, $\$'_{22}$, and $\$'_{23}$ are being treated as additional (redundant) forces from which null-space basis vectors are formed. As shown in the Section 4.5, these null-space basis vectors can be used to form a homogeneous solution for the force problem.

4.5 General Wrench Intensity Solutions

General wrench intensity solutions for the 3-*RRR* and the 3-*RPR PM*s can be expressed as:

$$\boldsymbol{w}_6 = \{\boldsymbol{w}_\mathrm{p}\}_{6\times1} + \{\boldsymbol{w}_\mathrm{h}\}_{6\times1}. \tag{4-6}$$

In Equation (4-6), $\boldsymbol{w}_\mathrm{p}$ is a particular solution that produces the desired wrench ${}^{B}\mathbf{F}$, for example, $\boldsymbol{w}_\mathrm{p} = {}^{B}\boldsymbol{\$}_6{}^{\mathrm{I}}\,{}^{B}\mathbf{F}$, the right-Moore-Penrose pseudo-inverse solution, is one of several possible particular solutions. Other examples of particular solutions include those formed by using the non-redundant *PM* force solutions of Chapter 3. Also in Equation (4-6), $\boldsymbol{w}_\mathrm{h}$ is a homogeneous wrench intensity solution that lies in the null-space of $\boldsymbol{\$}_6$. Specifically, for the chosen null-space basis vectors of Section 4.4:

$$\{\boldsymbol{w}_\mathrm{h}\}_{6\times1} = [\boldsymbol{V}_1\boldsymbol{V}_2\boldsymbol{V}_2]_{6\times3}\{w_{21}, w_{22}, w_{23}\}^{\mathrm{T}}_{3\times1}, \tag{4-7}$$

i.e., the solution for $\boldsymbol{w}_\mathrm{h}$ is dependent on the values chosen for the 2nd joint wrench intensities w_{21}, w_{22} and w_{23}. The wrench intensities of $\boldsymbol{w}_\mathrm{h}$ result in self-cancelling internal forces.

4.6 Values for w_{21} , w_{22} , and w_{23} to Ensure Desired w_{11}, w_{12} and w_{13} Intensities

To ensure specific (including non-reversing) w_{11}, w_{12} and w_{13}, let $w_{11\mathrm{d}}$, $w_{12\mathrm{d}}$ and $w_{13\mathrm{d}}$ be the desired values for w_{11}, w_{12} and w_{13}. Assume that particular values for $w_{11\mathrm{p}}$, $w_{12\mathrm{p}}$ and $w_{13\mathrm{p}}$ have been found from:

$$\boldsymbol{w}_\mathrm{p} = \{w_{11\mathrm{P}}, w_{12\mathrm{P}}, w_{13\mathrm{P}}\}^{\mathrm{T}} = {}^{\mathrm{B}}\$_3^{-1}\,{}^{\mathrm{B}}\mathbf{F}. \tag{4-8}$$

The difference $\boldsymbol{w}_{df}$ between the desired values and the particular values found in Equation (4-8) is given by:

$$\boldsymbol{w}_{df} = \{w_{11df}, w_{12df}, w_{13df}\}^T = \{w_{11d}, w_{12d}, w_{13d}\}^T - \{w_{11p}, w_{12p}, w_{13p}\}^T. \quad (4\text{-}9)$$

The elbow (or prismatic) joint wrench intensities $\{w_{21c}, w_{22c}, w_{23c}\}^T$ generating a $\mathbf{w}_h$ compensating for $\{w_{11df}, w_{12df}, w_{13df}\}^T$ are:

$$\{w_{21c}, w_{22c}, w_{23c}\}^T = [\mathbf{v}_1\mathbf{v}_2\mathbf{v}_3]^{-1}\{w_{11df}, w_{12df}, w_{13df}\}^T, \quad (4\text{-}10)$$

The following equation shows that any desired wrench intensities $\{w_{11d}, w_{12d}, w_{13}\}^T$ for the first joint found by summing a homogeneous solution based on $\{w_{21c}, w_{22c}, w_{23c}\}^T$ with the particular solution $\{w_{11p}, w_{12p}, w_{13p}\}^T$ produces the correct intensities:

$$\begin{aligned} \boldsymbol{w}_d &= \{w_{11d}, w_{12d}, w_{13d}\}^T \\ &= {}^B\$_3^{-1B}\mathbf{F} + [\mathbf{v}_1\mathbf{v}_2\mathbf{v}_3]\{w_{21c}, w_{22c}, w_{23c}\}^T \\ &= \boldsymbol{w}_p + \{w_{11df}, w_{12df}, w_{13df}\}^T \\ &= \boldsymbol{w}_p + \{\boldsymbol{w}_d - \boldsymbol{w}_p\} = \boldsymbol{w}_d. \end{aligned} \quad (4\text{-}11)$$

For the problem under consideration, non-reversing torques (for revolute) or non-reversing forces (for prismatic) are desired for all of the actuated joints.

4.7 Optimization-based Method for Ensuring Non-Reversing Actuator Outputs

It is desired to find backlash-free torques (for revolute) or forces (for prismatic) for the actuated joints, to follow a trajectory while the manipulator is subjected to an external

wrench. Note that the following discussion is in terms of wrench intensities but it is also valid for torques (or forces) since the conversion is easily obtained with Equation (2-4) or (2-9). It is possible to impose desired non-reversing intensities for the base joints. Elbow *R* joint (for 3-*RRR PMs*) or *P* joint (for 3-*RPR PM*s) wrench intensities can then be computed using Equation (4-10) for desired values. To ensure that the computed joint torque (for 3-*RRR PM*s) or joint force (for 3-*RPR PMs)* wrench intensities do not change sign (are non-reversing) the solution was formulated as a constrained non-linear optimization problem. The *MATLAB* routine *FMINCON* is used in a constrained optimization-based solution.

The multiplicity of solutions to the static force problem for an actuation-redundant *PM* allows the minimization of an objective function $OF = \sum_{i=1}^{n} L_i$ along a trajectory divided into *n* discrete points. The cost function is chosen here as $L_i = \boldsymbol{\tau}_i^T \boldsymbol{\tau}_i$ where $\boldsymbol{\tau}_i$ represents the vector of actuated joint torques (or forces) at the i^{th} position along the trajectory. The method is summarized as follows:

a) Specify a function that does not change sign for the base joint wrench intensities, i.e., desired values $\boldsymbol{w}_{1id}$, i = 1, 2, 3. The parameters that define the function are the search variables for the optimization. Then at each step of the trajectory:
   i. Compute the *ARS* of each actuated joint;
   ii. Compute the null-space basis vectors $\boldsymbol{v}_i^T$ using Equation (4-3);
   iii. Calculate a particular wrench intensity solution $\boldsymbol{w}_p = \{w_{11p}, w_{12p}, w_{13p}\}^T$ using Equation (4-8) (other methods are possible for finding $\boldsymbol{w}_p$);

iv. Calculate the vector $\{w_{11df}, w_{12df}, w_{13df}\}^T$ containing the difference between the desired wrench intensity $\{w_{11d}, w_{12d}, w_{13d}\}^T$ at the base joints and the particular solution $\{w_{11p}, w_{12p}, w_{13p}\}^T$ using Equation (4-9);

v. Resolve $\{w_{21c}, w_{22c}, w_{23c}\}^T$ using Equation (4-10) to determine the elbow joint wrench intensities required to compensate for the difference;

vi. Convert the wrench intensities into joint torques or forces using Equation (2-4) for revolute actuators or (2-9) for prismatic actuators;

b) Stop when the n^{th} step in the trajectory has been reached;

c) Compute the objective function $OF = \sum_{i=1}^{n} L_i$ where $L_i = \boldsymbol{\tau}_i^T \boldsymbol{\tau}_i$.

The problem is solved using the non-linear constrained optimization algorithm *FMINCON* from *MATLAB*'s optimization toolbox. This function uses a sequential quadratic programming method. Non-reversing signs of the computed elbow *R* (or *P*) torques (or forces) were added as constraints in the optimization routine.

4.8 Implementation Routines for the Optimization-based (*FMINCON*) Solutions for Non-Reversing Actuator Outputs

4.8.1 Sinusoidal Functions for Base Joint Wrench Intensities

As outlined in Section 4.7 step "a," the first step to achieve non-reversing actuator outputs is to specify functions for the desired base joint wrench intensities. To avoid backlash, these functions must be non-reversing. It can be seen in Figure 4.3 and 4.4 that

the torques obtained with the pseudo-inverse solution are similar to sine waves. Due to this, and also due to the simplicity in specifying the function's sign, sine waves are utilized as functions for the desired wrenches of the base joints. To ensure that they do not change sign, the following function was used:

$$\boldsymbol{w}_{1id} = \boldsymbol{w}_i + \alpha_i \boldsymbol{w}_i \sin(\theta + \gamma_i) \quad i = 1,2 \text{ and } 3 \tag{4-12}$$

where $\boldsymbol{w}_i$, α_i, and Υ_i are the mean value, a factor setting the amplitude, and the phase angle, respectively, for the base joint desired wrench intensity value of branch *i*. Note that if the values of α_i are limited to values between 0 and 1, the resulting sine wave will never change sign. The search space thus consists of 9 variables, the three values introduced in Equation (4-12) for each of the three branches. The optimization algorithm searches for these variables with a constraint that the joint wrench intensities of the elbow joints that are computed in steps a)i through a)vi of Section 4.7 are non-reversing.

The trajectory was divided into 200 intervals to produce 201 points where the steps a)i through a)vi of Section 4.7 are computed. Note that step a)iii of Section 4.7 ensures that a particular wrench intensity solution for the desired force is found. Steps a)i, a)ii, a)iv and a)v are related to finding a homogeneous (self-cancelling) wrench intensity solution. Step a)vi converts the wrench intensity values to joint torques for *R* joints or to joint forces for *P* joints. Step b) is related to stopping the computation when the n^{th} step in the trajectory has been reached. Step c) computes the objective function value. In the optimization algorithm, the following bounds were used for the search terms that appear in Equation (4-12):

$$5 \leq wi \leq 100;$$

$$0.1 \leq \alpha_i \leq 0.9; \qquad (4\text{-}13)$$

$$0 \leq \Upsilon i \leq \pi; \qquad i = 1, 2, \text{ and } 3.$$

Note that when negative desired joint wrench intensities are specified, the mean value is bounded by $-100 \leq \boldsymbol{w}_i \leq -5$.

4.8.2 Constraints to Ensure Non-Reversing Intensity Values

Functions c defined in Equations (4-14a, -14b and -14c) are used to ensure non-reversing intensity values. The values $\boldsymbol{w}_{21}(1)$, $\boldsymbol{w}_{22}(1)$, and $\boldsymbol{w}_{23}(1)$ are the 2nd joint wrench intensities for the first, second, and third branches in the first position. The wrench intensities $\boldsymbol{w}_{21}(i)$, $\boldsymbol{w}_{22}(i)$, and $\boldsymbol{w}_{23}(i)$ for i = 2, … 201, are the 2nd joint wrench intensities for the second through 201st positions for the first, second and third branches in the ith position.

$$i = 2 : N+1$$

$$c(i) = w_{21}(1) * w_{21}(i); \qquad (4\text{-}14a)$$

$$c(i+N) = w_{22}(1) * w_{22}(i); \qquad (4\text{-}14b)$$

$$c(i+2N) = w_{23}(1) * w_{23}(i). \qquad (4\text{-}14c)$$

If $w_{21}(1)$, $w_{22}(1)$, and $w_{23}(1)$ are positive or negative, $w_{21}(i)$, $w_{22}(i)$ and $w_{23}(i)$ for i = 2, 3, … 201, must keep the same sign. If this is the case the c(i) values in Equations (4-14a, -14b and -14c) will always be positive. If the values of c(i) are negative, the case is rejected. The positive c(i) values are candidates in the optimization, and functions c are

penalty functions for *FMINCON*. These penalty functions constrain the elbow values to be the same sign (non-reversing).

MATLAB's *FMINCON* routine involves the following parameters:

X=*FMINCON* (FUN, X0, A, B, Aeq, Beq, LB, UB, NONNLCON). (4-15)

FUN is the objective function subject to the linear inequalities A * X <= B and subject to the linear equalities Aeq * X = Beq. X are the design variables (search variables). LB and UB define a set of lower and upper bounds on the design variables.

NONLCON accepts X and returns C and Ceq, representing the nonlinear inequalities and equalities.

Considering the constraint for ensuring same-sign actuator values and the lower and upper boundaries defined in Equations (4-13) the *FMINCON* parameters are:

$LB = [w_{1LB}, w_{2LB}, w_{3LB}, \alpha_{1LB}, \alpha_{2LB}, \alpha_{3LB}, \Upsilon_{1LB}, \Upsilon_{2LB}, \Upsilon_{3LB}]$

$= [5, 5, 5, 0.1, 0.1, 0.1, 0, 0, 0];$ (4-16a)

$UB = [w_{1UB}, w_{2UB}, w_{3UB}, \alpha_{1UB}, \alpha_{2UB}, \alpha_{3UB}, \Upsilon_{1UB}, \Upsilon_{2UB}, \Upsilon_{3UB}]$

$= [100, 100, 100, 0.9, 0.9, 0.9, \pi, \pi, \pi].$ (4-16b)

The above Equations (4-16a) and (4-16b) are for the +++ case of the base joint values. In total there are 7 further possible cases, i.e. ++-, +-+, +--, -++, -+-, --+, ---. All of the cases are simulated for the results presented in Chapter 5. Appendix D is an example of the *MATLAB* coding used for -+- case of the base joint outputs.

4.9 Discussion

4.9.1 On the Static Force Problem for the Redundantly Actuated *PM*s

This chapter considered the use of redundant (extra) actuated joints to guarantee non-reversing base actuator torques (for *R* joints) and forces (for *P* joints). Non-redundantly actuated *PM*s were found (Chapter 3) to require positive and negative joint torques (for actuated revolute joints) or forces (for actuated prismatic joints) to follow trajectories with arbitrary applied force directions. For redundantly actuated *PM*s, the static force problem was examined (Section 4.2). It was chosen to actuate the base-proximal joints (joints 1 and 2) for all three branches. The advantage to actuating base proximal joints is to keep additional masses and inertias as close to the base as possible. Having base-proximal actuation is an advantage of *PM*s allowing faster accelerations and higher accuracy in comparison to serial manipulators (Hunt (1983)).

With two joints actuated per branch a 3-branch *PM* was found to have an actuation *DOR* = 3 for planar force tasks. An alternative to having the 1st and 2nd joints actuated would be to consider a combination including the 3rd joint (Wei and Simon (2010)). Actuations including branch 3rd joints are recommended as potential future research in Section 6.4.

4.9.2 On the Static Force Solutions for Redundantly-Actuated *PM*s based on Pseudo-Inversion of the *ARS*s Matrix

Inspired by kinematically redundant serial manipulator solutions (Whitney (1969) and (1972); Khatib (1983); Yoshikawa (1985)), wrench intensity solutions based on right Moore-Penrose inverses (Strang (1988)) of the 3×6 dimensioned *ARS* matrix were utilized. These pseudo-inverse solutions were developed in Section 4.3 and were attempted for the 3-*RRR* and the 3-*RPR PMs* cutting circle, spiral and arc trajectories.

Within the discussion of Chapter 3, it is noted that the arc trajectory is a $\theta = 0$ to 2 radians segment of a circular trajectory $\theta = 0$ to 2π of a large radius. The required input forces and torques for the 3-*RPR PMs* for a "full-circle" arc trajectory without redundant actuation was reported in Figure 3.19 and 3.20 of Chapter 3. Full-circle has been placed in quote marks since an arc trajectory is not usually considered for a full-circle. The pseudo-inverse solution for the required input forces and torques to follow the full-circle arc trajectory, with both the base joint and elbow prismatic joint actuated, are shown in Figure 4.9a and b.

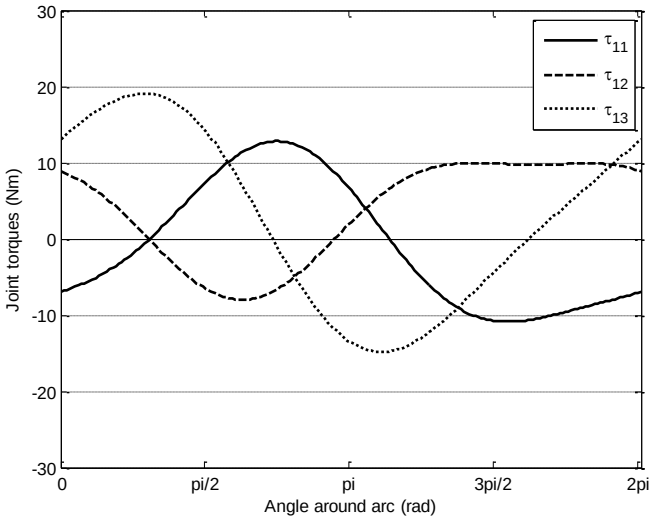

a) Base (1st) Joint Torques

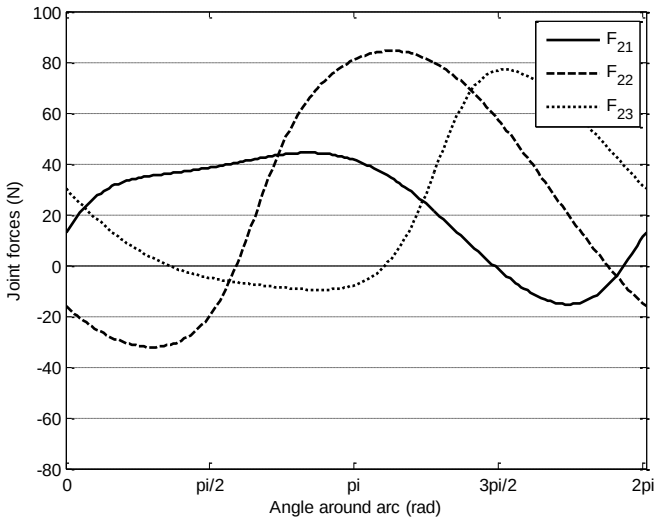

b) Prismatic (2nd) Joint Forces

Figure 4.9: 3-*RPR PM* Joint Torques and Forces to Follow the Full-circle Arc Trajectory using the Pseudo-inverse Solution.

Compare the non-redundantly actuated solution (Figure 3.19 and 3.20) and the redundant pseudo-inverse solution (Figure 4.9a and b) for the full-circle arc trajectory. Notice that the input torques and forces required for the pseudo-inverse solution have as expected lower magnitudes than the non-redundant solutions. The pseudo-inverse solution actually has the lowest possible solution for optimization of a 2-norm objective (Strang 1988) of the actuated joint forces (torques or forces depending on actuated joint type). The pseudo-inverse solution, however, does not reduce backlash (i.e., there is sign switching on all of the actuated joints). Since actuator sign switching could not be avoided, pseudo-inverse solutions are not considered any further in this research, except as potential particular solutions.

4.9.3 On the General Wrench Intensity Solutions

For a linear system with redundancy, a general solution comprised of a particular solution and a homogeneous solution (Strang 1988) can be found. This is the case for solving wrench intensities for static force problems requiring an arbitrary force to be produced with redundantly actuated *PM*s.

4.9.4 On the Null-space Basis Vectors for ${}^{B}[\$'_{6}]$

To represent the homogeneous solution, null-space basis vectors (Section 4.4) were derived for the *ARS* matrix. The derivation was based on resolving redundant *ARS*s back onto the *ARS*s used to form a particular solution. Numerically more stable methods are

available (e.g., *MATLAB* functions) to find null-space basis vectors for $\$'_6$. Within this Dissertation, both the null-space basis determination method of Section 4.4 and *MATLAB* functions have been used to find null-space basis vectors for $\$'_6$. These null-space basis vectors have been used to generate the presented results (both techniques find equivalent results).

4.9.5 On the Values for $w_{21}, w_{22},$ and w_{23} to Ensure Desired w_{11}, w_{12} and w_{13} Values

The null-space basis vectors lead to self-cancelling (internal) forces, and are used in this research for compensation (Section 4.5) to allow desired non-redundant wrench intensities. An algorithm (utilizing the *MATLAB* constrained optimization function *FMINCON*) for ensuring non-reversing actuated joint torque and/or force outputs is presented in Section 4.7.

4.9.6 On the Optimizations-based (*FMINCON*) Method for Ensuring Non-reversing Actuator Outputs

The *MATLAB* routine *FMINCON*, based on a sequential quadratic programming method, is discussed in Section 4.7 and requires the definition of equality and inequality constraints. Non-reversing joint torques (*R* joints) and forces (*P* joints) are formulated as inequality constraints in Section 4.8. These constraints ensure that the actuator outputs are always positive or negative depending on the sign of their initial values, i.e., the

actuator output values never cross zero. Note that the inequality constraints could also be defined such that the absolute joint output values satisfy a minimum value other than zero. This redefinition of the minimum absolute joint output values are also recommended as potential future research in Section 6.4.

4.9.7 On the Implementation Routines for the Optimization-based (*FMINCON*) Non-Reversing Actuator Values

A sine wave (Section 4.8.1) is used to model the desired wrench intensities. This curve is chosen because of its simplicity in specifying search parameters that assure same sense outputs. With the amplitude defined by a factor less than 1 (see Equation (4-12)), same sense outputs are guaranteed. It was noted that other functions could be used to ensure same sense outputs. As an example, consider the following function based on an arc-tangent (inverse-tangent) function.

Let:

$$\boldsymbol{w}_{1id} = \boldsymbol{w}_i + \alpha_i \boldsymbol{w}_i (\tan^{-1}(\theta + \gamma_I)/(\tfrac{\pi}{2})) \quad i = 1, 2, \text{ and } 3, \tag{4-17}$$

where $\boldsymbol{w}_i$, α_i, and Υ_i are again the mean value, a factor setting the amplitude, and a phase angle, respectively, for the base joint desired wrench intensity value of branch *i*. Note that the value of $(\tan^{-1}(\theta + \Upsilon_i)/(\pi/2))$ varies between 0 for $(\theta + \Upsilon_i) = 0$ and 1 for $(\theta + \Upsilon_i) = \infty$. If the values of α_i are limited to values between 0 and 1, the resulting inverse-tangent-based function will never change sign. The search space again consists of 9 variables $\boldsymbol{w}_i$, α_i, and Υ_i for each of the three branches. The optimization algorithm would

search for these variables with the before defined constraint that the joint wrench intensities of the elbow joints that are computed in steps a)i through a)vi of Section 4.7 are non-reversing. The search term constraints of Equation (4-13) would again be used. Again, please note that other curves could also be used as long as proper care of the function signs is taken.

If negative desired joint wrench intensities are specified, the mean value is bounded by $-100 \leq \boldsymbol{w}_i \leq -5$.

Constraints ensuring non-reversing (backlash-free) actuator outputs are presented in Section 4.8.2. These constraints provide a flag if the sense of the required actuator output force (torque for actuated *R* joint and force for actuated *P* joint) changes sign. The constraints function for both sign changes from positive to negative and from negative to positive.

Chapter 5

Results for Backlash Reduction using Actuation Redundancy

5.1 Overview of Chapter 5

Results for the reduction of backlash through the use of actuation redundancy are considered in Chapter 5. It was found in Chapter 3 that non-redundant actuation of a *PM* does not ensure backlash-free motion. With non-redundant actuation it was found that sign switching was required in the actuators. This sign switching requires backlash-prone zero-actuated joint forces (torques for actuated *R* joints, applied forces for actuated *P* joints). As noted earlier (Chapter 1) this actuator sign-switching results in the creation of backlash due to clearances in drive-chain components. In the non-redundant actuation of Chapter 3, either the first (base *R*) joint or the second (*R* elbow for 3-*RRR* or *P* for 3-*RPR* *PM*s) joint of each branch was considered to be actuated. In this Chapter, both the first

and the second joints of each branch are considered to be actuated simultaneously, i.e., 3-*RRR* or 3-*RPR* actuation.

Sections 5.2 and 5.3 present results from a non-reversing optimization-based (*FMINCON*) method to reduce the backlash associated with actuator sign-switching. Within Chapter 4, Section 4.7 an algorithm using *MATLAB* constrained optimization routine *FMINCON* is presented. Within Section 4.8, sub-sections present routines allowing the implementation of *FMINCON*. The implementation routines include: a non-reversing sinusoidal function and a non-reversing arc tangent function for base-joint wrench intensities to be found through optimization using *FMINCON* (sub-Section 4.8.1); and constraints allowing the implementation of *FMINCON* (sub-Section 4.8.2). Cutting force trajectories (circle, spiral and arc) of Chapter 3 will continue to be used in the examples presented in Chapter 5. Optimization-based (*FMINCON*) results for ensuring non-reversing actuator output values, and hence reduction of backlash-prone configurations, are found for the 3-*RRR PM*s in sub-Sections 5.2.2, 5.2.3 and 5.2.4, and for 3-*RPR PM*s in sub-Sections 5.3.2, 5.3.3 and 5.3.4. Section 5.4 discusses the reduction of force uncertainty configurations with the use of redundant actuation. A discussion in Section 5.5 summarizes the contributions of this chapter.

5.2 Results for the Optimization-based (*FMINCON*) Non-Reversing Actuator Values for the 3-*RRR PM*

5.2.1 3-*RRR PM*

The non-redundantly actuated 3-*RRR PM*'s configuration is considered in sub-Section 1.3 (manipulator layout), 2.5.1 (base joints actuated) and 2.5.2 (elbow joints actuated). The non-redundantly actuated 3-*RRR PM*s were found to require backlash-prone zero actuator-outputs. In Section 5.2, both the base and elbow joints are considered to be actuated simultaneously. This results in a 3-*RRR PM* with an actuation *DOR* = 3.

5.2.2 Optimization-based (*FMINCON*) solution for the 3-*RRR PM* (circle Trajectory)

Eight (2^3) different combinations of signs are possible for the desired wrench intensities of the three base joints (+++, ++-, +-+, +--, -++, -+-, --+, ---). All combinations were tested to find an optimized solution. Two of the combinations did not converge (*DNC*) to a solution, and for the six combinations that were able to satisfy the constraints of same-sense elbow torques, some performed better than others. The results obtained are sensitive to the initial input vector of the search variables. For combinations that did not converge, different initial vectors were tried to no avail. The results obtained are not necessarily a global optimum solution (*FMINCON* is a local optimization routine), but they nevertheless guarantee the reduction of backlash when following the trajectory.

Table 5.1 presents the optimization results for all the combinations tested. The objective function (*OF*) was divided by the number of points (n_{pts}) to report the average sum of torques squared for the trajectory. By dividing this value by the number of actuated joints, i.e., 6, and taking the square root, the average absolute value of the torques $|\boldsymbol{\tau}|$ along the trajectory is obtained.

Table 5.1: Optimization-based results, circle trajectory for the 3-*RRR PM*.

Combination	+ + +	+ + −	+ − +	+ − −	− + +	− + −	− − +	− − −
OF/n_{pts} (Nm)	802	779	*DNC*	7831	1180	1524	*DNC*	1333
$\|\boldsymbol{\tau}\|$ (Nm)	11.6	11.4	-	36.1	14.0	15.9	-	47.1

Table 5.1 shows that some combinations have better performance than others. Figure 5.1 presents the joint torques obtained after optimization with the ++- combination for the base joints to follow the circle trajectory; it is the lowest average absolute value of the required force. Note that none of the joint torques change sign and are cyclic (repeatable), i.e., the beginning point and ending point have the same value.

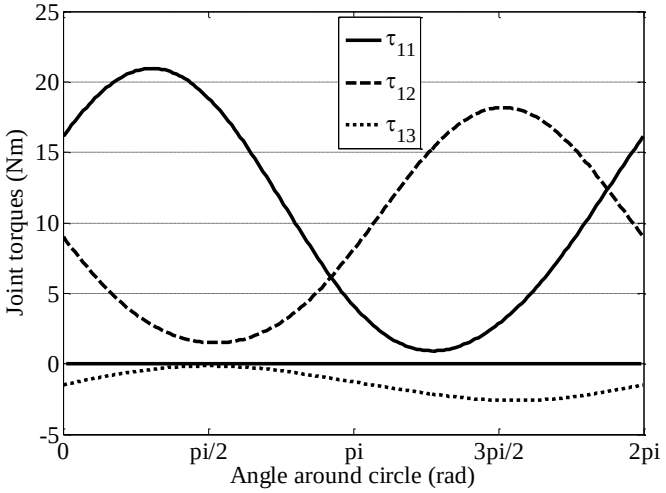

a) Base Joint Torques (circle Trajectory)

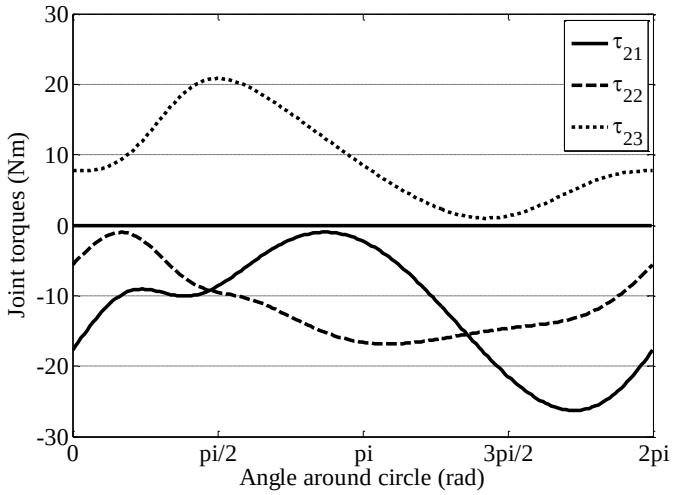

b) Elbow Joint Torques (circle Trajectory)

Figure 5.1: 3-*RRR PM* Optimization-based (*FMINCON*) Joint Torques to Follow Circle Trajectory using ++- Combination for the Base Joint Torques.

For this trajectory, a comparison of Figures 4.3a and b (pseudo-inverse) and 5.1a and b (optimization-based (*FMINCON*), non-reversing) indicates that an increase in the

magnitudes of the joint torques is required when ensuring non-reversing torque signs in comparison to pseudo-inverse solutions. This is not surprising since the pseudo-inverse generates the lowest 2-norm solution (Strang (1988)). Also the non-reversing constraint of the optimization results requires the solution to be only positive or only negative. This single-sign requirement increases the required magnitude of the wrench intensity (and therefore, torque) curves. However notice, the optimization-based (*FMINCON*) results require no reversal of the joint torques and therefore no backlash-prone actuator sign-switching.

5.2.3 Optimization-based (*FMINCON*) Solution for the 3-*RRR PM* (Spiral Trajectory)

The desired base joint wrench intensities are again modeled using Equation (4-12), the bounds in Equation (4-13), and the non-reversing elbow joint torque constraint. The eight possible combinations of the signs of the desired base wrench intensities are tested and are reported in Table 5.2.

Table 5.2: Optimization-based results, spiral trajectory for the 3-*RRR PM*.

Combination	+ + +	+ + −	+ − +	+ − −	− + +	− + −	− − +	− − −
OF/n_{pts} (Nm)	1211	6110	1260	DNC	DNC	3337	1137	2187
$\lvert\boldsymbol{\tau}\rvert$ (Nm)	14.2	31.9	14.5	-	-	23.6	13.8	19.1

Figure 5.2 illustrates the joint torques obtained after optimization with the combination --+ for the base joint signs. This combination has the smallest value for the objective function to follow the spiral trajectory. Note that in Figure 5.2(a), the desired sine wave curves for the base joint torques do not start and finish at the same amplitude. Starting and finishing with the same amplitude would be expected for a sine wave varying from 0 to 2π. The reason for different start and end values are that the start and end position on the spiral are not the same, as is the case for the circle trajectory.

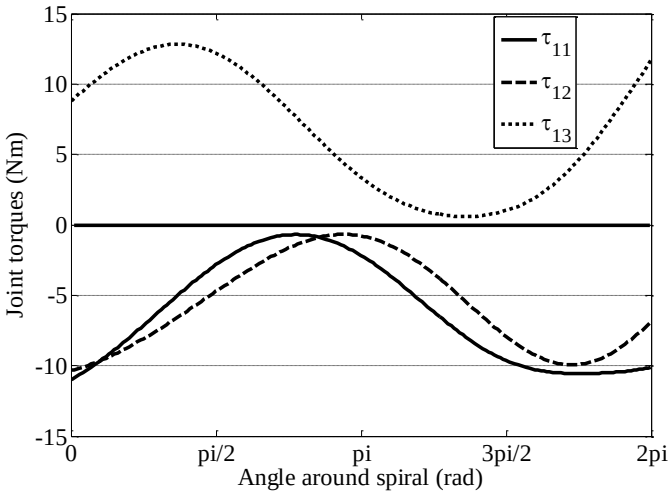

a) Base (1st) joint torques (spiral trajectory).

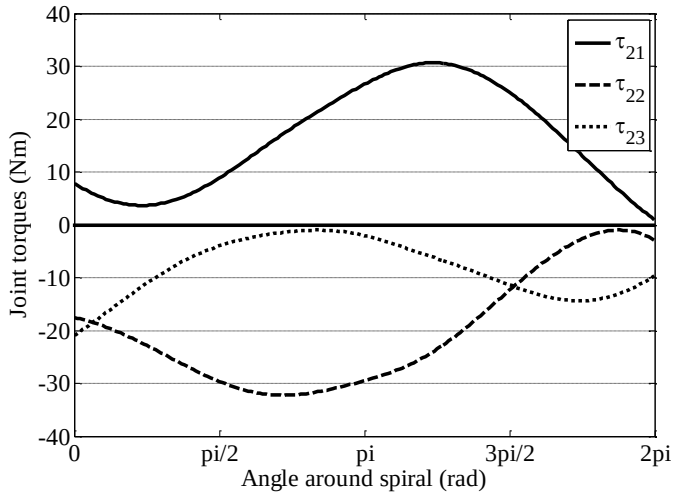

b) Elbow (2^{nd}) joint torques (spiral trajectory).

Figure 5.2: 3-*RRR PM* Optimized Joint Torques to Follow Spiral Trajectory using -- + Combination for the Base Joint Torques.

.

5.2.4 Optimization-based (*FMINCON*) Solution for the 3-*RRR PM* (arc Trajectory)

The method applied thus far fails for the 3-*RRR PM*, if it is applied to the arc trajectory described in Section 3.2.4. The *ARS*s of the base actuated joints, shown in Figure 5.3, almost collapse into a pencil of screws (Hunt (1978)), i.e., almost become a 2-system (singular for producing arbitrary planar forces). It can be observed that the *ARS*s of the first actuated joints of the first and second branches, which pass through the distal links, are almost aligned, and thus the three base actuated *ARS*s are close to meeting at a point.

In this case, matrix $\$'_3$ is ill-conditioned and problems occur when inverting $\$'_3$. This causes difficulties when the algorithm computes Equation (4-3) and (4-8).

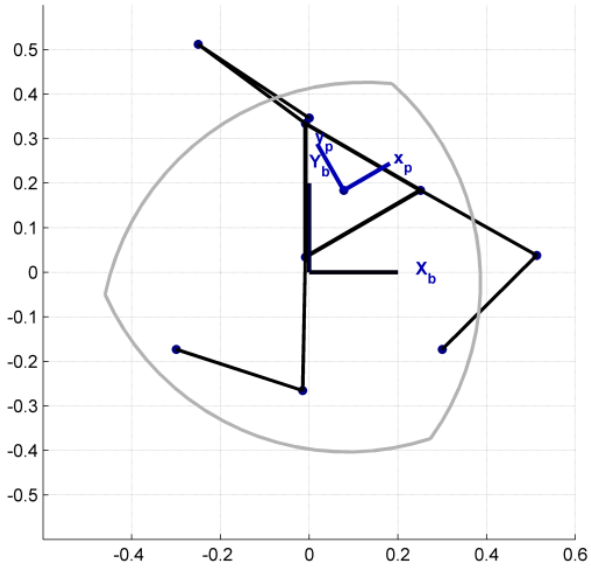

Figure 5.3: Near-singular Position of the 3-*RRR PM* when Following arc Trajectory.

To solve this problem, one can examine the static force problem, i.e., Equation (4 -1), for the 3-*RRR PM*. Instead of writing the equation as such, any order of the *ARS*s can be used. Since the first three screws produce a matrix that is almost singular, one of the *ARS*s of $\$'_3$ can be switched with one of the *ARS*s of the elbow actuated joints to create a better conditioned matrix. In what follows, a new matrix $\$^*_3$ is formed by switching the order of the *ARS*s $\$'_{21}$ and $\$'_{11}$ of branch 1 in matrix $\$'_3$. Note that this combination was chosen to reduce the close to degenerate (singular) condition described in the previous paragraph. The *ARS*s of the second branch could also have been chosen for switching.

Note that switching the *ARS*s of the third branch would not be a good choice since the *ARS*s of the base actuated joints of the first and second branches would still be almost aligned and the new matrix formed would also be ill-conditioned.

The new matrix formed by the switching proposed here is used in Equation (4-3) to compute the null-space basis vectors and in Equation (4-8) for the particular solution. The desired values are then specified for the wrench intensity values of the elbow-actuated joint of the first branch and for the base-actuated joints of branches 2 and 3, i.e., w_{21}, w_{12} and w_{13}. The compensation wrench intensities computed with Equation (4-10) are then obtained for the base-actuated joint of the first branch and for the elbow-actuated joints of branches 2 and 3. The method described in Sections 4.7 and 4.8.1 is basically followed but with different *ARS*s in the matrices.

The optimization algorithm was applied with the method described. A sine wave was again selected for the desired wrench intensities. It converged to a solution in six of the possible eight sign combinations for the desired wrench intensities. The optimization results are given in Table 5.3. The trajectory was again divided into 201 points. Figures 5.4a and b present the optimization results obtained with the -++ combination.

Table 5.3: Optimization-based results, arc trajectory for the 3-*RRR PM*.

Combination	+ + +	+ + −	+ − +	+ − −	− + +	− + −	− − +	− − −
OF/n_{pts} (Nm)	641	1852	*DNC*	*DNC*	461	822	1050	4842
$\lvert\boldsymbol{\tau}\rvert$ (Nm)	10.3	17.6	-	-	8.8	11.7	13.2	28.4

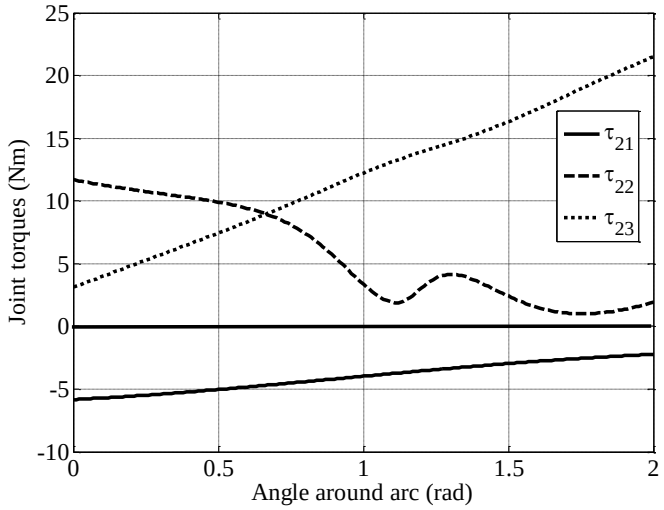

a) Base (1st) joint torques.

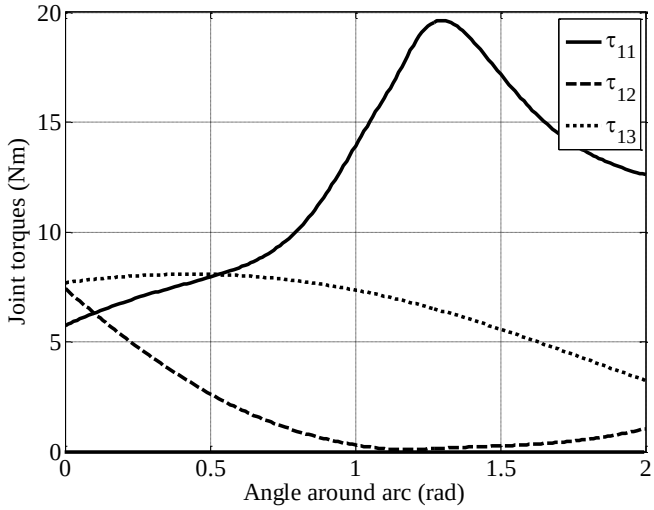

b) Elbow (2nd) joint torques.

Figure 5.4: 3-*RRR PM* Optimized Joint Torques to Follow Arc Trajectory using -++ Combination for the Desired Joint Torques.

5.3 Results f or the Optimization-based (*FMINCON*) Non-Reversing Actuator Values for the 3-*RPR PM*

5.3.1 3-*RPR PM*

The non-redundantly actuated 3-*RPR PM*'s configuration is considered in sub-Section 1.3 (manipulator layout), 2.5.3 (base joints actuated) and 2.5.4 (prismatic joint actuated). The non-redundantly actuated 3-*RPR PM*s were found to require backlash-prone zero-actuator outputs. In this Section both the base and prismatic joints are considered to be actuated simultaneously. This results in a 3-*RPR PM* with an actuation *DOR* of 3.

5.3.2 Optimization-based (*FMINCON*) solution for the 3-*RPR PM* (circle Trajectory)

For the 3-*RPR PM* case, there are prismatic joints rather than revolute joints for the 2nd joints of each branch. Due to this, the objective function:

$$\boldsymbol{OF} = wf_{11}\tau_{11} + wf_{21}f_{21} + wf_{12}\tau_{12} + wf_{22}f_{22} + wf_{13}\tau_{13} + wf_{23}f_{23}, \qquad (5\text{-}1)$$

is considered where the *wf*'s are weighting factors which reflect that the terms τ and f need to be weighted to reflect their importance within the objective. The weighting factors also considers the fact that the τ and the f terms have different units (*Nm* for the τ terms and *N* for the f terms) making the terms unit consistent. Since the individual elements of *OF* were found to have the same orders of magnitude all weights were chosen to have a unitary (1) value. To correct the unit inconsistency wf_{21}, wf_{22} and wf_{23} were assigned units of *m*, while wf_{11}, wf_{12} and wf_{23} were left without a unit.

Eight (2^3) different combinations of signs are considered for the desired wrench intensities of the three base joints (+++, ++-, +-+, +--, -++, -+-, --+, ---). All eight combinations converged to a solution and all of the combinations satisfied the constraints of non-reversing elbow forces. The +++ case performed better than the others and the results are shown in Figure 5.5. Note that the solution is a local optimal solution. Multiple initial start variables were tested, the reported values are the best found. The results obtained are not necessarily a global optimum solution (*FMINCON* is a local optimization routine), but they nevertheless guarantee non-reversing actuator values, when following the trajectory.

Table 5.4 presents the optimization results for all the combinations tested. The objective function (*OF*) was divided by the number of points to report the average weighted sum of torques (for *R* joints) and forces (for *P* joints) squared for the trajectory. By dividing this value by the number of actuated joints, i.e., 6, and taking the square root, the average absolute value of the forces $|\underline{f}|$ or torques $|\underline{\boldsymbol{\tau}}|$ along the trajectory is obtained.

Table 5.4: Optimization-based results (circle Trajectory) for 3-*RPR PM*.

Combination	+ + +	+ + −	+ − +	+ − −	− + +	− + −	− − +	− − −
OF/n_{points} (Nm)	1048	1171	1696	1975	1112	1524	1145	1301
$\lvert\underline{\boldsymbol{\tau}}\rvert$ (Nm)	13.2	14.0	16.8	18.1	13.6	15.9	13.8	14.7

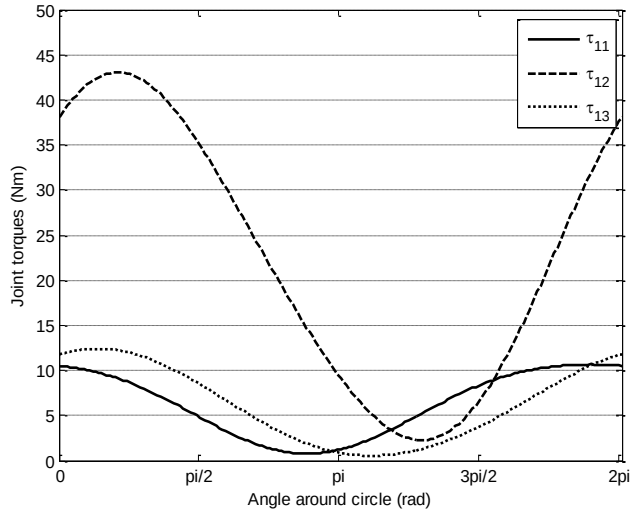

a) Base (1st) joint torques.

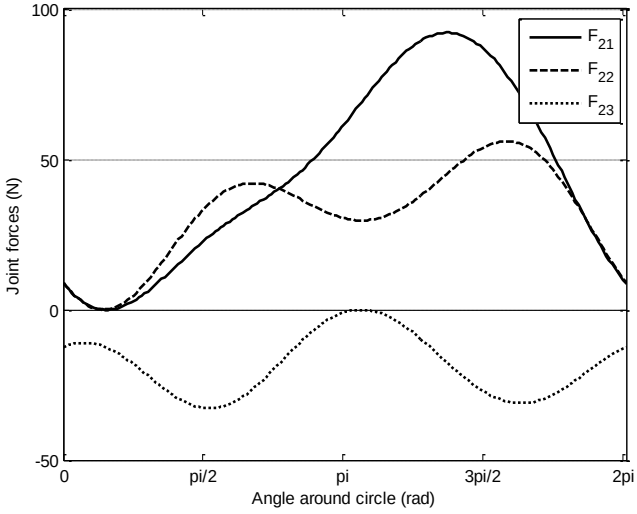

b) Prismatic (2nd) joint forces.

Figure 5-5: 3-*RPR PM* Optimization Joint Torques to Follow Circle Trajectory using +++ Combination for the Desired Joint Forces.

5.3.3 Optimization-based (*FMINCON*) Solution for the 3-*RPR PM* (spiral Trajectory)

For the spiral trajectory which is described by Equation (3-2) and the applied wrench of Equation (3-3), the non-redundantly actuated manipulators require reversing torques and forces at the actuated joints (Figure 3.8 and Figure 3.11). The desired base joint wrench intensities are again modeled using Equation (4-12), and the bounds in Equation (4-13) and same sign constraints are considered. The eight possible combinations of the signs of the desired wrench intensities are tested and are reported in Table 5.5. The optimization routine did not converge (*DNC*) for the --+ actuation of the base joints.

Table 5.5: Optimization-based results, spiral trajectory for the 3-*RPR PM*.

Combination	+ + +	+ + −	+ − +	+ − −	− + +	− + −	− − +	− − −
OF/n_{pts} (Nm)	950	1511	1391	1131	1434	1359	*DNC*	1184
$\|\underline{\boldsymbol{\tau}}\|$ (Nm)	12.6	15.9	15.2	13.7	15.5	15.1	-	14.1

The lowest objective function value was found with the +++ actuation of the base joints. The corresponding joint torque (for the base *R* joints) and joint forces (for the 2nd *P* joints) are shown in Figure 5.6.

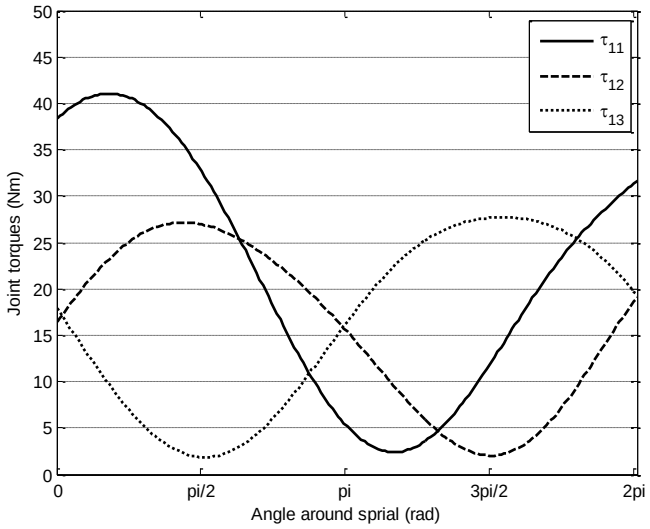

a) Base (1^{st}) joint torques.

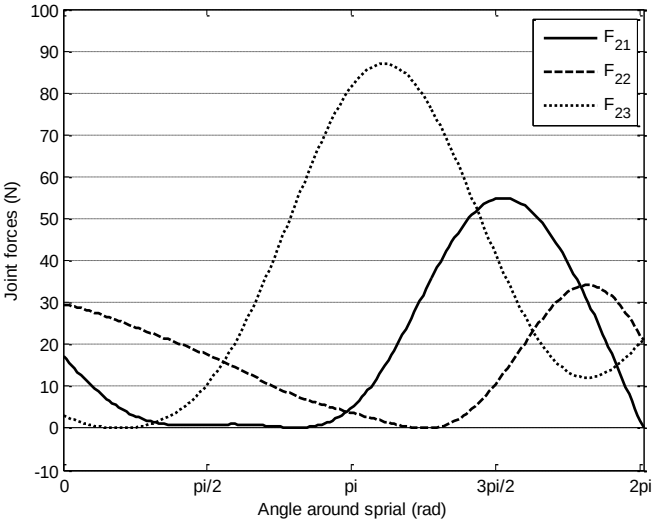

b) Prismatic (2^{nd}) joint forces.

Figure 5.6: 3-*RPR PM* Optimized Joint Torques to Follow Spiral Trajectory using +++ Combination for the Desired Joint Torques.

.

5.3.4 Optimization-based (*FMINCON*) Solution for the 3-*RPR PM* (arc Trajectory)

All eight combinations converged to solutions tabulated in Table 5.6. All combinations are also able to satisfy the constraint of non-reversing second-joint-actuator forces. The +++ in the Table 5.6 case performed better than the others and the results are shown in Figure 5.7. Note that the solution is a local optimal solution. Multiple initial start variables were tested, with the reported values being the best that were found. The results obtained are not necessarily a global optimum solution (*FMINCON* is a local optimization routine), but they never the less guarantee non-reversing first-joint-actuator torques when following the trajectory. The constraints of non-reversing second joint values ensure that non-reversing second joint actuator forces are also found.

Table 5.6: Optimization-based results, arc trajectory for the 3-*RPR PM*.

Combination	+ + +	+ + −	+ − +	+ − −	− + +	− + −	− − +	− − −
OF/n_{pts} (Nm)	354	409	1062	1226	416	510	936	646
$\lvert\boldsymbol{\tau}\rvert$ (Nm)	7.7	8.3	13.3	14.3	8.4	9.2	12.5	10.4

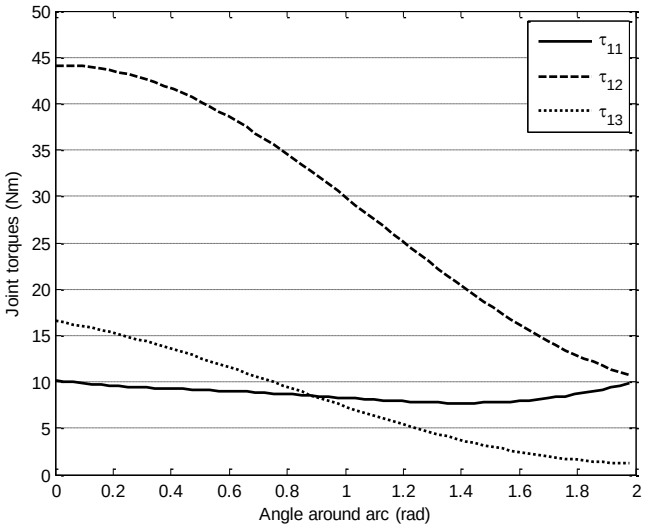

a) Base (1st) joint torques.

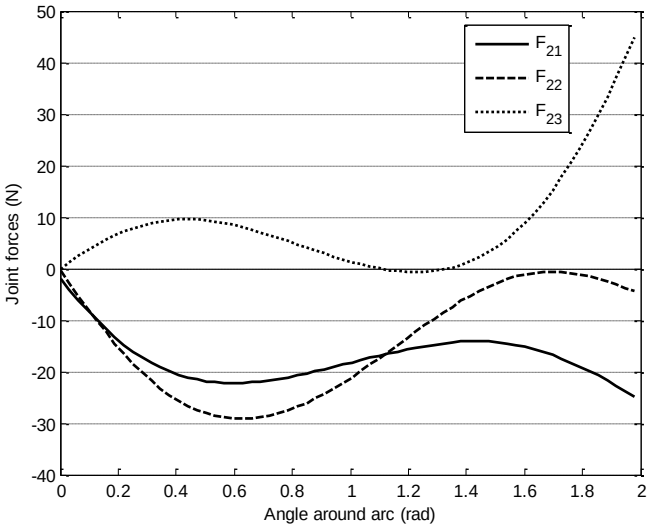

b) Prismatic (2nd) joint forces.

Figure 5.7: 3-*RPR PM* Optimization (*FMINCON*) Joint Torques to Follow Arc Trajectory using +++ Combination for the Desired Joint Torques.

5.4 The Reduction of Force Uncertainty Configurations with the use of Redundant Actuation

The redundantly actuated *PM*s, the 3-*RRR* and the 3-*RPR PM*s, considered in this Dissertation have three redundantly-actuated joints. These redundantly-actuated joints provide sufficient additional actuation forces to reduce all uncertainty configurations.

5.5 Discussion On the Results for the Optimization-based (*FMINCON*) Non-Reversing Actuator Values

The defined constraints for non-reversing joint wrench intensities and *FMINCON* are applied to the 3-*RRR* and 3-*RPR PM*s executing the three cutting tasks (circle, spiral and arc trajectories) defined in Chapter 3. A review of the parameters sent to *FMINCON* is given in Section 4.8.1.

The circle cutting trajectory is considered for the 3-*RRR* and 3-*RPR PM*s in Sections 5.2.2 and 5.3.2, respectively. Since the circle trajectory ends with the same joint displacements and cutting force requirements as it starts with, the actuator required values form closed curves (Figures 5.1 and 5.5). These closed curves are also referred to as being cyclic or as being repeatable.

The spiral cutting trajectory is considered for the 3-*RRR* and 3-*RPR PM*s in Sections 5.2.3 and 5.3.3. Since the spiral trajectory does not end with the same values as it starts with, the required actuator values do not form closed curves (Figures 5.2 and 5.6). The arc cutting trajectory is considered for the 3-*RRR* and 3-*RPR PM*s in Sections 5.2.4 and

5.3.4. Again, since the arc trajectory does not end with the same values as it started, the required actuator values (Figures 5.3 and 5.7) do not form closed curves (are not cyclic).

Within the discussion of Chapter 3, it is noted that the arc trajectory is a segment of $\theta = 0$ to 2 radians of a full-circle trajectory $\theta = 0$ to 2π of large radius. The required input forces and torques for the 3-*RPR PMs* for the full-circle of arc trajectory without redundant actuation was reported in Figure 3.19 and 3.20 of Chapter 3. The pseudo-inverse solution for the required input forces and torques with both the base joint and elbow prismatic joint actuated are shown in Figure 4.9a and b for the full-circle arc trajectory.

A solution for the required input torques and forces for the 3-*RPR PM* based on an optimization (*FMINCON*) is shown in Figure 5.8 for the full-circle arc trajectory.

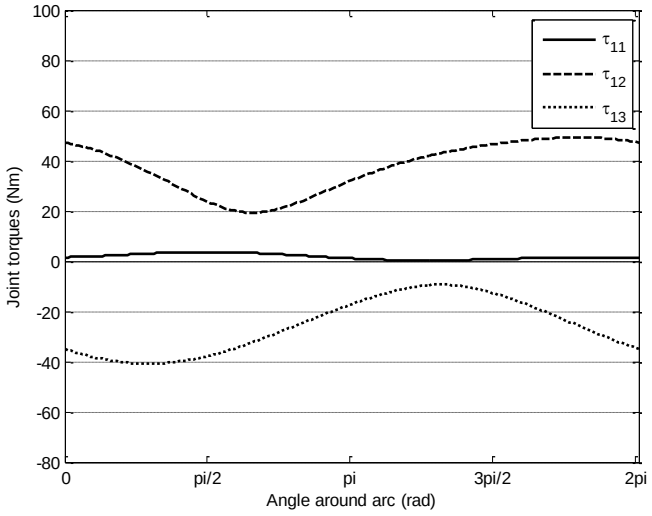

a) Base (1st) joint torques.

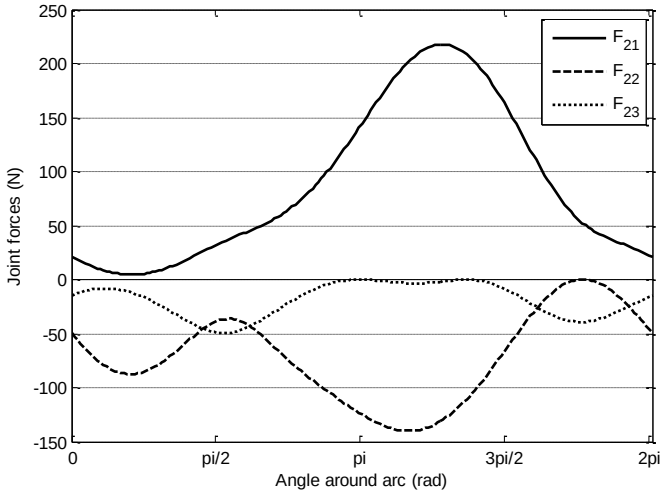

b) Prismatic (2^{nd}) joint forces.

Figure 5.8: 3-*RPR PM* Optimization (*FMINCON*) Joint Torques to Follow Full-Circle Trajectory using ++- Combination for the Joint Torques.

All three cases of the full-circle arc trajectory results including the non-redundant solutions (Figure 3.19 and 3.20), the pseudo-inverse solution (Figure 4.9a and b), and optimization results (Figure 5.8) can be compared. Notice that the input torques and forces required for the pseudo-inverse solution have as expected the lowest magnitudes, i.e., lower than the non-redundant solutions and the optimization-based (*FMINCON*) results. Note also that the optimization-based (*FMINCON*) results have lower magnitude values for the base and elbow joints than the non-redundant solutions, but have higher values than the pseudo-inverse solutions. These optimization-based (*FMINCON*) higher values, however, achieve backlash-free outputs, i.e., no actuator-output sign-switching. Notice that the optimized circle cutting trajectory with the first two joints per branch

actuated, i.e., Figures 4.3 and 4.4, requires lower peak absolute actuator values then the non-redundant circle cutting trajectories of Chapter 3. This is expected since two joints per branch are actuated for the optimized trajectories in comparison to one joint per branch actuated for the non-redundant actuated trajectories. Also notice that the optimized circle cutting trajectories, i.e., Figures 4.3 and 4.4 require higher peak absolute actuator values than those required to follow the circle cutting trajectory solved with the pseudo-inverse solution illustrated in Figures 4.3a and b. This again is expected since the optimized solution with the first two joints actuated per branch satisfies the constraints of non-reversing actuator values, while the pseudo-inverse solution minimizes the 2-norm of the actuator values and does not satisfy the non-reversing actuator value constraints, i.e., the joint values of Figures 4.3a and b switch sign and are prone to actuator backlash.

If singular configurations are present or if the manipulator passes close to a singular configuration when following a trajectory, changing some of the *ARSs* allows different *ARS* matrices to be constructed that are better conditioned and thus more numerically stable. Column switching for the *ARS* matrix was required for the 3-*RRR PM* cutting the arc trajectory in Section 4.8.3.

In all the results presented in Section 5.2 and 5.3, a sine wave (Section 4.8.1) is used to model the desired wrench intensities. This curve was chosen because of its simplicity in specifying search parameters that assure same sense outputs. With the amplitude defined by a factor less than 1 (see Equation (4-12)), the same sense outputs are guaranteed. Other curves can also be used as long as proper care of the function signs is taken (for example, the arc tangent-based function presented in Section 4.8.1).

Chapter 6

Conclusions and Rrecommendations for Further Research

6.1 Overview of Chapter 6

The Dissertation is summarized in Section 6.2. Main contributions made in the Dissertation are discussed in Section 6.3. Conclusions are made in Section 6.4 and recommedations for future research are discussed in Section 6.5.

6.2 Dissertation Summary

The goal of the research of this Dissertation is the reduction of backlash for *PM*s. During the realization of this goal, problems of non-redundantly and redundantly actuated *PM*s are considered. A novel approach of optimization-based wrench intensity resolutions is involved in the final solution. The paragraphs below summarize the contents of this Dissertation..

In Chapter 1, the goals of the research of this Dissertation are given (Section 1.1), and relevant literature related to backlash reduction is reviewed (Section 1.2). From the literature the observation that configurations where actuator forces switch sign (go to zero) are prone to backlash and related *PM* inacuracies, is made. Geometric parameters of the 3-*RRR* and 3-*RPR PM*s considered in later examples are presented including layouts and dimensions (Section 1.3.2). Actuated joint limits and *PM* working areas are considered. A working area determination method for *PM*s with rotated payload platforms is made in Section 1.3.3. The method is based on inverting the motion, rotating the base platform in the opposite sense to payload platform's rotation. Working areas for the 3-*RRR* and 3-*RPR PM*s are found. Chapter 1 ends with a summary (Section 1.4) of the material considered in later Chapters of the Dissertation.

Chapter 2 considers the inverse static force problem of solving for required actuated joint forces (torques for actuated revolute joints, forces for actuated prismatic joints). The example 3-*RRR* and 3-*RPR PM*s' base and payload platform frames of reference are discussed in Section 2.2. Expressing force problems with associated reciprocal screws (*ARS*s), wrench intensities and reciprocal products is considered in Section 2.3. The properties of reciprocal screw quantities are discussed in Section 2.4. Static force problems for the 3-*RRR*, 3-*RRR*, 3-*RPR*, and 3-*RPR PM*s are considered in terms of *ARS*s, wrench intensities and reciprocal products in Section 2.5. A discussion of the contributions of Chapter 2 is contained in Section 2.6. Within Section 2.6 is a proof of the invariance of a reciprocal product to changes in reference frame location and orientation.

In Chapter 3, circle (sub-Section 3.2.2), logarithmic spiral (sub-Section 3.2.3), and arc (sub-Section 3.2.4), force trajectories are derived for cutting operations. For the arc trajectory it is observed that the involved 3-*RRR PM*'s actuated joints come close to a planar pencil (Hunt 1978) screw system. A planar pencil has a screw system order of two (equivalent to a matrix representation rank of two), and involves screws lying in a common plane and having a common intersection point. Three or more screws forming a planar pencil are degenerative.

Feasibility of the trajectories and the *PM* working areas are considered in sub-Section 3.3.1, with all of the trajectories lying within the working area of the 3-*RRR PM* but none of the trajectories lying within the working area of the 3-*RPR PM*. The joint limits on the prismatic joints, i.e., lengths between 0.3*m* and 0.6*m*, are the reason for the trajectories lying outside of the working area of the 3-*RPR PM*. The unconstrained stacked revolute joints of the 3-*RRR PM* allowed a larger, trajectory-compatible, working area. The prismatic joints are redesigned within sub-Section 3.3.2 to allow length limits between 0 and 0.6*m*, and a trajectory compatible working area equivalent to the 3-*RRR PM* working area.

Unconstrained configurations of the non-redundantly actuated 3-*RPR PM* are considered in sub-Section 3.4. Non-redundant usual actuations of the 3-*RPR PM*s are considered in sub-Section 3.4.1. Analytical input and output velocity equations are discussed in Section 3.4.2 to derive the equations required to generate the Jacobian matrices whose rank deficiency is associated with *PM* uncertainty configurations. In an alternative to finding Jacobian matrix rank deficiency it is demonstrated in Section 3.4.3

that payload platform edges centrally located and oriented parallel with their corresponding base edges are uncertain force configurations. The payload platform and base edge uncertain force configurations do not allow the application of arbitrary moments about the related concurrency point (centre of the rank 2 (rank deficient) planar pencil formed from 3 *ARS*s). These uncertainty configurations are singular for solutions involving the inversion of *ARS* matrices. Stability of the payload platform is demonstrated in Section 3.4.4.

Inverse static force solutions are found for the actuated joints of the non-redundantly-actuated 3-*RRR PM* (sub-Section 3.5.2), 3-*RRR PM* (sub-Section 3.5.3), 3-*RPR PM* (sub-Section 3.5.4), and 3-*RPR PMs* (sub-Section 3.5.5) executing the circle, spiral and arc cutting trajectories. The non-redundantly actuated *PM*s are observed to have two backlash-prone configurations for the actuated joint-ouputs, where the actuated joint-outputs switch sign (go to zero). This is observed to happen for all three of the introduced trajectories (a full-cirle arc trajectory is considered in Section 3.6.5 to demonstrate the existance of two backlash-prone locations for the arc trajectory). Section 3.6 is a discussion of the contributions made in Chapter 3.

Within Chapter 4, static force problems for redundantly-actuated *PM*s are expressed in terms of *ARS*s, wrench intensities and reciprocal products in Section 4.2. Static force solutions for redundantly-actuated *PM*s based on pseudo (right Moore-Penrose) inversion of the *ARS*s matrix are solved in Section 4.3. The pseudo-inverse solutions of Section 4.3 are done for the circle, spiral, and arc trajectories for both the 3-*RRR* and the 3-*RPR PM*s. While minimizing the 2-norm (Strang 1988) of the required actuated joint forces, the

pseudo-inverse solutions did not reduce backlash, i.e., they involved zero-actuated joint forces. Therefore, pseudo-inverse solutions in this Dissertation are only considered as potential particular solutions.

A method of creating null-space basis vectors for the matrix of *ARS*s based on resolving redundant joint forces back onto joint forces selected as non-redundant is presented in Section 4.4. In Section 4.5 general wrench intensity solutions are expressed in terms of a particular solution and a homogeneous solution formed from the null-space basis vectors presented in Section 4.4.

Branch 2nd joint wrench intensity values to ensure specific (including non-reversing) 1st joint intensity values are presented in Section 4.6. An optimization-based algorithm for reducing backlash using the *MATLAB* program *FMINCON* is presented in Section 4.7. Routines including: non-reversing 1st joint wrench intensity values based on a sinusoidal function; and same sign constraints to allow the implementation of *FMINCON* are discussed in Section 4.8. Section 4.9 is a discussion presenting alternative non-reversing 1st joint wrench intensity values based on an inverse tangent function and highlighting contributions of Chapter 4.

Chapter 5 considers using optimization-based (*FMINCON*) solutions to find backlash-free wrench intensity results for redundantly-actuated *PM*s performing the circle, spiral and arc force trajectories. The use of optimization-based solutions to find backlash-free wrench intensity results is a novel contribution 5. Optimization-based (*FMINCON*) backlash-free solutions are presented for the 3-*RRR PM* for the circle (sub-Section 5.2.2), spiral (sub-Section 5.2.3) and the arc (sub-Section 5.2.4) trajectories. Again, with the arc

trajectory the *ARS*s of the base revolute joints are used to form a particular wrench intensity solution and a degenerative planar pencil (Hunt 1978) is approached. With redundant joints, however, selecting an *ARS* yielding a well-conditioned *ARS* matrix is recommended and implemented yielding a well-conditioned particular solution.

Optimization-based (*FMINCON*) backlash-free solutions are presented for the 3-*RPR PM* for the circle (sub-Section 5.3.2), spiral (sub-Section 5.3.3) and the arc (sub-Section 5.3.4) trajectories. Section 5.4 is a discussion highlighting the contributions of Chapter 5.

6.3 Contributions

The following novel contributions were made in this thesis:

1) A proof of the invariance of a reciprocal product to changes in reference frame location and orientation.(Se4ction 2.6.3).
2) Derivation of null-space basis vectors for the ARS matrix ${}^{B}\$'_{6}$ based on decomposing 2nd joint (elbow *R* for 3-*RRR* or prismatic *P* joint for 3- *RPR PM*s) screw coordinates, back onto the first join screw coordinates. (Section 4.4).
3) A design modification of the prismatic joints to allow length limits between 0 and 0.6m, and a trajectory compatible working area equivalent to the 3-RRR PM working area. (Section 3.3).
4) Demonstration of force uncertain configurations, due to platform and base edge alignment. (Section 3.4).

5) The algorithm to use FMINCON for ensuring reduced backlash, the non-reversing functions to ensure non-reversing first joint wrench intensities, and the constraints to ensure non-reversing second joint values (Sections 4.7 and 4.8, and Chapter 5).

6.4 Conclusions

Based on the results of this Dissertation, the following conclusions can be made:

1) Working areas for *PM*s with rotated payload platforms can be found by considering an inversion, rotating the base platform in the opposite direction to the rotation of the payload platform (Section 1.3).
2) Using screw coordinates and reciprocal products is a preferred way to solve *PM* static force problems since the reciprocal product is invariant of reference frame orientation and origin location (sub-Section 2.5.3).
3) 3-*R*<u>*P*</u>*R PM*s whose payload platform edges are centrally located and oriented parallel with their corresponding base edges are in uncertainty configurations (Section 3.4). The above conclusion is demonstrated by showing that the constraint forces provided by the actuated prismatic joints form a degenerative planar pencil (a 2-system (Hunt 1978)).
4) $3*O(\infty^1) = O(\infty^1)$ 3-*R*<u>*P*</u>*R PM* (rank-deficient) uncertainty configurations due to payload platform edges being centrally located and oriented parallel with corresponding base edges exist. In these edge-aligned configurations the constraint forces form a rank deficient planar pencil. (Section 3.4.3).

5) For a task to be repeatible its displacement and force trajectories trajectories must be cyclic, i.e., start and end with the same values (Section 5.2.3 and 5.4.1).
6) Non-redundantly actuated manipulators when executing the example circle, spiral and arc force trajectories exhibited two backlash-prone locations having actuator output sign-switching. This makes non-redundantly actuated *PM*s unsuitable for high-precision applications. (Section 3.5).
7) Backlash reduction for redundantly-actuated *PM*s cannot be achieved using Moore-Penrose pseudo-inverses of the *ARS* matrix of the *PM* (Section 4.3). The Moore-Penrose pseudo-inverse solution provides the minimum 2-norm of wrench intensities, but is not meant to provide backlash-free motion.
8) Reduction of backlash is possible for redundantly actuated *PM*s using non-linear optimization (*FMINCON*) and non-reversing actuator output constraints (Sections 5.2 and 5.3). The above conclusions are demonstrated for 3-*RRR* and 3-*RPR* *PM*s executing practical circle, spiral, and arc trajectories intended for cutting.

6.5 Recommendations for Future Research

a) The effect of actuator preloading on the inaccuracy caused by joint clearances discussed in Section 1.2.3 should be investigated.
b) The uncertainties found by Firmani and Podhorodeski (2009) using analytical input and output velocity equations should be verified utilizing the platform and base-edge alignment results found in Section 3.4 using kinematic geometry.

c) Within this Dissertation ensuring that $\tau \geq 0$ or $\tau \leq 0$ where τ is an indivdual actuation force (torque or force depending on joint type) are used to reduce backlash. This process is repeated for all actuated joints. The mininum absolute τ value could be defined to be a finite value, i.e., $\left| \tau \right| \geq \tau_{finite}$ or $\left| \tau \right| \leq \tau_{finite}$., The reason for this future research recommondation is to use further actuated joint preloading to ensure finite actuation outputs by placing the *PM* futher from configurations having backlash (Sections 4.9.6).

d) A very promising contribution to backlash reduction is the use of passive spring torques to pre-load wrist joints for 3-*PRR PM*s (where the enlarged underlined *R* indicates the passive spring preloading) has been made recently by Wei and Simaan (2010). Passive spring actuation and required spring preloading should be investigated for 3-*RRR*, 3-*RRR*, 3-*RPR* and 3-*RPR PM*s. The level of preloading required for the tasks of this Dissertation need to be determined.

e) The effect of preloading of the base or elbow joints and actuating the elbow or base or wrist should be considered. Potential actuation layouts include: 3- *RRR*, *3-RRR*, 3-*RRR*, 3-*RRR*, 3-*RPR*, 3-*RPR*, 3-*RPR*, 3-*PRR*, 3-*PRR*, 3-*PRR*, and 3-*PRR*.

References

Ball, R.S. (1900), *Theory of Screws: A Treatise on the Theory of Screws*, Cambridge University Press, New York, NY, USA, 1900.

Bicchi, A., Melchiorri, C., and Balluchib, D. (1995), "On the Mobility and Manipulability of General Multiple Limb Robots*," IEEE Transactions on Robotics and Automation*, **11**, pp. 215-228, April 1995.

Bonev, I.A., Zlatanov, D., and Gossdelin, C.M. (2003), "Singularity Analysis of 3-*DOF* Planar Parallel Manipulators via Screw Theory," *Transactions of ASME Journal of Mechanical Design*, **125**(3), pp. 573-581, 2003.

Boudreau, R., Mao, X., and Podhorodeski, R.P. (2012), "Backlash Reduction in Parallel Manipulators using Actuation Redundancy," published online: July 11, 2011, to *Robotica*, **30**(3), pp. 379-388, 2012.

Briot, S., and Bonev, I.A. (2008), "Accuracy Analysis of 3-*DOF* Planar Parallel Robots," *Mechanism and Machine Theory*, **43**, 445-458, 2008.

Carretero, J.A., Podhorodeski, R.P., Nahon, M. and Gosselin, C.M. (2000a), "Kinematic Analysis and Optimization of a New Three-Degree-of-Freedom Spatial Parallel Manipulator," *ASME Transactions, Journal of Mechanical Design*, **122**(1), pp..17-24, 2000a.

Carretero, J.A., Nahon, M. and Podhorodeski, R.P. (2000b), "Workspace Analysis and Optimization of a Novel 3-*DOF* Parallel Manipulator*," International Journal of Robotics and Automation*, **15**(4), pp. 178-188, 2000b.

Chebbi, A.- H., Affi, Z., and Romdhane, L. (2009), "Prediction of the Pose Errors Produced by Joint Clearance for the 3-UPU Parallel Robot," *Mechanism and Machine Theory*, **44**(9), pp. 1768-1783, 2009.

Chiacchio, P., Chiaverni, S. and Siciliano, B. (1991), "Global Task Space Manipulability Ellipsoids for Multiple-arm Systems," *IEEE Transactions on Robotics and Automation*, **7**, pp. 678-685, October 1991.

Collins, C.L., and McCarthy, J. M. (1998), "The Quartic Singularity Surfaces of Planar Platforms in the Clifford Algebra of the Projective Plane*," Mechanism and Machine Theory* **33**(7), pp. 931-944, 1998.

Craig, J.J. (2005), "Introduction to Robotics" *Mechanics and Control*, *3rd Edition*, Pearson Prentice Hall, Upper Saddle River, NJ, USA, 2005.

Ebrahimi, I, Carretero, J.A., and Boudreau, R. (2007), "3-*PRRR* Redundant Planar Parallel Manipulator: Inverse Displacement, Workspace and Singularity Analysis," *Mechanism and Machine Theory*, **42**(8), pp. 1007-1016, 2007.

Erdman, A. G. and Sandor, G. N. (1996), "*Mechanism Design: Analysis and Synthesis,* " vol. 1, Prentice Hall College Div, 1996

Firmani, F. and Podhorodeski, R. P. (2004), "Force-unconstrained Poses for a Redundantly-Actuated Planar Parallel Manipulator," *Mechanism and Machine Theory*, **39**(5), pp. 459-476, 2004.

Firmani, F., Zibil, A., Nokleby, S. B., and Podhorodeski, R. P. (2007), "Force-Moment Capabilities of Revolute-Jointed Planar Parallel Manipulators with Additional Actuated Branches," *CSME Transactions*, **31**(4), pp. 469-481, 2007.

Firmani, F., and Podhorodeski, R. P. (2009), "Singularity Analysis of Planar Parallel Manipulators based on Forward Kinematic Solutions," *Mechanism and Machine Theory*, **44**, pp. 1386-1399, 2009.

Gosselin, C. M. (1988), "Kinematic Analysis, Optimization and Programming of Parallel Robotic Manipulators," *Ph.D. Dissertation*, McGill University, 1988.

Gosselin, C.M., and Angeles, J. (1988), "The Optimum Kinematic Design of a Planar Three-Degree-of-Freedom Parallel Manipulator," *ASME Journal of Mechanisms, Transmissions, and Automation in Design*, **110**(1), pp. 35-41, 1988.

Gosselin, C.M., and Angeles, J. (1990), "Singularity Analysis of Closed-loop Kinematic Chains," *IEEE Transactions on Robotics and Automation*, **6**(3), pp. 281-290, 1990.

Gosselin, C.M. (1990), "Determination of the Workspace of 6-*DOF* Parallel Manipulators," *ASME Journal of Mechanical Design*, **112**(3), pp. 331-336, 1990.

Gosselin. C.M., Sefrioui, J, and Richards, M. J. (1992), "Solutions Polynomiales au Probleme de la Cinematique Directe des Manipulateurs, Paralleles Plans a Trois Degres de Liberte: polynomial solutions to the direct kinemastic problem of three degree-of-freedom parallel manipulators,*" Mechanism and Machine Theory*, **27**(2), pp. 107-119, 1992.

Gosselin, C.M., and Jean, M. (1996), "Determination of the Workspace of Planar Parallel Manipulators with Joint Limits," *Robotics and Autonomous Systems*, **17**, pp. 129-138, 1996.

Gosselin, C.M., Lemieux,S., and Merlet, J. P. (1996), *"*A New Architecture of Planar Three-Degree-of-Freedom Parallel Manipulator," *IEEE International Conference on Robotics and Automation*, **4**, pp. 3738-3743, 1996.

Gough, V. E. (1965), "Communication Comment, on "A Platform with Six Degrees of Freedom" by D. Stewart," Proceedings of *the Institution of Mechanical Engineers,* **180**(1)**,** pp. 379-381, 1965**.**

Hayes, M.J.D., and Husty, M.L. (2003), "On the Kinematic Constraint Surfaces of General Three-Legged Planar Robot Platforms," *Mechanism and Machine Theory*, **43**, pp. 379-394, 2003.

Hunt, K.H. ((1978), "Kinematic Geometry of Mechanisms," *Oxford University Press*, Toronto, ON, Canada, 1978.

Hunt, K.H (1983), "Structural Kinematics of in-parallel Actuated Robot Arms," *ASME Journal of Mechanisms Transmissions and Automation* in *Design,* **105**(4). pp. 705-712, 1983.

Innocenti, C. (2002), "Kinematic Clearance Sensitivity Analysis of Spatial Structures with Revolute Joints," *ASME Journal of Mechanical Design*, **124**(1), pp. 52-57, 2002.

Kang, B.H., Wen, J.T.-Y., Dagalakis, N.G., and Gorman, J. J. (2005), "Analysis and Design of Parallel Mechanisms With Flexure Joints," *IEEE Transactions on Robotics*, **21**(6), pp. 1179-1184, 2005.

Kazerounian, K., and Wang, Z. (1988), "Global versus Local Optimization in Redundancy Resolution of Robotic Manipulators," I*nternational Journal of Robotics Research*, **7**(5), pp. 3-12, 1988.

Khatib, O. (1983), "Dynamic Control of Manipulators in Operational Space," *6th World Congress on the Theory of Machines and Mechanisms*, pp. 1128-1131, 1983.

Kircanski, M., and Vukobratovic, M. (1984), "A Dynamic Approach to Nominal Trajectory Synthesis for Redundant Manipulators," *IEEE Transactions on Systems, Man, and Cybernetics*, Vol. SMC-**14**(4), pp. 580-586, 1984.

Klein, C.A. (1985), "Use of Redundancy in the Design of Robotic Systems", Proceedings of *the 2nd International Symposium on Robotics Research*, pp. 207-214, 1985.

Kotlarski, J., Trung, D. T., Heimann, B., and Ortmaier, T. (2010), "Optimization Strategies for Additional Actuators of Kinematically Redundant Parallel Kinematic Machines," *2010 IEEE International Conference on Robotics and Automation*, Anchorage, Alaska, pp. 656-661, 2010.

Lequay-Durand, S., and Reboulet, C. (1997), "Optimal Design of a Redundant Spherical Parallel Manipulator," *Robotica*, **15**(4), pp. 399-405, 1997.

Li, H., Gosselin, C. M., and Richard, M. J. (2006), "Determination of Maximal Singularity-free Zones in the Work-Space of Planar three-degree-of-freedom Parallel Mechanisms," *Mechanism and Machine Theory*, **41**(15), pp. 1157 – 1167, 2006.

Lotfi, B., Zhong, Z.W., and Khoo, L. P. (2010), "A Novel Algorithm to Generate Backlash-free Motions, *Mechanism and Machine Theory*, **45**, pp. 1171-1184, 2010.

Mao, X., and Podhorodeski, R. P. (2010), "Using Actuation Redundancy to Eliminate Backlash in Parallel Manipulators," Proceedings of *the CMSE 2010 Forum*, June 7-9, 2010, Victoria, BC, 5 pages, 2010.

Mao, X., and Podhorodeski, R. P. (2012), "Backlash Reduction in 3-*RPR* Parallel Manipulators," in preparation for Submission. 2012, to *Robotica*.

Merlet, J.P. (1989), "Singular Configurations of Parallel Manipulators and Grassmann Geometry," *International Journal Robotics Research*, **8**(5), pp. 45-56, 1989.

Merlet, J.P. (1993), "Parallel Manipulators: State of Art and Perspective," in *Robotics, Mechatronics, and Manufacturing Systems*, Elsevier, 1993.

Merlet, J.P. (1996a), "Direct Kinematics of Planar Parallel Manipulators," *IEEE International Conference on Robotics and Automation*, **4**, pp. 3744-3749, 1996a.

Merlet, J.P. (1996b), "Redundant Parallel Manipulators," *Journal of Laboratory Robotics and Automation*, **8**, pp. 17-24, 1996b.

Mohammadi-Daniali, H.R., Zsombor-Murray, P.J., and Angeles, J. (1995), "Singularity analysis of planar parallel manipulators," *Mechanism and Machine Theory*, **30**(5), pp. 665-678, 1995.

Müller, A. (2005), "Internal Preload Control of Redundantly Actuated Parallel Manipulators – Its Application to Backlash Avoiding Control," *IEEE Transactions on Robotics*, **21**(4), pp. 668-677, 2005.

Müller, A. and Maisser, P. (2007), "Generation and Application of Prestress in Redundantly Full-actuated Parallel Manipulators," *Multibody System Dynamics*, **18**(2), pp. 259-275, 2007.

Müller, A. (2010), "Consequences of Geometric Imperfections for the Control of Redundantly Actuated Parallel Manipulators," *IEEE Transactions on Robotics*, **26**(1), 2010.

Müller, A. (2011), "Problems in the Control of Redundantly Actuated Parallel Manipulators Caused by Geometric Imperfections," *Meccanica*, **46**, pp. 41-49, 2011.

Müller, A. and Hufnagel, T. (2012), "Robotics and Autonomous Systems," *Robotics and Autonomous Systems*, **60**, pp. 563-567, 2012.

Nakumura, Y., and Hanafusa, H. (1987), "Optimal Redundancy Control of Robot Manipulators," *International Journal of Robotics Research*, **6**(1), pp. 32-42, 1987.

O'Brien, J. F., Jafari, F., and Wen, J. T. (2006), "Determination of Unstable Singularities in Parallel Robots with N-arms," *IEEE Transactions on Robotics*, **22**(1), pp. 160 – 168, 2006.

Parenti-Castelli, V. and Venanzi, S. (2005), "Clearance Influence Analysis on Mechanisms," *Mechanism and Machine Theory*, **40**(12), pp. 1316-1329, 2005.

Pashkevich, A., Klimchik, A., and Chablat, D. (2011), "Enhanced Stiffness Modeling of Manipulators with Passive Joints," *Mechanism and Machine Theory*, **46**(5), pp. 662-679, 2011.

Pham, H.H. and Chen, I. M. (2004), "Optimal Synthesis for Workspace and Manipulability of Parallel Flexure Mechanism," *11th World Congress in Mechanism and Machine Science*, Tianjin, China, 5 pages, 2004.

Pieper, D., and Roth, B. (1969), "The Kinematics of Manipulators Under Computer Control," In Proceedings of *the Second World Congress on the Theory of Machines and Mechanisms*, Journal of Materials Processing Technology. **140**, pp. 100-104, 1969.

Pinto, C., Corral, J., Altuzaria, O., and Hernandez, A. (2010), "A Methodology for Static Mapping in Lower Mobility Parallel Manipulators with Decoupled Motions," *Robotica*, **20**, pp. 719-735, 2010.

Podhorodeski, R.P. (1989), "New Approaches for the Solution of Inverse Instantaneous Kinematic Problems and of Contact Forces in Multiple Contact Grasping, " *Ph.D. Dissertation*. University of Toronto, 1989.

Podhorodeski, R.P., Goldenberg, A.A., and Fenton, R. G. (1991), "Resolving Redundant Manipulator Joint Rates and Identifying Special Arm Configurations using Jacobin Null-space Bases," *IEEE Transactions on Robotics and Automation*, **7**(5), pp. 607-618, 1991.

Podhorodeski, R.P., Goldenberg, A.A., and Fenton, R. G. (1993), "A Null-Space Solution of the Inverse Kinematics of Redundant Manipulators Based on a

Decomposition of Screws," *ASME Journal of Mechanical Design*, **115**(3), pp. 530-539, 1993.

Roth, B. (1984), "Screw, Motors, and Wrenches that Cannot be Bought in a Hardware Store," Proceedings of *the 1st International Symposium on Robotics Research*, pp. 679-693, 1984.

Ryu, C. J., Kim, J. W., Hwang, J.C., Park, C.B., Cao, H.S., Kiha Lee, Y.H., Lee, U.C., Park, F.C., and Kim, J. W. (1998), "ECLIPSE: An Overactuated Parallel Mechanism for Rapid Machining," *ASME International Mechanical Engineering Congress and Exposition*, **11**, pp. 1–11, 1998.

Stewart, D. (1965a), "A Platform with Six Degrees of Freedom," Proceedings of *the Institution of Mechanical Engineers*, **180**(1), pp. 371-378, 1965a.

Stewart, D. (1965b), "Author's Reply to Gough's Comment on "Platform with Six Degrees of Freedom," Proceedings of *the Institution of Mechanical Engineers*, **180(1)**, pp. 386, 1965b.

Strang, G. (1988), Linear Algebra and its Applications, *2nd Edition*, Harcourt Brace, Orlando, FL, USA, 1988.

Suh, K.C., and Hollerbach, J. M. (1987)., "Local versus Global Torque Optimization of Redundant Manipulators," Proceedings of *1987 IEEE International Conference on Robotics and Automation*, pp. 619-624, 1987.

Wei, W., and Simaan, N. (2010), "Design of Planar Parallel Robots With Preloaded Flexures for Guaranteed Backlash Prevention," *ASME Journal of Mechanisms and Robotics*, **2**(1), pp. 1-10, 2010.

Weihmann, L., Martins, D., and Dos Santos Coelho, L. (2012), "Modified Differential Evolution Approach for Optimization of Planar Parallel Manipulators Force Capabilities," *Expert Systems with Applications*, **39**, pp. 6150-6156, 2012.

Whitney, D.E. (1969), "Resolved Motion Rate Control of Manipulators and Human Prothesis," *IEEE Transactions on Man-Machine Systems*, Vol. MMS-10, pp. 47-53, 1969.

Whitney, D.E. (1972), "The Mathematics of Coordinates Control of Prothetic Arms and Manipulators," *IEEE Transactions on Systems, Man, and Cybernetics*, **94**, pp. 303-309, 1972.

Williams II, R.L., and Reinholtz, C. F. (1988), "Closed-Form Workspace Determination and Optimization for Parallel Robot Mechanisms," *20th Biennial ASME Mechanisms Conference*, **15**(3), pp. 341-351, 1988.

Williams II, R.L., and Joshi, A.R. (1999), "Planar Parallel 3-RPR Manipulator," *6th Conference on Applied Mechanisms and Robotics*, Cincinnati, OH, pp. 1 - 8, 1999.

Wu, J., Wang, J., Wang, L., and Li, T. (2009), "Dynamics and Control of a Planar 3-*DOF* Parallel Manipulator with Actuation Redundancy," *Mechanism and Machine Theory*, **44**, pp. 835-849, 2009.

Xu, Y., Yao, J., and Zhao, Y. (2012), "Inverse Dynamics and Internal Forces of the Redundantly Actuated Parallel Manipulators," *Mechanism and Machine Theory*, **51**, pp. 172-184, 2012.

Yang, Y., and O'Brien, J.F. (2007), "A Case Study of Planar 3-RPR Parallel Robot Singularity Free Workspace Design," *2007 IEEE International Conference on Mechatronics and Automation*, Harbin, China, pp. 1834-1838, 2007.

Yi, B.-J., Chung, G. B., Na, H.Y., Kim, W.K., and Suh, I. H. (2003), "Design and Experiment of a 3-*DOF* Parallel Micromechanism Utilizing Flexure Hinges," *IEEE Transactions on Robotics and Automation*, **19**(4), pp. 604-612, 2003.

Yosikawa, T. (1985), "Manipulability and Redundancy Control of Robotic Mechanisms," *IEEE International Conference on Robotics and Automation*, pp. 1004-1009, 1985.

Zanganeh, K.E., and Angeles, J. (1997), "Kinematic Isotropy and the Optimal Design of Parallel Manipulators," *The International Journal of Robotics Research*, **16**(2), pp. 185-197, 1997.

Zhang, J., Yu, H., Gao, F., and Zhao, X. (2011), "Key Issues in Studying Parallel Manipulators," Proceedings of *International Conference on Advanced Mechatronics Systems*, pp. 234-244, 2011.

Zhang, D., Xu, Z., Mechefske, C.M., and Xi, F. (2004), "Optimum Design of Parallel Kinematic Toolheads with Genetic Algorithms," *Robotica*, **22**, pp 77-84, 2004.

Zibil, A., Firmani, F., Nokleby, S.B., and Podhorodeski, R. P. (2007), "An Explicit Method for Determining the Force-Moment Capabilities of Redundantly-Actuated Planar Parallel Manipulators," *ASME Journal of Mechanical Design*, **129**(10), pp. 1046-1055, 2007.

Appendix A

FDS for the *RRR* and *RPR* Branch Types

A.1 Overview

The forward displacement solution *(FDS*) finds locations and orientations of the *PM* payload platform (and end-effector) for known actuated joint displacements. Within Appendix A, *FDS*s are found for the *RRR* and *RPR* branch types and three branch *PM*s. Wrist locations in terms of the branch parameters and joint displacements are presented in Section A.2. The *FDS* for three-branch *PM*s is discussed in Section A.3. Inverse displacement solutions (*IDS*s) are presented in Appendix B.

A.2 Wrist Locations in Terms of Branch Parameters and Joint Displacements

The locations of the base joints, x_{1i} and y_{1i}, i = 1 to *b*, are given by:

$$x_{1i} = l_B \cos((i-1)(2\pi/b) - \pi/(2b)), \tag{A-1a}$$

$$y_{1i} = l_B \sin((i-1)(2\pi/b) - \pi/(2b)), \quad i = 1, 2, \ldots b. \tag{A-1b}$$

For b = 3:

$$x_{1i} = l_B \cos((i-1)(\frac{2\pi}{3} - \pi/6)), \tag{A-2a}$$

$$y_{1i} = l_B \sin((i-1)(2\pi/3) - \pi/6), \quad i = 1, 2, \text{ and } 3. \tag{A-2b}$$

Equations (A-2) are true for both the 3-*RRR PM* and for the 3-*RPR PM*. Equations (A-1) could be rewritten as: $x_{1i} = l_B\cos(\gamma_i)$ and $y_{1i} = l_B\sin(\gamma_i)$ where:

$$\gamma_i = (i-1)(2\pi/b) - \pi/(2b). \tag{A-3}$$

The base pin spacing is illustrated if values of γ_i are considered for different values of *b* (different numbers of branches,) i.e.:

$$b = 3: \gamma_1 = -\frac{\pi}{6};\ \gamma_i = \frac{\pi}{2};\ \gamma_3 = \frac{7\pi}{6};\gamma_4 = 2\pi - \frac{\pi}{6} = -\frac{\pi}{6},$$

$$b = 4: \alpha_1 = -\frac{\pi}{8}; \alpha_2 = -\frac{3\pi}{8}; \alpha_3 = -\frac{7\pi}{8}; \alpha_4 = -\frac{11\pi}{8}; \alpha_5 = 2\pi - \frac{\pi}{8} = -\frac{\pi}{8},$$

$$b = 6: \gamma_1 = -\frac{\pi}{12};\ \gamma_2 = \frac{3\pi}{12};\ \gamma_3 = \frac{7\pi}{12};\gamma_4 = \frac{11\pi}{12};\gamma_5 = \frac{15\pi}{12}, \gamma_6 = \frac{19\pi}{12};\gamma_7 = 2\pi - \frac{\pi}{12} = -\pi/12$$

(A-4)

The value for $\gamma_{(b+1)}$ (i.e., γ_4 for $b = 3$) was calculated to ensure that the γ_i of Equation (A-3) is cyclic.

For the 3-*RRR PM*, the wrist locations, x_{3i} and y_{3i}, i = 1 to 3, in terms of branch parameters and joint displacements can be found by inspection to be:

$$x_{3i} = x_{1i} + l_1 \cos q_{1i} + l_1 \cos(q_{1i} + q_{2i}), \quad \text{(A-5a)}$$

$$y_{3i} = y_{1i} + l_1 \sin q_{1i} + l_2 \sin(q_{1i} + q_{2i}), \quad i = 1, 2, \text{ and } 3, \quad \text{(A-5b)}$$

where l_1 and l_2 are the fixed lengthes of the 1st and 2nd links of each branch, and q_{1i} and q_{2i} are the displacements of the 1st and 2nd joints of branch i.

For the 3-*RPR PM*, the wrist locations, x_{3i} and y_{3i}, i = 1 to 3, in terms of branch parameters and joint displacements can be found by inspection to be:

$$x_{3i} = x_{1i} + q_{2i} \cos(q_{1i}), \quad \text{(A-6a)}$$

$$y_{3i} = y_{1i} + q_{2i} \sin(q_{1i}), \quad i = 1, 2, \text{ and } 3, \quad \text{(A-6b)}$$

where q_{2i} is the length of the ith prismatic joint and q_{1i} is the angle at the 1st joint of the ith branch, i.e., the angle of the prismatic joint.

Equations (A-2a) and (A-2b) and Equations (A-5a) and (A-5b) are the *FDS*s for the 3-*RRR PM*. Equations (A-2a) and (A-2b) and Equations (A-6a) and (A-6b) are the *FDS*s for the 3-*RPR PM*.

A.3 *FDS* for 3-Branch *PM*s

For non-redundant actuation (and joint displacement encoding), i.e., only one joint per branch sensed, solution the *FDS* of a *PM* can be done with tangent ½ angle (Craig (2005)) substitution. Gosselin *et al*. (1992) expresssed the *FDS* solutions of the 3-*RPR* and the 3-*RRR PM*s as the roots of a 6th order polynomial of a single variable. Merlet

(1996) confirmed that the *FDS* for 3-*RRR PM*s can be expressed in terms of the roots to a 6^{th} order polynomial of a single variable and demonstrated that the *FDS* of 3-*RPR* and 3-*PRR PM*s can be expressed in terms of the roots of quadratics.

The solutions of Gosselin *et al*. (1992) and Merlet (1996) show that *PM*s can have several different assembly modes (*FDS*s). For example, a 3-*RRR* manipulator can have up to 6 assembly modes (*FDS*s). Switching between assembly modes becomes possible in force unconstrained configurations. This is a serious disadvantage of non-redundant *PM* joint-displacement-encoding since false assembly-mode switching can lead to *PM*s being dangerously controlled on an incorrect assembly mode (i.e., it would not follow the desired end-effector trajectory and would not apply the correct force.)

For the redundant joint displacement encoding considered in this research, both main-arm joint displacements are known. This allows the locations of all three wrists to be found from Equations (A-5) for 3-RRR *PMs* and Equations (A-6) for 3-*RPR PM*s. The location of the payload platform centre can be found by averaging the locations of the three wrist locations, i.e.,

$$x_P = (x_{31} + x_{32} + x_{33})/3, \tag{A-7a}$$

$$y_P = (x_{31} + x_{32} + x_{33})/3, \tag{A-7b}$$

where x_{3i} and y_{3i} are calculated from Equations (A-5a) and (A-5b) for the 3-*RRR PM* and from Equations (A-6a) and (A-6b) for the 3-*RPR PM*. A vector in the payload platforms X-direction, expressed in terms of the *PM*'s base orientation is found by subtracting the location of the third branch's wrist location ${}^0x_{33} = {}^0\{x_{33}, y_{33}\}^T$ from the first branch's wrist location ${}^0x_{31} = {}^0\{x_{31}, y_{31}\}^T$, i.e.,

$$^{o}x_{p} = {}^{o}x_{31} - {}^{o}x_{33} = {}^{0}\{x_{31} - x_{33}, y_{31} - y_{33}\}^{T}. \quad \text{(A-8)}$$

The platforms orientation in terms of the compoments of the platforms X-direction can be expressed as a quadrant corrected arc tangent function:

$$\emptyset = a\tan 2(y_{31} - y_{33}, x_{31} - x_{33}). \quad \text{(A-9)}$$

Equations (A-8) and (A-9) are the *FDS* for a 3-branch *PM* with symmetric redundant joint-displacement-encoding, i.e., the 1st and 2nd joint of each branch encoded.

Appendix B

IDS for the *RRR* and *RPR* Branch Types

B.1 Overview

The inverse displacement solutions (*IDS*s), screw coordinates, and *ARS* coordinates of a *PM* are required to be found in order to propose algorithms for the reduction of backlash. The *IDS* finds joint displacements for a known location and orientation of the *PM*'s end-effector.

The *PM*s analyzed in this work include the 3-*RRR* and the 3-*RPR*. In this Appendix the *IDS*s are analysed for both *PM*s. Section B.2 presents wrist locations in terms of *PM* parameters and the specific task and presents the base locations in terms of *PM* parameters. Section B.3 solves the *IDS*s for the 3-*RRR* and the 3-*RPR PM*s. Appendix C presents the screw coordinates, and the *ARS* coordinates of the *RRR* and *RPR* branch types.

B.2 Inverse Displacement Solutions: Known Values from Branch Parameters and Specified Task, Find Joint Displacements

The *IDS* is required to calculate the screw and the *ARS* coodinates of the joints. In a symmetric planar *PM*, the base and the end-effector of the manipulator are equilateral polygons. Based on the number of the branches (see Figure B-1 for a three-branch example), the positions of the branch wrists can be calculated, i.e., regardless of the brach type, the wrist joint positions of each branch, x_{3i} and y_{3i}, can be found from:

$$x_{3i} = x_p + l_p \cos((i-1)\left(\frac{2\pi}{b}\right) - \pi/b + \emptyset), \quad \text{(B-1a)}$$

$$y_{3i} = y_p + l_p \sin((i-1)\left(\frac{2\pi}{b}\right) - \pi/b + \emptyset), \quad i = 1, 2, \ldots b. \quad \text{(B-1b)}$$

where x_p and y_p are the coordinates of the known task locations, φ is the known task rotation, l_p is the payload platform radius, and b is the number of branches of the *PM* (b = 3 for the considered *PM*s). The base positions of each branch can be found from:

$$x_{1i} = x_B + l_B \cos((i-1)\left(\frac{2\pi}{b}\right) - \pi/b), \quad \text{(B-2a)}$$

$$y_{1i} = y_B + l_B \sin((i-1)\left(\frac{2\pi}{b}\right) - \pi/b), \quad i = 1, 2, \ldots b. \quad \text{(B-2b)}$$

where l_B is the base platform radius.

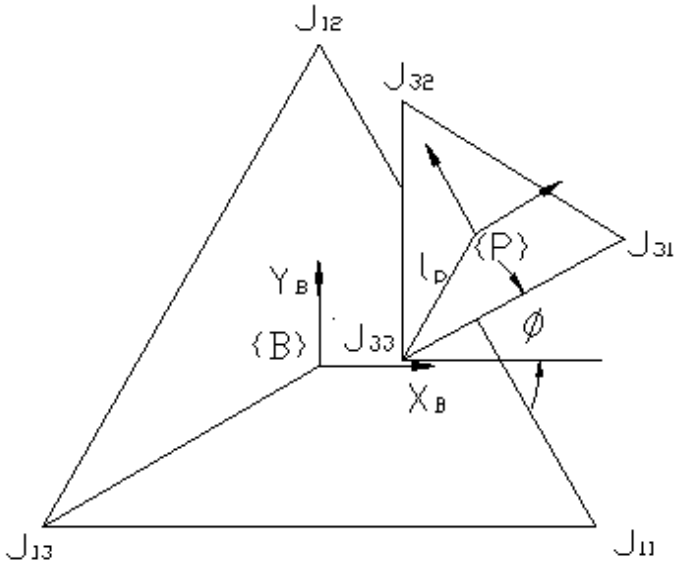

Figure B-1: Base and Platform Geometry of a Three-Branch Planar *PM*.

In Equations (B-1) and (B-2,) b is the number of the branches, i is the branch index with i =1, 2, …, b, and x_{3i} and y_{3i} are the coordinates of the wrist joints. The quantities x_{1i} and y_{1i} are the coordinates of the base joints, x_p and y_p are the coordinates of the centre of the platform, ϕ is the orientation of the platform, and x_B and y_B are the coordinates of the centre of the base. Note that every coordinate has been defined with respect to the base reference frame {B}, a frame located at the centre of the base frame, and oriented such that its X axis points from the first joint of the third branch J_{13} to the first joint of the first branch J_{11}, and the Y axis points to the first joint of the second branch J_{12} as shown in Figure B-1. The rest of the *IDS* problem is specific to each branch type and will be presented in sub-Section B.3 for the 3-*RRR PM* and B.4 for the 3-*RPR PM*.

B.3.1 *IDS* of a 3-*RRR PM*

A *RRR* type branch is shown in Figure B-2. Forward displacement equations of a *RRR* type branch and the joint angles of a 3-*RRR PM* can be written as:

$$x_{3i} = x_{1i} + l_{1i}\cos(q_{1i}) + l_{2i}\cos(q_{1i} + q_{2i}), \quad \text{(B-3a)}$$

$$y_{3i} = y_{1i} + l_{1i}\sin(q_{1i}) + l_{2i}\sin(q_{1i} + q_{2i}), \quad \text{(B-3b)}$$

$$\emptyset = q_{1i} + q_{2i} + q_{3i} - (2\pi(i-1))/b. \quad \text{(B-3c)}$$

where l_{1i} and l_{2i} are the link lengths of the first and second links, respectively, and q_{1i} and q_{2i} are the joint angle values of the first and second joints of the i^{th} branch, respectively. Squaring and adding equations (B-3a) and (B-3b) yields:

$$(x_{3i} + x_{1i})^2 + (y_{3i} + y_{1i})^2 = l_{1i}^{\,2} + l_{2i}^{\,2} + 2l_{1i}l_{2i}(\cos(q_{1i})\cos(q_{1i} + q_{2i}) + \sin(q_{1i})\sin(q_{1i} + q_{2i})) \quad \text{(B-4)}$$

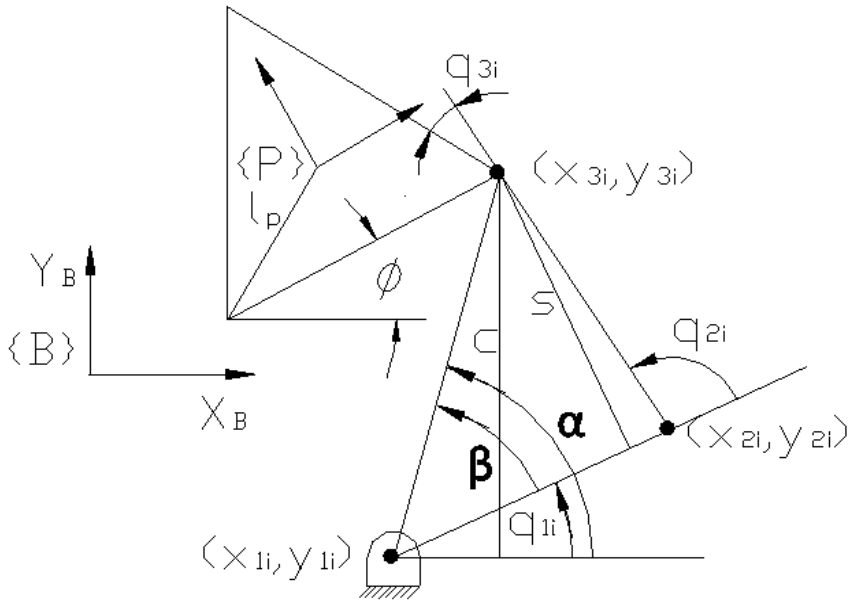

Figure B-2: A *RRR* Type Branch and Its Parameters.

Substituting $q_{1i} = -q_{1i}$ into Equation (B-4) and correcting signs yields:

$$(x_{3i} + x_{1i})^2 + (y_{3i} + y_{1i})^2 = {l_{1i}}^2 + {l_{2i}}^2 + 2l_{1i}l_{2i}(\cos(-q_{1i})\cos(q_{1i} + q_{2i}) - \sin(-q_{1i})\sin(q_{1i} + q_{2i})) \quad \text{(B-5)}$$

Noting the trignometric angle-sum rule (Craig 2005):

$$(\cos(q_1)(\cos(q_2) - \sin(q_1)\sin(q_2) = \cos(q_1 + q_2), \quad \text{(B-6)}$$

allows simplification of Equation (B-5) to:

$$(x_{3i} - x_{1i})^2 + (y_{3i} - y_{1i})^2 = {l_{1i}}^2 + {l_{2i}}^2 + 2l_{1i}l_{2i}\cos(q_{2i}). \quad \text{(B-7)}$$

From Equation (B-7):

$$\cos(q_{2i}) = \frac{(x_{3i}-x_{1i})^2 + (y_{3i}-y_{1i})^2 - l_{1i}^2 - l_{2i}^2}{2l_{1i}l_{2i}}, \quad \text{(B-8)}$$

and therefore, two solutions of q_{2i} are:

$$q_{2i} = \arctan2(\pm\sqrt{1 - \cos^2(q_{2i})},\ \cos(q_{2i})), \quad \text{(B-9)}$$

where the two solutions correspond to elbow down and up assembly modes. Note that arctan2 is a two-argument arctangent operator that takes into account the signs of the two inputs (the numerator and the denominator) and returns the angle in the correct quadrant.

The base joint angle q_{1i} can be expressed as α-β as shown in Figure B-2, i.e.,:

$$q_{1i} = \arctan2(y_{3i} - y_{1i}, x_{3i} - x_{1i}) - \arctan2(s, c + l_{1i}), \quad \text{(B-10)}$$

where $s = l_{2i}\sin(q_{2i})$ and $c = l_{2i}\sin(q_{2i})$. Lastly, wrist joints angle q_{3i} can be found based on Equation (B-3c) as:

$$q_{3i} = \phi + \frac{2\pi(i-1)}{b} - q_{1i} - q_{2i} \quad i = 1,2 \text{ and } 3 \quad \text{(B-11)}$$

Equations (B-9), (B-10) and (B-11) complete the *IDS* for the 3-*RRR PM*.

B.3.2 *IDS* of a 3-*RPR PM*

An *RPR* type branch is shown in Figure B-3. The forward displacement equations of an *RPR* type branch and the platform orientation of a 3-*RPR PM* can be written as:

$$x_{3i} = x_{1i} + q_{2i}\cos(q_{1i}), \tag{B-12a}$$

$$y_{3i} = y_{1i} + q_{2i}\sin(q_{1i}), \tag{B-12b}$$

$$\emptyset = q_{1i} + q_{3i} - (2\pi(i-1))/b \tag{B-12c}$$

where q_{1i} is the displacement of the first joint, i.e., base joint angle and q_{2i} is the displacement of the second joint, i.e., the length of the prismatic joint of branch *i*. Squaring and adding Equations (B-12a) and (B-12b) yields:

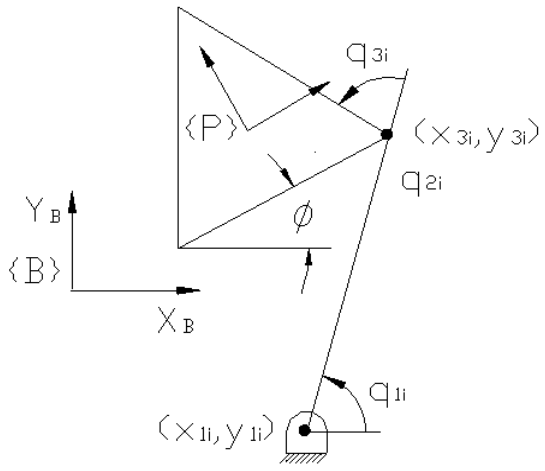

Figure B-3: An *RPR* Type Branch and Its Parameters.

$$q_{2i} = \pm\sqrt{(x_{3i} - x_{1i})^2 + (y_{3i} - y_{1i})^2}, \tag{B-13}$$

where a negative solution for q_{2i} may not be feasible since it is the length of a prismatic joint.

The base joint angle q_{1i} can be found as:

$$q_{1i} = \arctan 2(y_{3i} - y_{1i}, x_{3i} - x_{1i}), \tag{B-14}$$

and the wrist joint angle q_{3i} can be found from Equation (B-12c) as:

$$q_{3i} = \emptyset + \frac{2\pi(i-1)}{b} - q_{1i} \qquad i = 1, 2 \text{ and } 3. \tag{B-15}$$

Equations (B-13), (B-14) and (B-15) complete the IDS for the 3-*RPR PM*.

Appendix C

Screw Coordinates and *ARS*s of *RRR* and *RPR PM* Branch

C.1 Overview

Screw coordinates, and *ARS* coordinates of a *PM* are required to analyze the backlash characteristics of *PMs*. The *PM*s analyzed in this work include 3-*RRR* and 3-*RPR*. In this appendix, the screw coordinates, and the *ARS* coordinates of the actuated joints for the *RRR* and *RPR* branch types are presented.

C.2 Screw Coordinates

Screw coordinates of the joints can be determined regardless of the branch type. The screw coordinates in condensed notation for a planar revolute joint *j* of a branch *i* written as a row vector are:

$$\$_{\text{revolute}} = \{1;\ y_{ji}, -x_{ji}\}.^{T} \qquad \text{(C-1)}$$

Within Equation C-1 the primary vector for a revolute joint is the joint's direction and it is responsible for the rotary contribution of the joint, i.e., it is a unit vector in the *Z*-direction and for a unit screw quantity it is equal to 1, *i.e.*, $\$ = 1. The second vector $\$_o$ is related to translational velocity and it is equal to the moment of the primary vector about the reference frame origin. Denoting the perpendicular normal distance $d = \{x_{ij},\ y_{ji}\}^T$ from the reference origin to the screw, the moment, in terms of unit vetors *i, j,* and k, is equal to:

$$\$_0 = d \times \$ = (X_{ji}i + Y_{ji}j) \times (1K) = (Y_{ji}i + X_{ji}j) = \{Y_{ji}, -X_{ji}\}^T, \qquad \text{(C-2)}$$

a moment equal to the second vector of the unit screw quantity of Equation (C-1). The moment is related to planar motion, i.e., X and Y translation. Note both $\$$ and $\$_o$ have been reduced to only include the coordinates related to planar motion, i.e., terms that are always zero are not included.

The screw coordinates of a prismatic joint are:

$$\$_{\text{prismatic}} = \{0; \cos(\emptyset_{ji}), \sin(\emptyset_{ji})\}. \qquad \text{(C-3)}$$

Equation (C-3) is an unit screw quantity for a prismatic joint. The 0 term in the primary vector is since a prismatic joint does not contribute to rotation, the angle φ_{ji} is the orientation of the joint, an orientation determined in the IDSs of Appendix B. Note that the second vector of the screw coordinates for a prismatic joint is related to the translational motion contribution.

C.3 Associated Reciprocal Screw Coordinates

The *ARS* coordinates of the joint j of the ith branch of a planar *PM* can be denoted as:

$$\$'_{ji} = \{\dot{x}.\dot{y}; d\}^T, \quad \text{(C-4)}$$

Where $\dot{x}$, and $\dot{y}$ specifies the unit direction of the force that is caused by the j^{th} joint of the i^{th} branch, and d is the magnitude of the moment of this unit direction about the origin of the reference frame, i.e., the perpendicular distance between the origin of the reference frame and the force vector. The *ARS* coordinates of the joints are dependent on the branch type and will be presented in sub-Sections C.4 and C.5.

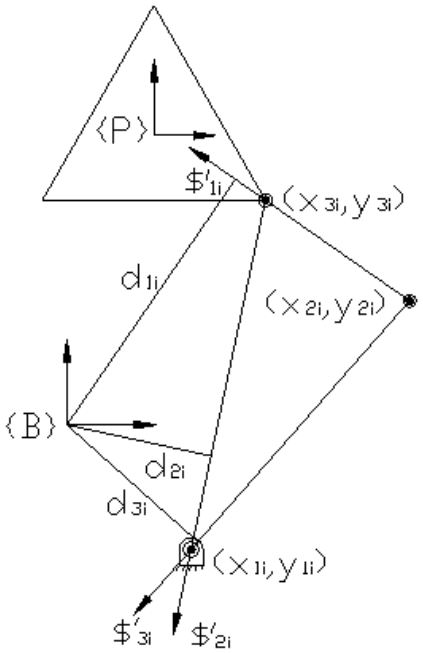

Figure C-1: *ARS* Coordinates of a *RRR* Type Branch.

C.4 *ARS* Coordinates of a *RRR* Branch

ARS coordinates of a *RRR* type branch can be geometrically defined from Figure C-1 as follows:

$$\$'_{1i} = \{\cos(q_{1i} + q_{2i}), \sin(q_{1i} + q_{2i}); d_{1i}\}^T, \quad \text{(C-5a)}$$

$$\$'_{2i} = \left\{\frac{(x_{1i}-x_{3i})}{\text{norm}}, \frac{(y_{1i}-y_{3i})}{\text{norm}}; d_{2i}\right\}^T. \quad \text{(C-5b)}$$

where norm = $((x_{3i}-x_{1i})^2+(y_{3i}-y_{1i})^2)^{1/2}$, and d_{ji} are the perpendicular distances between the origin of the base frame and the screw vector (see Figure C-1), and can be found as:

$$d_{1i} = x_{2i}\sin(q_{1i} + q_{2i}) - y_{2i}\cos(q_{1i} + q_{2i}), \quad \text{(C-6a)}$$

$$d_{2i} = x_{1i}\frac{(y_{1i} - y_{3i})}{\text{norm}} - x_{1i}\frac{(x_{1i} - x_{3i})}{\text{norm}}. \quad \text{(C-6b)}$$

C.5 *ARS* Coordinates of a *RPR* Branch

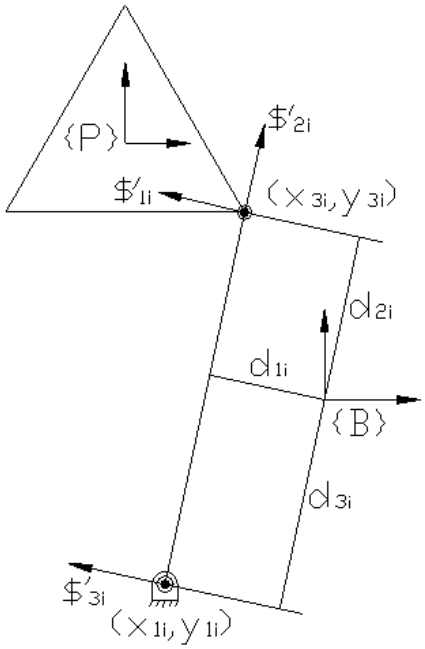

Figure C-2: *ARS* Coordinates of a *RPR* Type Branch.

ARS coordinates of a *RRR* type branch can be geometrically defined from Figure C-2 as follows:

$$\$'_{1i} = \{\cos(q_{1i} + \pi/2), \sin(q_{1i} + \pi/2); d_{1i}\}^T, \quad \text{(C-7a)}$$

$$\$'_{2i} = \{\cos(q_{1i}), \sin(q_{1i}); d_{2i}\}^T, \quad \text{(C-7b)}$$

where d_{ij} are the perpendicular distances between the origin of the base frame and the screw axis (see Figure C-2,) and can be found as:

$$d_{1i} = x_{3i}\sin(q_{1i} + \pi/2) - y_{3i}\cos(q_{1i} + \pi/2), \quad \text{(C-8a)}$$

$$d_{2i} = x_{1i}\sin(q_{1i}) - y_{3i}\cos(q_{1i}). \quad \text{(C-8b)}$$

Appendix D

Programming Source Codes

D.1 Overview

Within Appendix D examples of source codes are given for the programming used in this Dissertation. *MATLAB* has been used in the develo*PM*ent of the source codes used for solving for *PM* branch forces. In particular, source codes for the non-redundantly and redundantly actuated 3-*RPR PM*s executing circle trajectories will be given. Section D.2 presents the coding for the non-redundantly actuated 3-*RPR* and 3-*RPR PMs* executing the circle trajectory.

Section D.3 presents the coding for the redundantly actuated 3-*RPR PM* executing the circle trajectory**,** using the right Moore-Penrose pseudo-inverse solution. Note, the Pseudo-Inverse solution proved to be ineffective for reducing backlash. The results of

the Moore-Penrose pseudo-inverse programing were responsible for related figures in Chapter 4.

Section D.4 presents the coding for the optimizations, using *FMINCON*, for the redundantly-actuated 3-*RPR PM*s executing the circle trajectory. In the *FMINCON* coding of this research, branch numbers are denoted with the indices i = 1, 2, and 3. The base joint of all branchs B_1, B_2 and B_3 are known locations presented as a 3-component row vector, where the order is from branch 1 to 3. For example, for a 3-branch *PM*:

$$i = (1, 2, 3);$$

$$x1 = [0.3, 0, -0.3]; \quad \text{(D-1a)}$$

$$y1 = [-0.1732, 0.34647, -0.1732]. \quad \text{(D-1b)}$$

Equations (D-1) describe the x and y locations of the three base joints. Similarly, *x3* and *y3* are the wrist joint locations, and are presented the same way. The values *q1, q2, q3* and *D1, D2, D3* are related to the *IDS*s and to *ARS1* for the associated reciprocal screws (*ARS*) ***$'*** for each base joint; and to *ARS2* for the *ARS* ***$'*** related to each second joint, and to *ARS3* for the *ARS* ***$'*** related to each third joint. The term s1 denotes the screw coordinates ***$*** of each base revolute joint; and *s2* denotes ***$*** for each elbow revolute joint for 3-*RRR PM*s or for each prismatic joint for 3-*RPR PM*s. *V* are 3-dimensional null-space basis vectors found from decomposing redundant joint wrenches back onto non-redundant wrenches, and *V61* for 6 joints actuated resulting in three 6-dimensional null-space basis vectors (the first two joints of each of the three branches are actuated.) The force *F* is a 100*N* applied force in directions tangent to the cutting trajectories. *Wp* are

particular wrench intensity solutions; and *W1d* are desired wrench intensities for base joints, with *i* denoting each branch.

D.2 Coding for Non-Redundantly Actuated 3-*RPR* and 3-*RPR PM*s Executing a Circle Trajectory

```
function [theta,TAU] = CIRCLENOOP()
clc

theta=0:pi/100:2*pi;
N=length(theta);
xcenter=0.1;
ycenter=0.1;
% center of the trajectory
tau11=zeros(N,1);tau12=zeros(N,1);tau13=zeros(N,1);
W21=zeros(N,1);W22=zeros(N,1);W23=zeros(N,1);
tauPI11=zeros(N,1);tauPI12=zeros(N,1);tauPI13=zeros(N,1);
tauPI21=zeros(N,1);tauPI22=zeros(N,1);tauPI23=zeros(N,1);
WPI21=zeros(N,1);WPI22=zeros(N,1);WPI23=zeros(N,1);
for n=1:N
for i = (1:3)
x1 = [0.3,0,-0.3];
y1 = [-0.1732,0.34647,-0.1732];
%  Step 1.
xp=xcenter+0.05*cos(theta(n));
yp=ycenter+0.05*sin(theta(n));
r = (3+4*i)*pi/6;
x3(i) = xp+0.1732*cos(r+pi/6);
y3(i) = yp+0.1732*sin(r+pi/6);
% Step 2

q1(i) = atan2((y3(i)-y1(i)),(x3(i)-x1(i)));
q2(i) = sqrt((x3(i)-x1(i))^2+(y3(i)-y1(i))^2 );
q3(i) = pi/6+2*pi*(i-1)/3-q1(i);
% Step 3

D1(i) = x3(i)*sin(q1(i)+pi/2)-y3(i)*cos(q1(i)+pi/2);
D2(i) = x1(i)*sin(q1(i)) - y1(i)*cos(q1(i));
D3(i) = x1(i)*sin(q1(i)+pi/2)-y1(i)*cos(q1(i)+pi/2);

% step 4
ARS1(:,i)=[cos(q1(i)+pi/2),sin(q1(i)+pi/2),D1(i)]';
ARS2(:,i)=[cos(q1(i)),sin(q1(i)),D2(i)]';
ARS3(:,i)=[cos(q1(i)+pi/2),sin(q1(i)+pi/2),D3(i)]';
```

```
% step 5
s2(:,i) =[0,cos(q1(i)),sin(q1(i))]';
s1(:,i) =[1,y1(i),-x1(i)]';
% step 6

End
A = ARS1(:,1);
B = ARS1(:,2);
C = ARS1(:,3);

% step 7
for i = 1:3
V(:,i)= ARS1\(-ARS2(:,i));
end

% step 8 then we find 3 of Vi when i = 1,2,3
V61=[V(:,1)',1,0,0];
V62= [V(:,2)', 0,1,0];
V63=[V(:,3)',0,0,1];
% step 9 test out whether the solution is correct.

D =  ARS2(:,1);
E =   ARS2(:,2);
F =   ARS2(:,3);

X = [A, B, C, D, E, F]*[V61',V62',V63'];

%step 10 set ups an equation for F

Force = [(-100*sin(theta(n))),(100*cos(theta(n))), ...
         (-(0.1 +0.05* sin(theta(n)))*(-100*sin(theta(n))) + (0.1 +
0.05*cos(theta(n)))*(100*cos(theta(n))))]';

Wpbase  = ARS1*Force;
tau11(n)=Wpbase(1)*ARS1(:,1)'*[0 1 0;0 0 1;1 0 0]*s1(:,1);
tau12(n)=Wpbase(2)*ARS1(:,2)'*[0 1 0;0 0 1;1 0 0]*s1(:,2);
tau13(n)=Wpbase(3)*ARS1(:,3)'*[0 1 0;0 0 1;1 0 0]*s1(:,3);



Wpelbow = ARS2*Force;
W21(n)=Wpelbow(1)*ARS2(:,1)'*[0 1 0;0 0 1;1 0 0]*s2(:,1);
W22(n)=Wpelbow(2)*ARS2(:,2)'*[0 1 0;0 0 1;1 0 0]*s2(:,2);
W23(n)=Wpelbow(3)*ARS2(:,3)'*[0 1 0;0 0 1;1 0 0]*s2(:,3);
TAU=[tau11,tau12,tau13,W21,W22,W23,tauPI11,tauPI12,tauPI13,WPI21,WPI22,
WPI23];
figure(1)
plot(theta,TAU(:,1:3))
figure(2)
plot(theta,TAU(:,4:6))
```

```
end


% main program
[theta,TAU] = CIRCLENOOP()
figure(1)
hold off
plot(theta,TAU(:,1),'k','linewidth',1.5)
hold on
plot(theta,TAU(:,2),'k--','linewidth',1.5)
plot(theta,TAU(:,3),'k:','linewidth',1.5)
plot([0,201],[0,0],'k','linewidth',1)
xlabel('Angle around circle (rad)')
ylabel('Joint torques (Nm)')
legend('\tau_{11}','\tau_{12}','\tau_{13}')
axis([0 2*pi -50 50])
h = gca;
set(h,'YGrid','on')

figure(2)
hold off
plot(theta,TAU(:,4),'k','linewidth',1.5)
hold on
plot(theta,TAU(:,5),'k--','linewidth',1.5)
plot(theta,TAU(:,6),'k:','linewidth',1.5)
plot([0,201],[0,0],'k','linewidth',1)
xlabel('Angle around circle (rad)')
ylabel('Joint forces (N)')
legend('F_{21}','F_{22}','F_{23}')
axis([0 2*pi -150 150])
h = gca;
set(h,'YGrid','on')
```

D.3 Redundantly Actuated 3-*RPR PMs* Executing a Circle Trajectory Using the Moore-Penrose Pseudo-Inverse Solution

```
function [theta,TAU] = CIRCLENOOP()
clc

theta=0:pi/100:2*pi;
N=length(theta);
xcenter=0.1;
```

```
ycenter=0.1;
% center of the trajectory
tau11=zeros(N,1);tau12=zeros(N,1);tau13=zeros(N,1);
W21=zeros(N,1);W22=zeros(N,1);W23=zeros(N,1);
tauPI11=zeros(N,1);tauPI12=zeros(N,1);tauPI13=zeros(N,1);
tauPI21=zeros(N,1);tauPI22=zeros(N,1);tauPI23=zeros(N,1);
WPI21=zeros(N,1);WPI22=zeros(N,1);WPI23=zeros(N,1);
for n=1:N
for i = (1:3)
x1 = [0.3,0,-0.3];
y1 = [-0.1732,0.34647,-0.1732];
%  Step 1.
xp=xcenter+0.05*cos(theta(n));
yp=ycenter+0.05*sin(theta(n));
r = (3+4*i)*pi/6;
x3(i) = xp+0.1732*cos(r+pi/6);
y3(i) = yp+0.1732*sin(r+pi/6);

% Step 2

q1(i) = atan2((y3(i)-y1(i)),(x3(i)-x1(i)));
q2(i) = sqrt((x3(i)-x1(i))^2+(y3(i)-y1(i))^2 );
q3(i) = pi/6+2*pi*(i-1)/3-q1(i);
% Step 3

D1(i) = x3(i)*sin(q1(i)+pi/2)-y3(i)*cos(q1(i)+pi/2);
D2(i) = x1(i)*sin(q1(i)) - y1(i)*cos(q1(i));
D3(i) = x1(i)*sin(q1(i)+pi/2)-y1(i)*cos(q1(i)+pi/2);

% step 4
ARS1(:,i)=[cos(q1(i)+pi/2),sin(q1(i)+pi/2),D1(i)]';
ARS2(:,i)=[cos(q1(i)),sin(q1(i)),D2(i)]';
ARS3(:,i)=[cos(q1(i)+pi/2),sin(q1(i)+pi/2),D3(i)]';

% step 5
s2(:,i) =[0,cos(q1(i)),sin(q1(i))]';
s1(:,i) =[1,y1(i),-x1(i)]';
% step 6

end

 A = ARS1(:,1);
 B = ARS1(:,2);
 C = ARS1(:,3);

% step 7
for i = 1:3
V(:,i)= ARS1\(-ARS2(:,i));
end

% step 8 then we find 3 of Vi when i = 1,2,3
```

```
V61=[V(:,1)',1,0,0];
V62= [V(:,2)', 0,1,0];
V63=[V(:,3)',0,0,1];
% step 9 test out whether the solution is correct.

D =  ARS2(:,1);
E =   ARS2(:,2);
F =   ARS2(:,3);

X = [A, B, C, D, E, F]*[V61',V62',V63'];

%step 10 set ups an equation for F

Force = [(-100*sin(theta(n))),(100*cos(theta(n))), ...
         (-(0.1 +0.05* sin(theta(n)))*(-100*sin(theta(n))) + (0.1 +
0.05*cos(theta(n)))*(100*cos(theta(n))))]';


 Wpboth = [A, B, C, D, E, F]'/([A, B, C, D, E, F]*[A, B, C, D, E,
F]')*Force
 tauPI11(n)=Wpboth(1)*ARS1(:,1)'*[0 1 0;0 0 1;1 0 0]*s1(:,1);
 tauPI12(n)=Wpboth(2)*ARS1(:,2)'*[0 1 0;0 0 1;1 0 0]*s1(:,2);
 tauPI13(n)=Wpboth(3)*ARS1(:,3)'*[0 1 0;0 0 1;1 0 0]*s1(:,3);
 WPI21(n)=Wpboth(4)*ARS2(:,1)'*[0 1 0;0 0 1;1 0 0]*s2(:,1);
 WPI22(n)=Wpboth(5)*ARS2(:,2)'*[0 1 0;0 0 1;1 0 0]*s2(:,2);
 WPI23(n)=Wpboth(6)*ARS2(:,3)'*[0 1 0;0 0 1;1 0 0]*s2(:,3);
end

TAU=[ tauPI11,tauPI12,tauPI13,WPI21,WPI22,WPI23];
figure(1)
plot(theta,TAU(:,1:3))
figure(2)
plot(theta,TAU(:,4:6))
end

% main program
[theta,TAU] = CIRCLENOOP()
%
% %% plot the data
figure(1)
hold off
plot(theta,TAU(:,1),'k','linewidth',1.5)
hold on
plot(theta,TAU(:,2),'k--','linewidth',1.5)
plot(theta,TAU(:,3),'k:','linewidth',1.5)
plot([0,201],[0,0],'k','linewidth',1)
xlabel('Angle around circle (rad)')
ylabel('Joint torques (Nm)')
legend('\tau_{11}','\tau_{12}','\tau_{13}')
axis([0 2*pi -30 30])
h = gca;
```

```
set(h,'YGrid','on')

figure(2)
hold off
plot(theta,TAU(:,4),'k','linewidth',1.5)
hold on
plot(theta,TAU(:,5),'k--','linewidth',1.5)
plot(theta,TAU(:,6),'k:','linewidth',1.5)
plot([0,201],[0,0],'k','linewidth',1)
xlabel('Angle around circle (rad)')
ylabel('Joint forces (N)')
legend('F_{21}','F_{22}','F_{23}')
axis([0 2*pi -40 40])
h = gca;
set(h,'YGrid','on')
```

D.4 Redundantly Actuated 3-*RPR PM*s Executing a Circle Trajectory for Case -+-.

```
function [theta,TAU] = xmaoRPRCIRCLE()
clc
LB=[ -100 5  -100 .1 .1 .1 0 0 0];
UB=[ -5  100  -5 .9 .9 .9 pi pi pi];
x0=(LB+UB)/2;
x0=UB;
x0=[ -5.0000   58.1050   -5.0000    0.9000    0.9000    0.1000
0.6318    0.7164    0.0000];

OF=funObj(x0)
options=optimset('Algorithm','active-set','MaxFunEvals',2000);
% x = FMINCON(fun,x0,A,b,Aeq,beq,lb,ub,nonlcon,options)
[x,fval]=FMINCON(@funObj,x0,[],[],[],[],LB,UB,@mycon,options)
[OF, TAU]=funObj(x)
theta=0:pi/100:2*pi;
end

function [OF, TAU]=funObj(x)
w=x(1:3);
alpha=x(4:6);
gamma=x(7:9);
theta=0:pi/100:2*pi;
OF=0;
N=length(theta);
xcenter=0.1;
ycenter=0.1;
```

```
% center of the trajectory
tau11=zeros(N,1);tau12=zeros(N,1);tau13=zeros(N,1);
W21=zeros(N,1);W22=zeros(N,1);W23=zeros(N,1);
for n=1:N
for i = (1:3)
x1 = [0.3,0,-0.3];
y1 = [-0.1732,0.34647,-0.1732];
%  Step 1.
xp=xcenter+0.05*cos(theta(n));
yp=ycenter+0.05*sin(theta(n));
r = (3+4*i)*pi/6;
x3(i) = xp+0.1732*cos(r+pi/6);
y3(i) = yp+0.1732*sin(r+pi/6);

% Step 2

q1(i) = atan2((y3(i)-y1(i)),(x3(i)-x1(i)));
q2(i) = sqrt((x3(i)-x1(i))^2+(y3(i)-y1(i))^2 );
q3(i) = pi/6+2*pi*(i-1)/3-q1(i);
% Step 3

D1(i) = x3(i)*sin(q1(i)+pi/2)-y3(i)*cos(q1(i)+pi/2);
D2(i) = x1(i)*sin(q1(i)) - y1(i)*cos(q1(i));
D3(i) = x1(i)*sin(q1(i)+pi/2)-y1(i)*cos(q1(i)+pi/2);

% step 4
ARS1(:,i)=[cos(q1(i)+pi/2),sin(q1(i)+pi/2),D1(i)]';
ARS2(:,i)=[cos(q1(i)),sin(q1(i)),D2(i)]';
ARS3(:,i)=[cos(q1(i)+pi/2),sin(q1(i)+pi/2),D3(i)]';

% step 5
s2(:,i) =[0,cos(q1(i)),sin(q1(i))]';
s1(:,i) =[1,y1(i),-x1(i)]';
% step 6

end

A = ARS1(:,1);
B = ARS1(:,2);
C = ARS1(:,3);

% step 7
for i = 1:3
V(:,i)= ARS1\(-ARS2(:,i));
end

% step 8 then we find 3 of Vi when i = 1,2,3
V61=[V(:,1)',1,0,0];
V62= [V(:,2)', 0,1,0];
V63=[V(:,3)',0,0,1];
% step 9 test out whether the solution is correct.
```

```
D = ARS2(:,1);
E = ARS2(:,2);
F = ARS2(:,3);
X = [A, B, C, D, E, F]*[V61',V62',V63'];

%step 10 setup an equation for F
Force = [(-100*sin(theta(n))),(100*cos(theta(n))), ...
         (-(0.1 +0.05* sin(theta(n)))*(-100*sin(theta(n))) + (0.1 +
0.05*cos(theta(n)))*(100*cos(theta(n))))]';

Wp  = ARS1*Force;

% Wd = w+alpha.*w.*sin(theta+gamma);
w11d=w(1)+alpha(1)*w(1)*sin(theta(n)+gamma(1));
w12d=w(2)+alpha(2)*w(2)*sin(theta(n)+gamma(2));
w13d=w(3)+alpha(3)*w(3)*sin(theta(n)+gamma(3));
Wd=[w11d,w12d,w13d]';

Wdf = Wd  - Wp;
% Evaluate (16)
Wc =   V\Wdf;
tau11(n)=w11d*ARS1(:,1)'*[0 1 0;0 0 1;1 0 0]*s1(:,1);
tau12(n)=w12d*ARS1(:,2)'*[0 1 0;0 0 1;1 0 0]*s1(:,2);
tau13(n)=w13d*ARS1(:,3)'*[0 1 0;0 0 1;1 0 0]*s1(:,3);
W21(n)=Wc(1)*ARS2(:,1)'*[0 1 0;0 0 1;1 0 0]*s2(:,1);
W22(n)=Wc(2)*ARS2(:,2)'*[0 1 0;0 0 1;1 0 0]*s2(:,2);
W23(n)=Wc(3)*ARS2(:,3)'*[0 1 0;0 0 1;1 0 0]*s2(:,3);
End

% Objective function
OF= sqrt(tau11'*tau11+tau12'*tau12+tau13'*tau13 ...
   +W21'*W21+W22'*W22+W23'*W23);
TAU=[tau11,tau12,tau13,W21,W22,W23];
end

function [c,ceq] = mycon(x)
w=x(1:3);
alpha=x(4:6);
gamma=x(7:9);
theta=0:pi/100:2*pi;
N=length(theta);
xcenter=0.1;
ycenter=0.1;
% center of the trajectory
tau11=zeros(N,1);tau12=zeros(N,1);tau13=zeros(N,1);
W21=zeros(N,1);W22=zeros(N,1);W23=zeros(N,1);
for n=1:N
for i = (1:3)
x1 = [0.3,0,-0.3];
y1 = [-0.1732,0.34647,-0.1732];
```

```
%  Step 1.
xp=xcenter+0.05*cos(theta(n));
yp=ycenter+0.05*sin(theta(n));
r = (3+4*i)*pi/6;
x3(i) = xp+0.1732*cos(r+pi/6);
y3(i) = yp+0.1732*sin(r+pi/6);

% Step 2

q1(i) = atan2((y3(i)-y1(i)),(x3(i)-x1(i)));
q2(i) = sqrt((x3(i)-x1(i))^2+(y3(i)-y1(i))^2 );
q3(i) = pi/6+2*pi*(i-1)/3-q1(i);
% Step 3

D1(i) = x3(i)*sin(q1(i)+pi/2)-y3(i)*cos(q1(i)+pi/2);
D2(i) = x1(i)*sin(q1(i)) - y1(i)*cos(q1(i));
D3(i) = x1(i)*sin(q1(i)+pi/2)-y1(i)*cos(q1(i)+pi/2);

% step 4
ARS1(:,i)=[cos(q1(i)+pi/2),sin(q1(i)+pi/2),D1(i)]';
ARS2(:,i)=[cos(q1(i)),sin(q1(i)),D2(i)]';
ARS3(:,i)=[cos(q1(i)+pi/2),sin(q1(i)+pi/2),D3(i)]';

% step 5
s2(:,i) =[0,cos(q1(i)),sin(q1(i))]';
s1(:,i) =[1,y1(i),-x1(i)]';
% step 6

end

A = ARS1(:,1);
B = ARS1(:,2) ;
C = ARS1(:,3);

% step 7
for i = 1:3
V(:,i)= ARS1\(-ARS2(:,i));
end

% step 8 then we find 3 of Vi when i = 1,2,3
V61=[V(:,1)',1,0,0];
V62= [V(:,2)', 0,1,0];
V63=[V(:,3)',0,0,1];

% step 9 test out weather the solution is correct.

D = ARS2(:,1);
E = ARS2(:,2);
F = ARS2(:,3);
X = [A, B, C, D, E, F]*[V61',V62',V63'];
```

```
%step 10 setup an equation for F

Force = [(-100*sin(theta(n))),(100*cos(theta(n))), ...
         (-(0.1 +0.05* sin(theta(n)))*(-100*sin(theta(n))) + (0.1 +
0.05*cos(theta(n)))*(100*cos(theta(n))))]';

Wp  = ARS1*Force;

% Wd = w+alpha.*w.*sin(theta+gamma);
w11d=w(1)+alpha(1)*w(1)*sin(theta(n)+gamma(1));
w12d=w(2)+alpha(2)*w(2)*sin(theta(n)+gamma(2));
w13d=w(3)+alpha(3)*w(3)*sin(theta(n)+gamma(3));
Wd=[w11d,w12d,w13d]';

%Evaluate artificial function (21)
Wdf = Wd  - Wp;
% Evaluate (16)
Wc =   V\Wdf;
tau11(n)=w11d*ARS1(:,1)'*[0 1 0;0 0 1;1 0 0]*s1(:,1);
tau12(n)=w12d*ARS1(:,2)'*[0 1 0;0 0 1;1 0 0]*s1(:,2);
tau13(n)=w13d*ARS1(:,3)'*[0 1 0;0 0 1;1 0 0]*s1(:,3);
W21(n)=Wc(1)*ARS2(:,1)'*[0 1 0;0 0 1;1 0 0]*s2(:,1);
W22(n)=Wc(2)*ARS2(:,2)'*[0 1 0;0 0 1;1 0 0]*s2(:,2);
W23(n)=Wc(3)*ARS2(:,3)'*[0 1 0;0 0 1;1 0 0]*s2(:,3);
end
for i=1:N
c(i)=W21(1)*W21(i);
c(i+N)=W22(1)*W22(i);
c(i+2*N)=W23(1)*W23(i);
end
c = -c;
ceq = [];
end


%main program
[theta,TAU] = xmaoRPRCIRCLE()
figure(1)
hold off
plot(theta,TAU(:,1),'k','linewidth',3)
hold on
plot(theta,TAU(:,2),'k--','linewidth',3)
plot(theta,TAU(:,3),'k:','linewidth',3)
plot([0,201],[0,0],'k','linewidth',1.5)
xlabel('Angle around circle (rad)')
ylabel('Joint torques (Nm)')
legend('\tau_{11}','\tau_{12}','\tau_{13}')
axis([0 2*pi -10 50])
h = gca;
set(h,'YGrid','on')
```

```
h = gca;
set(h,'YGrid','on')

figure(2)
hold off
plot(theta,TAU(:,4),'k','linewidth',2)
hold on
plot(theta,TAU(:,5),'k--','linewidth',2)
plot(theta,TAU(:,6),'k:','linewidth',2.5)
plot([0,201],[0,0],'k','linewidth',1.5)
xlabel('Angle around circle (rad)')
ylabel('Joint forces (N)')
legend('F_{21}','F_{22}','F_{23}')
axis([0 2*pi -80 100])
h = gca;
set(h,'YGrid','on')
```